

RUPRECHT-KARLS-UNIVERSITÄT HEIDELBERG



Hanno Meyer zu Theenhausen

---

Search for Light Dijet Resonances  
using Trigger Jets with the  
ATLAS Experiment at the  
Large Hadron Collider

Dissertation

KIRCHHOFF-INSTITUT FÜR PHYSIK

---



Dissertation  
submitted to the  
Combined Faculties of the Natural Sciences and  
Mathematics  
of the Ruperto-Carola-University of Heidelberg,  
Germany  
for the degree of  
Doctor of Natural Sciences

Put forward by  
Hanno Meyer zu Theenhausen  
born in Ankum

Oral examination on February 8<sup>th</sup>, 2018



# Search for light Dijet Resonances using Trigger Jets with the ATLAS Experiment at the Large Hadron Collider

Referees: Prof. Dr. Hans-Christian Schultz-Coulon  
Prof. Dr. Klaus Reyers



# Abstract

Searches for resonances in the dijet invariant mass spectrum provide a model-independent approach to search for physics beyond the Standard Model at the Large Hadron Collider. In the sub-TeV mass range the sensitivity of dijet searches is statistically limited due to the bandwidth capacity of the data acquisition system. This limitation can be circumvented by only recording the calorimeter jets that are reconstructed within the trigger system, omitting full detector readout. This approach is applied to the analysis of proton-proton collision data recorded with the ATLAS detector at a center of mass energy of  $\sqrt{s} = 13$  TeV with an integrated luminosity of  $29.7 \text{ fb}^{-1}$ . The jets are subjected to a dedicated calibration procedure using calorimeter information only. The search targets dijet resonances in the mass range between 400 and 2000 GeV. Using a data-driven background estimate, no significant excesses are found.

# Kurzzusammenfassung

Die Suche nach Resonanzen im invarianten Massenspektrum von Dijets bietet einen modellunabhängigen Ansatz, um am Large Hadron Collider nach Physik jenseits des Standardmodells zu suchen. Im Sub-TeV Massenbereich ist die Sensitivität von Dijet-Suchen aufgrund der Bandbreitenkapazitäten der Datenerfassungssysteme statistisch begrenzt. Diese Einschränkung kann umgangen werden, indem nur Kalorimeterjets aufgezeichnet werden, die innerhalb des Triggersystems, ohne vollständige Detektorauslese, rekonstruiert werden. Mit diesem Ansatz werden Proton-Proton-Kollisionsdaten analysiert, die mit dem ATLAS Detektor bei einer Schwerpunktsenergie von  $\sqrt{s} = 13$  TeV zu einer integrierten Luminosität von  $29.7 \text{ fb}^{-1}$  aufgenommen wurden. Die Jets werden einer dedizierten Kalibrationsprozedur unterzogen, die ausschließlich auf Kalorimeter Informationen basiert. Die Suche zielt auf Dijet Resonanzen im Massenbereich zwischen 400 und 2000 GeV ab. Unter Verwendung einer datenbasierten Hintergrundabschätzung werden keine signifikanten Exzesse gefunden.



# Contents

<b>Introduction</b>	<b>1</b>
<b>1 Theoretical Foundation</b>	<b>5</b>
1.1 The Standard Model of Particle Physics . . . . .	5
1.2 Jet Production in Quantum Chromodynamics . . . . .	8
1.3 Beyond the Standard Model . . . . .	15
<b>2 Experimental Foundation</b>	<b>25</b>
2.1 The Large Hadron Collider . . . . .	25
2.2 The ATLAS Detector . . . . .	28
2.3 The ATLAS Trigger and Reconstruction System . . . . .	39
<b>3 Reconstruction of Dijet Events</b>	<b>43</b>
3.1 Jet Reconstruction . . . . .	44
3.2 Monte Carlo Simulations . . . . .	49
<b>4 The Dijet Trigger-Object Level Analysis (TLA)</b>	<b>51</b>
4.1 The TLA Approach . . . . .	51
4.2 Analysis Strategy . . . . .	53
4.3 Event Selection and Signal Regions . . . . .	54
<b>5 TLA Jet Calibration and Performance</b>	<b>57</b>
5.1 Jet Calibration . . . . .	57
5.2 Jet Energy Scale Uncertainties . . . . .	75
5.3 Reconstruction Efficiency of TLA Jets . . . . .	81
5.4 The Dijet Invariant Mass Spectrum . . . . .	84
<b>6 TLA Background Estimation</b>	<b>87</b>
6.1 Background Estimation Strategy . . . . .	87
6.2 Sliding Window Fit (SWiFt) . . . . .	88
6.3 Statistical Analysis . . . . .	89
6.4 SWiFt Window Width . . . . .	92
6.5 Background Estimation Robustness . . . . .	98

---

6.6	Expected Sensitivity . . . . .	102
6.7	Unblinding Strategy . . . . .	103
6.8	Dependence on Calibration Smoothness . . . . .	104
<b>7</b>	<b>TLA Search Results in 13 TeV Data</b>	<b>113</b>
7.1	The J75 data . . . . .	113
7.2	The J100 data . . . . .	114
7.3	Discussion . . . . .	115
<b>8</b>	<b>Summary</b>	<b>117</b>
<b>A</b>	<b>TLA Jet Reconstruction and Calibration</b>	<b>119</b>
A.1	Jet Quality Selection . . . . .	119
A.2	Modelling of GSC Jet Property Variables . . . . .	121
	<b>Bibliography</b>	<b>125</b>
	<b>Acknowledgements</b>	<b>135</b>





# Introduction

The Standard Model of Particle Physics (SM) can be considered one of the most successful scientific theories. Since its formulation in the mid-1970s, it has produced accurate predictions to the vast majority of the experimental tests. One such prediction of the SM is the existence of the Higgs boson, which was finally discovered in 2012 at the Large Hadron Collider (LHC) at CERN.

Despite its success, the SM has many shortcomings such as unnatural fine-tuning of its parameters. Most strikingly though, it falls short in describing observed physical phenomena such as gravity, dark matter, dark energy and the matter-antimatter asymmetry. To address these and other problems, many theories beyond the Standard Model (BSM) have been proposed but none have been observed so far. Since many BSM phenomena, such as new particles, are expected to be rare compared to SM processes, the LHC has recently increased its center of mass energy as well as its instantaneous luminosity.

In the proton-proton collisions at the LHC, new particles could be produced by the interaction of two partons of the protons. An example is a mediator particle that connects the SM and the dark matter sector. If the new particle decays back to two quarks (or gluons), two outgoing collimated jets of hadrons (dijets) are produced in the final state. This could be observed in the dijet invariant mass spectrum recorded by the LHC experiments, which would feature a resonance peaked at the mass of the new particle. This signature is therefore very model-independent. The advantage of the model-independent final state towards BSM phenomena comes with the disadvantage of a large background of SM processes. In fact, especially at low masses, the SM dijet production rate is so high that a large fraction of events cannot be recorded due to the limited bandwidth of the data-acquisition and reconstruction systems of the LHC experiments. This leads to an unwanted loss in sensitivity in the sub-TeV mass range, which is, however, especially interesting for searches for dark matter mediator particles.

The ATLAS experiment at the LHC circumvents the limitations in the low mass range by recording only the partial event information that is needed for the search. The partial events contain only calorimeter jets, which are reconstructed “online” at a high rate by the ATLAS trigger system. Using this approach, the ATLAS Trigger-Object Level Analysis (TLA) has collected a set of 28 billion dijet events between 2015 and 2017. This is more than twice as many events as were recorded with the conventional “offline” approach for all other signatures combined. Yet the high statistical power of this analysis comes with the challenge of using calorimeter-based information from the trigger system only and still

achieve a similar performance of jet energy calibration as in the offline approach which uses the full detector information. In addition, the statistical precision of the data adds challenges to the background estimation. Monte Carlo simulations can not be used due to large systematic uncertainties and simple functional forms can not describe the full invariant mass spectrum.

This work reports on the ATLAS dijet TLA in 2016, the employed jet reconstruction and calibration strategy, the background estimation procedure and the search for resonances. Chapter 1 provides a theoretical overview of the SM, jet production and BSM phenomenology with a focus on quantum chromodynamics and on dark matter. Chapter 2 introduces the LHC and the ATLAS detector, highlighting the calorimeters and the trigger system. The reconstruction of dijet events and their simulation in Monte Carlo is explained in Chapter 3. Chapter 4 outlines the TLA approach and the basic event selection for the employed signal regions. In Chapter 5 the TLA jet calibration procedure is presented and the jet performance is characterized in terms of resolution, uncertainties and reconstruction efficiency. Chapter 6 outlines the background estimation strategy which is then applied in the search for possible signals as presented in Chapter 7. Finally, Chapter 8 gives a summary and an outlook on potential improvements in the future.

### **Author's contributions**

No result of ATLAS is the merit of a single individual. Physics analyses usually work in teams of several analyzers and the data which they analyze could only be taken due to the combined effort of the thousands of individuals in the ATLAS collaboration. I contributed to ATLAS as a whole during my work close to the hardware and operation of the L1 calorimeter trigger (L1Calo). Afterwards I was one of the main analyzers in the physics analysis of the dijet TLA.

Within L1Calo I was involved in the finalization of the upgrade of the L1Calo PreProcessor for the LHC run II. I contributed to this during my one year on-site stay at CERN where my work ranged from installation and maintenance of the hardware modules to the commissioning and operation of the upgraded system. My main contribution was to refine the L1Calo monitoring software by adapting it to the new Multi-Chip-Module (nMCM) which represents the heart of the L1Calo PreProcessor. Besides the general adaptation of the monitoring software to a refined software object format, this included the development of additional monitoring software for the new nMCM functions such as the pedestal correction, the second look-up table and the saturated BCID algorithm. The monitoring software is crucial for the stable operation of L1Calo during data-taking and proved viable during the commissioning of the new nMCM functions.

I then turned towards proton-proton collision data analysis with the ATLAS dijet TLA, which is presented in this thesis. I contributed with various studies and projects i.e. on the reconstruction efficiency of trigger jets, a dedicated jet energy calibration based on calorimeter jet information (calorimeter-based Global Sequential Calibration), an in-situ validation technique of the whole calibration chain and a significant reduction of the jet energy scale uncertainties due to a Monte Carlo based determination of the jet flavor

composition and calorimeter response.

The TLA uses a sliding window fit to derive a data-driven background estimate. Here I contributed with studies on the optimal window parametrization. I characterized its performance in terms of the sensitivity and robustness in presence of simulated signals as well as its dependence on theory uncertainties. Furthermore I studied the dependence of the background estimation procedure on the smoothness of the calibration in data and Monte Carlo and validated a new approach to respect systematic uncertainties in the search phase of the analysis. Finally, I used the sliding window fit in conjunction with the bump hunter algorithm in the search for excesses on the dijet invariant mass spectrum.

At the time of writing, the analysis results are prepared for publication.



# Chapter 1

## Theoretical Foundation

This chapter gives an introduction to the underlying principles and the particle content of the Standard Model of particle physics, followed by a brief overview of jet production in quantum chromodynamics. Finally, shortcomings of the Standard Model as well as possible extensions to address these are discussed. This chapter is mostly based on sources [1–8].

### 1.1 The Standard Model of Particle Physics

The Standard Model of Particle Physics is a gauge quantum field theory, describing all known fundamental particles and their non-gravitational interactions with each other. As the term quantum field theory suggests, the fundamental objects of this theory are represented as quantum fields which are defined at all points in space-time and give rise to particles in terms of field quanta of their excitations. The fields can be classified according to their internal angular momentum (spin), separating spin-1/2 fermions (the “matter fields”) from the spin-1 gauge bosons (the “interaction fields”) and the spin-0 Higgs boson. The SM being furthermore a gauge theory means that its physical state (Lagrangian) stays invariant under certain Lie groups of local transformations. The local gauge group of the Standard Model is the unitary product group  $SU(3)_C \times SU(2)_L \times U(1)_Y$ , where each symmetry group gives rise to the aforementioned massless spin-1 gauge bosons and a conserved quantum number corresponding to the group generator.

- $U(1)_Y$  generates a gauge boson  $B$  with conserved quantum number  $Y$ , the *weak hypercharge*.
- $SU(2)_L$  generates gauge bosons  $W_1, W_2, W_3$  with conserved quantum number  $T$ , the *weak isospin*. The index  $L$  denotes that only particles with left-handed parity carry a non-zero  $T$ .
- $SU(3)_C$  generates gauge bosons  $G_{a=1,\dots,8}$  with conserved quantum number  $C$ , the *color charge*, taking 8 possible values.

The  $SU(2)_L \times U(1)_Y$  product constitutes the electroweak symmetry giving rise to the unified *electroweak interaction* that is spontaneously broken to  $U(1)_{EM}$  in nature. This is a result of the *Higgs-mechanism* mediated by the Higgs field  $\phi$ , a complex scalar doublet of  $SU(2)$  with two neutral and two electrically charged components. Due to the Higgs field's potential  $V = \mu^2(\phi^\dagger\phi) + \lambda(\phi^\dagger\phi)^2$ , with  $\mu^2 < 0$ , the field has a non-zero vacuum expectation value, that breaks the symmetry of the electroweak interaction. In this process, three components of the Higgs field are absorbed by three electroweak gauge bosons that acquire thereby mass. After symmetry breaking, the generator (and conserved quantum number) of  $U(1)_{EM}$  is given by a linear combination of the weak hypercharge and the third component of the weak isospin,  $Q = \frac{Y}{2} + T_3$ . The  $W_{1,2,3}$  and  $B$  bosons mix with each other, resulting in the physically observed  $\gamma$ ,  $Z^0$  and  $W^\pm$  gauge bosons,

$$\gamma = \cos \theta_W B + \sin \theta_W W_3 \quad (1.1)$$

$$Z^0 = -\sin \theta_W B + \cos \theta_W W_3 \quad (1.2)$$

$$W^\pm = \frac{1}{\sqrt{2}} (W_1 \mp iW_2) , \quad (1.3)$$

where  $\theta_W$  is the weak mixing angle. The massive  $W^\pm$  and  $Z^0$  bosons mediate the *weak interaction*, while the massless photon  $\gamma$  mediates the *electromagnetic interaction*. The unabsorbed component of the Higgs field accounts for the massive Higgs boson.

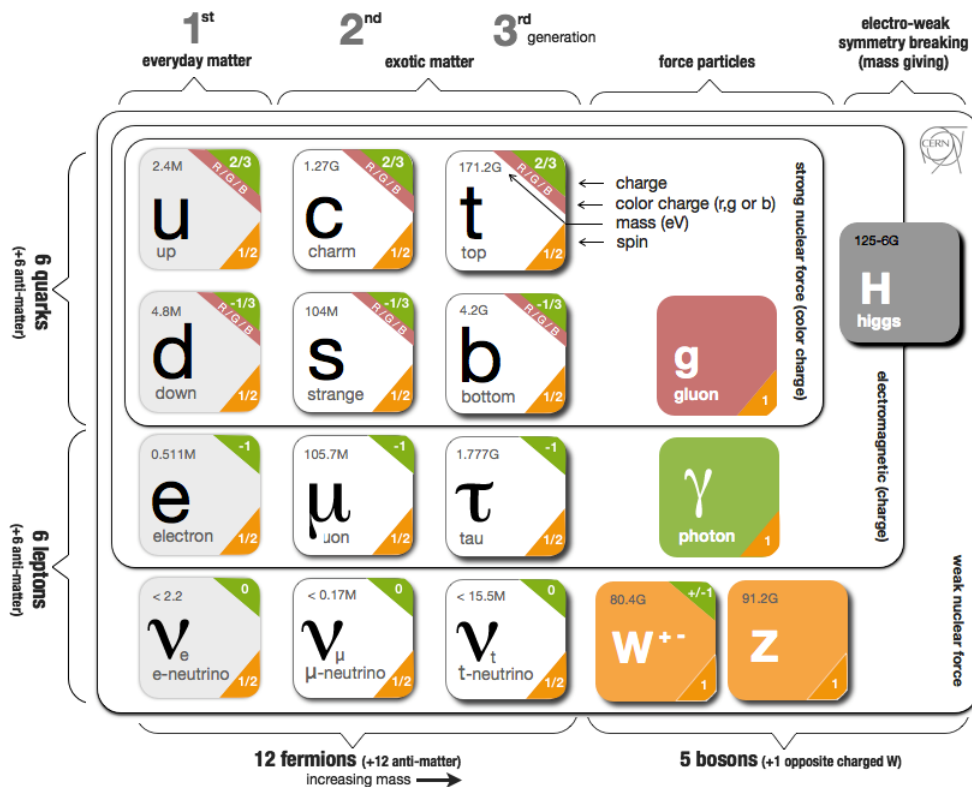


Figure 1.1: The particle content of the SM [9].

The  $SU(3)_C$  group gives rise to the *strong interaction* mediated by the *gluons*  $G_{a=1,\dots,8}$ . The underlying symmetry group is non-abelian leading to *gluon self interaction*, *asymptotic freedom* and *confinement* as explained in more detail in Chapter (1.2).

The fermions of the SM can be sub-grouped according to their affiliation with the fundamental interactions, i.e. *quarks* are subject to all fundamental interactions, *leptons* do not interact strongly and *neutrinos* interact only weakly. Each fermion type comes in three mass generations in which all properties, except the particle mass, are identical. The dynamics of the fermions is described by the Dirac equation. The particle content of the SM is summarized in Figure 1.1.

Guided by experimental data, all aforementioned concepts (quantum field theory, Dirac equation, gauge principle and Higgs mechanism) can be successfully combined into the Lagrangian of the Standard Model,

$$\begin{aligned} \mathcal{L}_{SM} = & \frac{1}{4}W_{\mu\nu}^a W_a^{\mu\nu} - \frac{1}{4}B_{\mu\nu}B^{\mu\nu} - \frac{1}{4}G_{\mu\nu}^a G_a^{\mu\nu} \\ & + \bar{L}\gamma^\mu \left( i\partial_\mu - \frac{1}{2}g\tau^a W_\mu^a - \frac{1}{2}g'Y B_\mu \right) L + \bar{R}\gamma^\mu \left( i\partial_\mu - \frac{1}{2}g'Y B_\mu \right) R \\ & + \frac{1}{2} \left| \left( i\partial_\mu - \frac{1}{2}g\tau^a W_\mu^a - \frac{1}{2}g'Y B_\mu \right) \phi \right|^2 - V(\phi) \\ & + g_s (\bar{q}\gamma^\mu T_a q) G_\mu^a + (G_1 \bar{L}\phi R + G_2 \bar{L}\phi_c R + h.c.) . \end{aligned} \quad (1.4)$$

The first line describes the kinetic energies and self-interactions of the gauge bosons. The second line contains the kinetic energies and electroweak interaction terms of left-handed and right-handed fermions separately. The gauge bosons and the Higgs gain their masses through the Higgs-Yukawa couplings as given in the third line. In the last line the first term represents the interactions between quarks and gluons, whereas the second term describes the fermion mass generation through their Yukawa couplings to the Higgs field. The SM Lagrangian contains 25 free parameters (putting the QCD CP violating phase aside) which need to be set by experiment. Among those are the 12 Yukawa couplings of the fermions to the Higgs field, the 3 coupling strengths of the interactions  $g$ ,  $g'$ ,  $g_s$ , the vacuum expectation value  $v$  and mass  $m_H$  of the Higgs boson as well as 8 flavor mixing angles of the CKM and PMNS matrices. Once these parameters are set,  $L_{SM}$  (or parts of it) can be successfully used to derive concrete experimental predictions. This happens by the rules of quantum field theory either by finding equations of motion following the principle of least action, or, more commonly, by solving path integrals, leading to the graphical representation of Feynman diagrams. Figure 1.2 shows the Feynman diagram vertices of the electroweak sector. The phenomenology of the strong interaction is presented in the following Chapter.

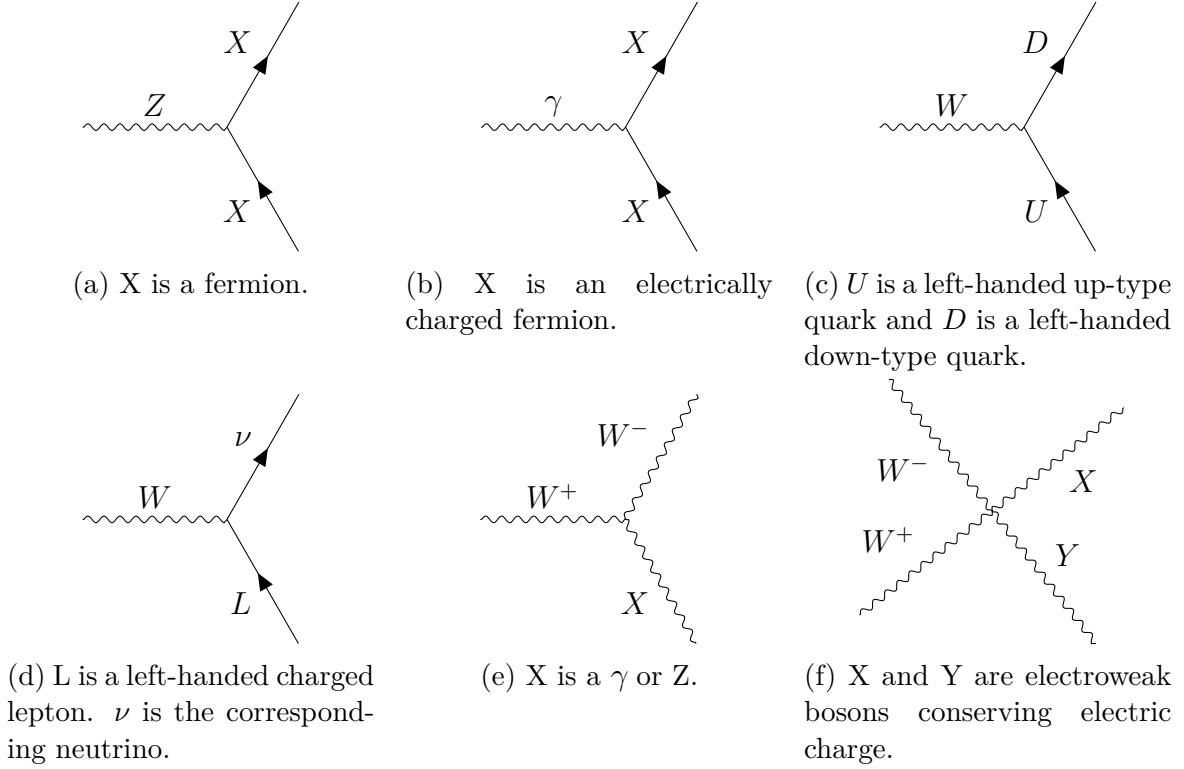


Figure 1.2: The vertices of the electroweak sector.

## 1.2 Jet Production in Quantum Chromodynamics

### 1.2.1 Quantum Chromodynamics

Quantum chromodynamics (QCD) is a non-abelian gauge theory corresponding to the  $SU(3)_C$  gauge group of the SM. Its Lagrangian is defined as

$$\mathcal{L}_{QCD} = -\frac{1}{4}G_{\mu\nu}^a G_a^{\mu\nu} + \sum_q \bar{q}_i (i\gamma^\mu \delta_{ij} \partial_\mu + ig_s T_{ij}^a G_\mu^a - m_q \delta_{ij}) q_j, \quad (1.5)$$

where  $G_{\mu\nu}^a$  is the gluon field strength tensor given by

$$G_{\mu\nu}^a = \partial_\mu G_\nu^a - \partial_\nu G_\mu^a - g_s f^{abc} G_\mu^b G_\nu^c, \quad (1.6)$$

$q_{i,j}$  denotes quark spinors with mass  $m_q$  and color-indices  $i, j = 1, 2, 3$ ,  $G_\mu^a$  are the gluon fields,  $g_s$  is the gauge coupling and  $f^{abc}$  are the structure constants of the Lie group with

generators  $T_{ij}^a$ . The QCD Lagrangian can be described graphically as:

$$\mathcal{L}_{QCD} = \left[ \begin{array}{c} \begin{array}{c} a \text{-----} b \\ \delta^{ab} \end{array} + \begin{array}{c} \begin{array}{c} b \\ \diagup \\ a \text{-----} \\ \diagdown \\ c \end{array} \\ g_s f^{abc} \end{array} + \begin{array}{c} \begin{array}{c} b \\ \diagup \\ a \text{-----} \\ \diagdown \\ c \\ \diagup \\ d \end{array} \\ g_s^2 f^{abe} f^{cde} \end{array} \end{array} \right] \\
 + \sum_{\text{flavors}} \left[ \begin{array}{c} \begin{array}{c} i \text{-----} j \\ \delta_{ij} \end{array} + \begin{array}{c} \begin{array}{c} j \\ \diagup \\ i \text{-----} \\ \diagdown \\ a \end{array} \\ g_s T_{ij}^a \end{array} \end{array} \right]. \quad (1.7)$$

The fermionic part is summed over all quark flavors and contains a free quark field propagator as well as the coupling between quarks and gluons. The gluon field strength tensor describes the free gluon field propagator and two additional terms containing the coupling of gluons to gluons. The gluon self-coupling terms are characteristic of the non-abelian nature of the symmetry group where the commutator of the group generator  $[T^a, T^b] = if_{abc}T^c$  does not vanish. Therefore the gluons themselves carry color with color-index  $a, b, c, d, e = 1, \dots, 8$ . The  $ggg$  coupling is proportional to  $g_s f^{abc}$  and for the  $gggg$  case this is squared. The  $qqg$  coupling is proportional to  $g_s$  and the group generator  $T_{ij}^a$ .

The QCD coupling constant  $g_s$  is the only free parameter of the QCD Lagrangian. It can be related to the strong coupling constant  $\alpha_s$  by  $\alpha_s = g_s^2/4\pi$ .

Predictions for any QCD processes can be made by summing over all relevant diagrams contributing to it and using Feynman rules to find the matrix elements of the involved vertices. Here it is the combination of the gluon self-interaction vertices together with the high energy dependence of the running strong coupling  $\alpha_s$  which makes QCD complex to calculate at low momentum transfers, but leads to a rich phenomenology with concepts like *asymptotic freedom* and *color confinement*. This will be elaborated in the following.

### Running of $\alpha_s$ , asymptotic freedom and color confinement

To retrieve the transition amplitude for  $qq$  scattering, all relevant diagrams, including those containing loops in the gluon propagator, have to be summed up. This is shown in the following illustration:

$$\alpha_s(q^2) = \alpha_s(q^2) + \text{self-energy loop} + \text{ghost loop} + \text{gluon loop} + \dots \quad (1.8)$$

Here contributions from the integrals over momenta of the virtual particles in the loops produce an infinite result for the gluon self energy correction  $\Pi(q^2)$ . The resulting gluon propagator does no longer have a simple  $1/q^2$  form. To retain the  $1/q^2$  form the loop corrections can be absorbed to the definition of  $\alpha_s$  that necessarily depends on  $q^2$ . In principle it is assumed that these loop contributions would cancel if new physics (which we are ignorant of) becomes relevant at high energies in the loops, leading in fact to a finite result. However also being ignorant of new physics, the divergences can still be parametrized by a process called *regularization* and subtracted from the remaining contributions by a process called *renormalization* to recover a finite result. This works because  $\alpha_s$  is finite as an established experimental fact. Thus a known  $\alpha_s$  at some scale ( $q^2 = \mu_R^2$ ) can be used to regularize the divergent self energy loop corrections  $\Pi(\mu_R^2)$  at the renormalization scale  $\mu_R$ . In the resulting expression

$$\alpha_s(q^2) = \frac{\alpha_s(\mu_R^2)}{1 + 4\pi\alpha_s(\mu_R^2) \cdot [\Pi(q^2) - \Pi(\mu_R^2)]}, \quad (1.9)$$

both  $\Pi(q^2)$  and  $\Pi(\mu_R^2)$  are divergent, but their difference is finite. However the dependence of the interaction strength on  $q^2$  remains with

$$\Pi(q^2) - \Pi(\mu_R^2) \approx -\frac{B}{4\pi} \ln\left(\frac{q^2}{\mu_R^2}\right) \quad (1.10)$$

for values of  $q^2$  and  $\mu_R^2$  larger than the confinement scale and thus

$$\alpha_s(q^2) = \frac{\alpha_s(\mu_R^2)}{1 + B\alpha_s(\mu_R^2) \ln\left(\frac{q^2}{\mu_R^2}\right)}. \quad (1.11)$$

Fermionic and bosonic loops contribute to  $B$  with opposite sign, such that

$$B = \frac{11N_c - 2N_f}{12\pi}, \quad (1.12)$$

where  $N_c = 3$  is the number of colors and  $N_f \leq 6$  is the number of quark flavors leading to  $B > 0$ . Consequently  $\alpha_s$  asymptotically *decreases* with increasing  $q^2$  of smaller distance scales. In this regime, i.e. at  $|q| > 100$  GeV as it is common in proton-proton collisions at the LHC,  $\alpha_s$  is  $\mathcal{O}(0.1)$  and quarks and gluons can be treated as quasi-free particles. This

is the aforementioned *asymptotic freedom* of QCD, where  $\alpha_s$  is sufficiently small such that perturbation theory can be used. It is, however, not sufficiently small to neglect higher-order corrections. Therefore QCD calculations are often evaluated beyond lowest order, which is computationally very challenging due to the vast amount of relevant Feynman diagrams. At the other end of the energy spectrum, i.e. at  $|q| \approx 1$  GeV,  $\alpha_s$  is  $\mathcal{O}(1)$  and perturbation theory is not applicable since all Feynman diagrams of higher orders become significant. In this regime, as it is realized inside hadrons, quark-gluon and gluon-gluon self-interaction diagrams lead to a strongly bound state of the partons, giving rise to the concept of *color confinement*. This term denotes that no colored object can propagate as a free particle, but instead the object is confined with other colored objects to form a color neutral state. If two quarks are separated, they exchange gluons which in turn self-interact and therefore form an effective narrow tube of constant high energy density mediating a strong attractive force between the two original quarks. At large separations the energy stored in the gluon field is proportional to the distance between the quarks. Empirically this takes the form

$$V(r) \approx \kappa r, \quad (1.13)$$

where  $\kappa \approx 1$  GeV/fm, corresponding to an enormous force of  $\sim 10^5$  N between any colored objects independent of their separation. At some point of separation it is energetically more favorable to create a  $q\bar{q}$ -pair from the QCD vacuum to form a new color neutral state, rather than further increasing the gluon field energy. Therefore quarks and gluons are generally confined to colorless hadrons, which makes the strong interaction effectively a finite range force. Colorless hadrons can either be mesons ( $q\bar{q}$ ), baryons ( $qqq$ ) or anti-baryons ( $\bar{q}\bar{q}\bar{q}$ ). Also combinations of the above states such as pentaquarks ( $qqqq\bar{q}$ ) and tetraquarks ( $q\bar{q}q\bar{q}$ ) have been observed [10, 11]. The high-energetic partonic final states in proton-proton collisions at the LHC undergo a process called *hadronization*, leaving collimated sprays of hadrons known as *jets* as the main observable final states of QCD interactions.

### The Factorization Theorem

The description of proton-proton scattering at given energies requires to take into account both the perturbatively accessible hard-scattering process of partons on the one hand, as well as the non-perturbative domain of the asymptotically free partons within the proton on the other hand. According to the *factorization theorem* both domains can be treated independently. The DGLAP-equations can be used to describe the evolution of the proton parton distribution functions (PDFs) and perturbation theory can be employed to evaluate the transition amplitudes of the hard scattering. Thus, the scattering cross-section of two partons  $a, b$ , within protons  $A, B$  factorizes to the PDFs  $q_a, q_b$  and the hard scattering cross-section  $\hat{\sigma}_{ab \rightarrow cd}$  with

$$\sigma_{AB \rightarrow X} = \sum_{a,b} \int_{x_a, x_b=0}^1 dx_a dx_b q_a(x_a, \mu_F^2) q_b(x_b, \mu_F^2) \times \hat{\sigma}_{ab \rightarrow cd}(\alpha_s(\mu_R^2), Q^2/\mu_F^2, Q^2/\mu_R^2) , \quad (1.14)$$

where, the  $\mu_F$  is the *factorization scale*. It defines a boundary between the hard and soft terms below which it absorbs collinear and IR divergences of QCD into the definition of the PDFs in a similar way as the renormalization scale absorbs UV divergences into the definition of  $\alpha_s$ . If all orders in  $\alpha_s$  could be taken into account, the resulting cross-section would be independent of  $\mu_F$  and  $\mu_R$ . In reality a dependence on the choice of these parameters remains, resulting in an uncertainty of the theoretical calculation.

### 1.2.2 Kinematic Variables

To describe  $1 + 2 \rightarrow 3 + 4$  parton scattering, which leads to the production of two jets in the final state, it is useful to review the kinematic variables of the interaction. The four-momentum of the involved particles,

$$p^\mu = (E, p_x, p_y, p_z) \quad (1.15)$$

can be expressed in the high-energy limit in the laboratory frame as

$$p^\mu = p_T (\cosh y, \sin \phi, \cos \phi, \sinh y) , \quad (1.16)$$

where  $p_T = \sqrt{p_x^2 + p_y^2}$  is the transverse momentum,  $\phi$  is the azimuthal angle and  $y = \frac{1}{2} \ln \left( \frac{E+p_z}{E-p_z} \right)$  is the rapidity. For high energies, partons can be assumed to be massless and the rapidity is approximated by the pseudorapidity  $\eta = -\ln \tan \left( \frac{\theta}{2} \right)$  which is more directly measurable. Both rapidity variables are preferred over the polar angle  $\theta$  because particle production is roughly constant as a function of  $y$  and  $\eta$  and differences in  $y$  or  $\eta$  are Lorentz invariant under boosts along the  $z$  axis. Relative distances between particles are typically defined as

$$\Delta R = \sqrt{(\Delta\phi)^2 + (\Delta\eta)^2} . \quad (1.17)$$

Further Lorentz invariant variables that are useful to describe the kinematics of the  $1+2 \rightarrow 2+3$  scattering are the Mandelstam variables, defined as

$$\hat{s} = (p_1 + p_2)^2 \quad \hat{t} = (p_1 - p_3)^2 \quad \hat{u} = (p_2 - p_3)^2 . \quad (1.18)$$

satisfying the relation  $\hat{s} + \hat{t} + \hat{u} = 0$ . The Mandelstam variables can be expressed by the scattering angle  $\theta^*$  in the parton center-of-mass system:

$$\hat{t} = -\frac{1}{2} \hat{s} (1 - \cos \theta^*) , \quad \hat{u} = -\frac{1}{2} \hat{s} (1 + \cos \theta^*) . \quad (1.19)$$

The scattering angle in the partonic center-of-mass system can be related to the rapidities of the outgoing partons by

$$\cos \theta^* = \tanh y^* , \quad (1.20)$$

where  $\pm y^*$  expresses the rapidities of the outgoing partons in the partonic center-of-mass system:

$$y^* = \frac{y_3 - y_4}{2} . \quad (1.21)$$

The rapidity of the two-parton system in the laboratory frame is given by:

$$\bar{y} = \frac{y_3 + y_4}{2} . \quad (1.22)$$

Also the invariant mass of the partons can be related through a Mandelstam variable to the proton-proton center-of-mass energy  $\sqrt{s}$ :

$$m^2 = \hat{s} = x_1 x_2 s , \quad (1.23)$$

where  $x_1$  and  $x_2$  are the proton momentum fractions carried by the interacting partons:

$$x_1 = \frac{2p_T}{\sqrt{s}} \cosh y^* e^{\bar{y}}, \quad x_2 = \frac{2p_T}{\sqrt{s}} \cosh y^* e^{-\bar{y}} . \quad (1.24)$$

Thus, the invariant mass can be expressed as:

$$m^2 = 4p_T^2 \cosh^2 y^* \quad (1.25)$$

In practice, the jets from the outgoing partons will not be completely back-to-back, for example due to additional radiations. This can be respected by expressing the dijet invariant mass as:

$$m_{jj}^2 = 2p_{T,3} p_{T,4} (\cosh(\Delta\eta) - \cos(\Delta\phi)) \quad (1.26)$$

### 1.2.3 Jet Production

The cross-section for  $1 + 2 \rightarrow 3 + 4$  parton scattering in a proton-proton collision factorizes according to the factorization theorem into a PDF part and a hard-scattering part. It may be written as

$$\begin{aligned} \frac{d^2\sigma}{dm^2 d\cos\theta^*} &= \frac{1}{32\pi M^2} \sum_{i,j=q,\bar{q},g} \int_0^1 dx_1 dx_2 f_i(x_i, \mu_F^2) f_j(x_2, \mu_F^2) \\ &\times \delta(x_1 x_2 s - M^2) \sum_{\hat{t}} |\mathcal{M}(ij \rightarrow kl)|^2 \frac{1}{1 + \delta_{kl}} , \end{aligned} \quad (1.27)$$

where  $f_{i,j}$  are the PDFs of the respective partons, the delta function ensures four-momentum conservation and  $\frac{1}{1+\delta_{kl}}$  accounts for processes with identical final-state partons.  $\sum_{\hat{t}} |\mathcal{M}|^2$  is the transition matrix element summed over all corresponding diagrams. A selection of leading order diagrams are shown in Figure 1.3.

The four most dominant sub-processes are  $gg \rightarrow gg$ ,  $gq \rightarrow gq$ ,  $qq \rightarrow qq$  and  $q\bar{q} \rightarrow q\bar{q}$ , all of them dominated by the  $\hat{t}$ -channel exchange of gluons [5, 12]. The only sub-process without a  $\hat{t}$ -channel pole is the sub-dominant  $q_1\bar{q}_1 \rightarrow q_2\bar{q}_2$   $\hat{s}$ -channel process. With  $\hat{t} =$

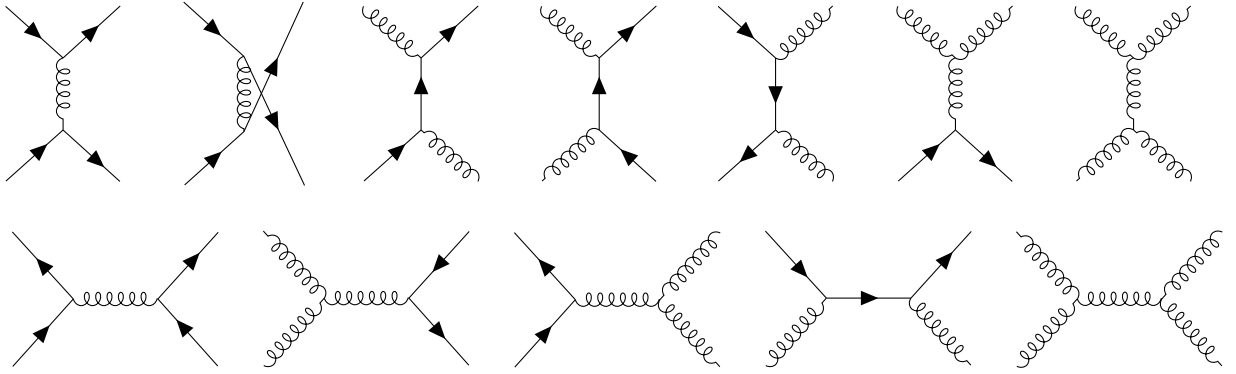


Figure 1.3: Selection of sub-processes contributing to the  $2 \rightarrow 2$  scattering cross-section. Both  $\hat{s}$  and  $\hat{t}$  channel diagrams are shown in different combinations of initial- and final-state partons.

$-\frac{1}{2}\hat{s}(1 - \cos\theta^*)$ , the overall angular dependence of the differential cross-section approximates Rutherford scattering with

$$\frac{d\sigma}{d\cos\theta^*} \sim \frac{1}{\sin^4(\theta^*/2)}. \quad (1.28)$$

Already at leading order the two-parton scattering cross-section calculation involves a vast number of diagrams due to the many possible initial and final states. Evaluation at next-to-leading order (NLO) diminishes the dependence on the renormalization and factorization scale, but at the same time, due to the self-interacting nature of the gluons, the number of contributing diagrams exponentiates.

Four examples of NLO diagrams are given in Figure 1.4. The loop-diagrams (a) and (b) constitute virtual corrections, while (c) and (d) are real corrections in terms of initial and final state radiation. The matrix elements for both diagram types lead to separate divergences. For the real corrections this is the case if the radiation is soft or collinear. In the non-perturbative regime in the initial state these divergences can be absorbed into the definition of the PDF. In the final state, continuous soft and collinear radiations lead to the formation of a *parton-shower* and thus a narrow-coned parton-level jet.

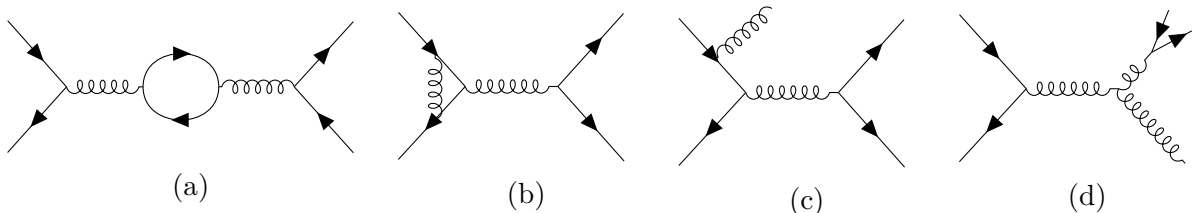


Figure 1.4: Selection of NLO contributions to the parton scattering process. The loop diagrams in (a) and (b) constitute *virtual* corrections, whereas the initial and final state radiation diagrams in (c) and (d) are *real* corrections.

Divergences in the parton-shower can be avoided according to the *Kinoshita-Lee-Nauenberg theorem*, stating that real and virtual contributions precisely cancel [13–15]. This puts requirements onto the observables that are used in the experiment - they must be insensitive to soft and collinear emissions, such that the connection between predicted and measured observables is well defined and not plagued by divergences. These requirements are called *infrared* and *collinear safety* and are respected in the definition of jets, ensuring observables like the jet production cross-section to be well-behaved. As the momentum transfer in the evolution of the parton-shower decreases the process eventually becomes non-perturbative. This triggers the phase of *hadronization*, where partons are combined into colorless states, thus forming a spray of collimated hadrons - a particle-level jet.

At the ATLAS experiment, the Standard Model inclusive dijet production cross-section has been measured to  $\sigma \approx 10.2 \times 10^5$  pb [16] at 13 TeV for dijets with  $p_T > 100$  GeV, which agrees with NLO theoretical predictions. The differential cross-section  $\frac{d\sigma}{dm}$  is smoothly, steeply and monotonically falling and is orders of magnitude above other non-QCD-dominated Standard Model processes.

The differential dijet production cross-section  $\frac{d\sigma}{dm}$  can be enhanced by BSM contributions, for example due to the on-shell production of a new intermediate particle that is decaying into a pair of quarks or gluons. This extends the phase-space for dijet production, thus producing a peaked *resonance* in the differential cross-section, which may be observable as a “bump” in the dijet invariant mass spectrum.

## 1.3 Beyond the Standard Model

### 1.3.1 Limitations of the Standard Model

Although the Standard Model describes the majority of experimental results, to which it can be applied, it is known that it cannot be the final answer for an ultimate theory correctly describing all laws of nature. The most obvious reason for this is that the SM does not predict certain phenomena which otherwise are known to exist.

#### Unexplained phenomena

An obvious unexplained phenomenon is gravity: Any attempts to find a quantum field theory of general relativity lead to a non-renormalizable theory, meaning that it takes an infinite amount of experimental parameters to cancel all arising divergences, rendering the resulting theory useless to derive any predictions. This indicates that the Standard Model is merely an effective theory which breaks down at least at the gravitational scale at  $\Lambda_G = 10^{19}$  GeV. [17]

Other observed phenomena are *dark matter* and *dark energy*, that account for the fact, that the directly observable matter and energy distribution in the universe corresponding to SM particles is not sufficient to explain its gravitational behavior and there is thought to be something in addition which is not (yet) directly observable. Being the most relevant for this thesis, the concept of dark matter is explained in further detail in Chapter 1.3.2.

Another SM insufficiency is the CP-violation of the electroweak interaction, which is not enough to explain the observed *matter-antimatter asymmetry* in the universe. It is assumed that matter and antimatter have been produced to equal amounts during the Big Bang, and therefore should be present in almost equal amounts today. Since this is not the case, either the base assumption does not apply, or an additional asymmetry in the respective evolution of states eventually leads to a dominance of matter over antimatter. [18]

A further phenomenon the SM does not describe is the existence of neutrino oscillations which indicates the existence of neutrino masses. Neutrino-Higgs Yukawa couplings for left- and right-handed neutrinos or even Majorana mass terms for only left-handed neutrinos can be incorporated into the SM by hand, however this construction is deemed unsatisfactory since it offers no insights in the neutrino mass scale being at least  $\mathcal{O}(10^5)$  times smaller than the mass scale of the other elementary particles. [19]

### Theoretical problems

In addition to phenomena which are not explained, the Standard Model in itself has a couple of theoretical shortcomings. These are not problematic in terms of predictions of the theory, but rather indicate a lack of understanding which might also hint to deeper underlying theories or mechanisms.

One example is the *hierarchy problem*. It manifests itself in the mass term of the Higgs boson, which receives quantum corrections proportional to the square of the scale at which the Standard Model is expected to break down, i.e. for fermionic quantum corrections:

$$\Delta m_H^2 = -\frac{|\lambda_f|^2}{8\pi^2}\Lambda^2 + \dots \quad (1.29)$$

The breakdown happens to our knowledge by the latest at the gravitational scale  $\mathcal{O}(10^{19} \text{ GeV})$ , which would imply quantum corrections  $\mathcal{O}((10^{19} \text{ GeV})^2)$  to be precisely canceled out by the Higgs bare mass to leave the observed  $m_H = 125 \text{ GeV}$ . This cancellation requires much higher degree of “fine-tuning” than for the logarithmically divergent quantum corrections appearing for example in QED and QCD, and is therefore deemed “unnatural” by many theorists. Instead it seems reasonable to expect these quantum corrections to cancel for another reason, for example due to an unknown new physics process, possibly entering at a much lower scale.

Another unnatural fine-tuning problem is called the *strong CP problem*. It arises because a priori it is not given why the QCD Lagrangian does not contain an additional CP violating phase, in analogy to the electroweak sector,

$$L_\Theta = \Theta \frac{g^2}{32\pi^2} G_A^{\mu\nu} \tilde{G}_{\mu\nu}^A \quad (1.30)$$

since it would perfectly conserve  $SU(3)_C$  gauge invariance. Experimentally it is found that  $\Theta < 10^{-9}$ , so the strong CP problem denotes the question why  $\Theta$  is so small although it could take values  $\mathcal{O}(1)$ . Interestingly anthropical arguments to solve fine-tuning problems

do not apply to the strong CP problem, because the universe's hospitality seemingly would not change if  $\Theta$  would be  $\mathcal{O}(1)$ . [20]

Finally, there is the straightforward problem that the values of the free 25 Standard Model parameters (26, with the strong CP violating phase) seem ad hoc. They can only be determined experimentally, although some patterns in the parameters seem to indicate an underlying structure. To give some examples, the particle masses are similar within each fermion generation which is most likely not a coincidence, or, the CKM matrix is almost diagonal whereas the PMNs matrix is almost flat. Also the convergence of the running coupling constants seems to suggest that the three SM interactions can be unified at a larger energy scale.

### Unexplained experimental results

Generally the Standard Model describes the vast majority of experimental results extraordinarily well. Up to now there is not a single Standard Model prediction for the existence of a particle or an interaction between particles that has not been confirmed experimentally, given that the experimental sensitivity was sufficient. However there are a few controversial experimental results which do not reflect the Standard Model prediction. One is the *proton-radius puzzle*, expressing a significant inconsistency between the apparent proton radius of ordinary hydrogen and muonic hydrogen [21]. Another is the experimentally measured anomalous magnetic moment of the muon, which is significantly different from the theory expectation [22].

Among the problematic areas of the Standard Model, the most relevant for the scope of this work is dark matter. To some extent dark matter is a *known unknown*, and therefore very encouraging to search for. Its phenomenology is described in more detail in the following section.

#### 1.3.2 Dark Matter

Dark matter is hypothesized to exist because the directly observable matter content of star clusters, galaxies and the large-scale structure of the universe is not sufficient to explain their gravitational behavior.

In galaxies, for example, the rotational velocity of a star of mass  $m$  should be given by the equation of centripetal and gravitational force,

$$\frac{mv^2}{r} \approx \frac{Gm}{r^2}M(r), \quad (1.31)$$

where  $M(r)$  is the total mass within the radius  $r$ . Most of the observable mass is distributed around the galactic bulge, implying rotational velocities proportional to  $1/\sqrt{r}$ . This is not reflected in observations [23]. In fact the measured velocities decrease much slower with  $r$ , according to an actual mass distribution  $M(r) \propto r$  with a large non-luminous component, called dark matter.

There are attempts to explain this discrepancy with a modification to Newton's law of gravity or to general relativity. The predictions of these models however, fail to explain other astrophysical observations, such as the dynamics of the Bullet Cluster (1E 0657-558) without assuming the existence of dark matter. The Bullet Cluster consists of one large galaxy cluster colliding with a smaller sub-cluster which is now exiting the collision-site at a velocity of 4500 km/s in the plane of the sky featuring a bullet-like shape. It can be observed in the optical spectrum, in the x-ray spectrum and via gravitational lensing. The optical spectrum shows the galaxies and stars of the "bullet", being slowed down by the collision only slightly because the distances between them are large and the collision interactions are mostly gravitational. In the x-ray spectrum the intergalactic gas is visible in a bow shock. In contrast to the galaxies and stars, the gas is being slowed down significantly due to the electromagnetic interactions during the collision, and thus lags behind the "bullet". It is important to note that the intergalactic gas makes up a much larger fraction of the matter in the bullet cluster than the stars do. Consequently, without assuming dark matter, one would expect in additional gravitational lensing observations of background objects, the strongest lensing to follow the gas distribution. This again is not observed. Instead the point of strongest lensing follows the galaxies and stars. This is in contrast to models with modifications to the gravitational laws [24]. But observations do confirm the existence of dark matter and, moreover, constrain the interactions of dark matter with the intergalactic gas and with itself [25].

However, there are indications that there is indeed some form of weak interaction of dark matter particles  $\chi$  with themselves and with SM particles. Assuming such interactions has the advantage that the current abundance of dark matter in the universe can be understood as a result of a thermal freeze-out from thermal equilibrium between SM and DM particles after their production through the decay of the inflaton field  $\phi$  shortly after the Big Bang. Known under the term "*WIMP miracle*" it turns out, that a *weakly interacting massive particle* as DM candidate particle, with coupling strength and mass on the order of the weak scale, e.g.  $\mathcal{O}(100 \text{ GeV})$ , would lead to exactly the relic abundance of dark matter which is observed today in the universe, independent of the branching ratios from inflaton to dark matter decays ( $\phi\phi \rightarrow \chi\chi$ ). The relic density is then just a product of the time evolution of WIMPs and SM particles in thermal equilibrium in an expanding universe which would elegantly circumvent another fine-tuning problem.

The relic density of DM has been determined to  $\Omega_c h^2 = 0.1199 \pm 0.0022$  [26] by the Planck-Satellite from measurements of anisotropies in the cosmic microwave background. This amounts to  $\sim 5.3$  times more dark matter in the universe compared to baryonic matter, of which the relic density has been measured to  $\Omega_c h^2 = 0.02222 \pm 0.00023$  [26].

There is additional compelling evidence for the existence of dark matter from velocity dispersions [27], gravitational lensing [28], baryonic acoustic oscillations [29], redshift surveys [30] and large scale structure formation [31]. To summarize, all mentioned observations and conclusions suggest that dark matter:

- does act gravitationally
- does not interact electromagnetically

- is constituted of stable massive particles
- does most likely not interact via the strong force
- is likely to interact with SM particles (and itself) via the weak force or a different kind of force, which is as weak or weaker than the weak force. This corresponds to a WIMP.

Candidate particles for WIMPs are for example the *lightest neutralino* [32], an additional neutral Higgs boson state from *two Higgs doublet* models [33], new heavy states from *little Higgs* models [34], a member of the twin sector in the *twin Higgs* mechanism [35] or the *scalar neutrino* [36].

### 1.3.3 Theories Beyond the Standard Model

To address the aforementioned limitations of the Standard Model, many extensions (BSM models) have been put on the market. The most prominent of which address many SM problem areas at once, such as *Supersymmetry* [37] or *Grand Unified Theories* [38], whereas others address only a certain SM problem, e.g. the *Little Higgs* model [39].

Supersymmetry proposes a new broken symmetry relating bosons and fermions to each other, doubling the particle content of the SM by introducing a superpartner to every particle which differs by half a unit of spin. Loops of superpartners can easily cancel SM contributions to the Higgs self-energy, providing a solution to the hierarchy problem and the lightest stable supersymmetric particle (LSP) arises as a natural candidate for dark matter. Also the unification of forces seems even more plausible in a supersymmetric scenario because here all interaction couplings can converge towards a single point. [40]

In certain supersymmetric models, such as those violating *R-parity*, the decay of *stop* particles is accessible via dijet resonance searches [41].

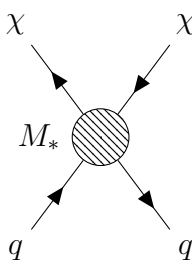
Grand Unified Theories (GUTs) attempt to accommodate the gauge symmetries of the Standard Model into a larger symmetry group. Candidate gauge groups are for example  $SU(5)$ ,  $SO(10)$  and  $E_6$ . GUTs typically reduce the number of free coupling parameters of the Standard Model, as those are degraded to the low energy manifestations of a single unified coupling parameter. Many more appealing features are possible, especially when combined with supersymmetry, such as an explanation for the matter-antimatter asymmetry due to the  $C$ ,  $CP$  and baryon number violating decay of new  $X$  and  $Y$  gauge bosons of the superior symmetry group [42]. Here baryon number is violated naturally because of a fundamental quark-lepton coupling in GUTs [43], which also relates the quark and lepton masses within the mass generations [42]. Another interesting feature of GUTs is an explanation for the quantization of electric charge [42]. In many variations of these models the superior symmetry group can be decomposed into an additional  $U(1)'$  gauge symmetry, giving rise to new heavy vector bosons  $Z'$ ,  $W'$ . Although being much heavier than their SM counterparts, their masses could fall within the reach of the LHC [44], where they could be detectable for example via their decay to a pair of jets.

There are more popular BSM theories, of which many predict distinctive experimental signatures to search for in particle collision experiments. The analysis of this work, the dijet TLA, is *signature-driven*, meaning that it is sensitive to a large variety of BSM theories rather than being fine-tuned towards the final state of a certain BSM model. The aforementioned  $Z'$  particle is only one of many possibilities for an intermediate particle that could possibly decay into a dijet final state. In fact, the dijet final state is one of the most inclusive signatures from a model independent point of view, because any potential new particles produced in the proton-proton collisions at the LHC must interact with the partons of the proton in the initial state and thus should also be able to decay into partons (jets) in the final state.

In the context of the inclusiveness of this search and the large variety of models, it is convenient to find a more general parametrization to interpret any search results. As such, this analysis uses generic Gaussian signal shapes as a phenomenological parametrization for any beyond Standard Model processes that lead to a localized dijet resonance. Moreover, a simplified dark matter mediator model is used as a benchmark model to interpret the search results in the context of a dark matter search, where the TLA is expected to be especially advantageous due to the high search sensitivity at low probed masses. The simplified dark matter mediator model will be explained further in the following section.

### 1.3.4 A Simplified Dark Matter Axial Mediator Model

Given the large variety of dark matter models, and the different dark matter detection methods, it is important that analysers of experimental data interpret their results in a way that covers a range of models as broad as possible, while staying at the same time as model independent as possible. One way to do this is the *effective field theory* (EFT) approach. In the context of WIMP dark matter an effective field theoretical description of the interactions between DM and SM fields can be realized by contact interactions through a set of non-renormalizable operators, such as:

$$\mathcal{L}_{EFT} = \frac{1}{M_*^2} (\bar{q}q)(\bar{\chi}\chi) \quad (1.32)$$


where the quark field  $q$  and DM particle fields  $\chi$  couple via a scalar interaction. The energy scale  $M_*$  determines the interaction strength and is taken to the power of 2 to recover the mass dimension of the Lagrangian<sup>1</sup>. The EFT approach can be used to describe all dark matter detection methods by a single operator, dependent on the arrow of time in the EFT

<sup>1</sup>The mass dimension of the Lagrangian is 4, whereas the EFT operator is of mass dimension 6.

diagram (left-right: direct detection, up-down: indirect detection/annihilation, down-up: collider production). [45]

The EFT approach, however, only describes higher-order processes consistently if the energy scale of the interaction is small compared to  $M_*$  - a requirement which is not necessarily fulfilled at colliders such as the LHC. The scattering events at the LHC occur at high enough energies allowing the direct production of the interaction mediator itself. In this case it is indispensable to include a propagating mediator to the degrees of freedom of the DM SM contact interaction. This approach is known as a *simplified model* [45].

An appealing feature of simplified models in the DM context is that in the currently probed parameter space the interactions can be large enough to allow for significant dark matter annihilation cross-sections, avoiding dark matter overproduction in the early universe [46]. These models can be categorized dependent on the spin of the mediator  $s_R = (0, 1/2, 1, \dots)$ , the mediator exchange channel  $c = (s, t)$  and the spin of the DM particle  $s_\chi = (0, 1/2, 1, \dots)$  with nomenclature  $s_R c s_\chi$  [45]. The benchmark model for this work follows the  $1s\frac{1}{2}$  case, where the DM particle  $\chi$  is a Dirac fermion of mass  $m_\chi$  interacting with SM particles (and itself) via the exchange of an axial-vector mediator  $R$  of mass  $M_R$ . This model defines no gauge symmetry, anomaly-breaking additional fields or symmetry-breaking. Hence, being an effective theory as well, some unspecified dynamics would be needed to complete the model in the ultraviolet. These are assumed to be decoupled from the phenomenology at the relevant probe energies. Thus, the Lagrangian of this simplified axial-vector model can be written as

$$\mathcal{L}_A = g_\chi^A \bar{\chi} \gamma^\mu \gamma^5 \chi R_\mu + \sum_q g_q^A \bar{q} \gamma^\mu \gamma^5 q R_\mu, \quad (1.33)$$

where  $g_\chi^A$  and  $g_q^A$  are the couplings of the mediator to DM particles or quarks respectively [46]. One example for a UV complete model with similar phenomenology is a massive  $Z'$  arising from a new broken  $U(1)_X$  gauge symmetry [47][48]. Note, that even when arising from the same gauge group, the respective couplings could easily differ by a small factor [49][50]. Since in the model above couplings to leptons have been neglected, the mediator is also referred to as “leptophobic  $Z'$ ”. This benchmark signal is chosen because of the large complementarity in the exploration of its  $(g_\chi^A, g_q^A, m_\chi, M_R)$  parameter space between constraints from direct detection experiments, the observation of the relic abundance, mono-jet collider searches and finally dijet collider searches. The respective processes arising in the benchmark model are sketched in Figure 1.5.

Constraints to this model in the  $(g_\chi^A, g_q^A, m_\chi, M_R)$  parameter space are illustrated in Figure 1.6. The exclusion contours were presented by the authors of [46] based on the calculated versus observed relic density, 2013 results from the direct detection experiment “LUX” [51], 2012 results from CMS monojet searches [52], and finally combined results from dijet searches from UA2 [53], CDF [54], CMS [55] and ATLAS [56][57]. It is recognizable that the different methods complement each other. Combinations of large  $M_R$  and small  $m_\chi$  lead to DM overproduction and are therefore excluded by the observed relic abundance. The calculated relic abundance is significantly depleted for  $m_\chi = M_R/2$ , which enhances the annihilation cross-section due to an on-shell resonance and weakens the limits. Naturally

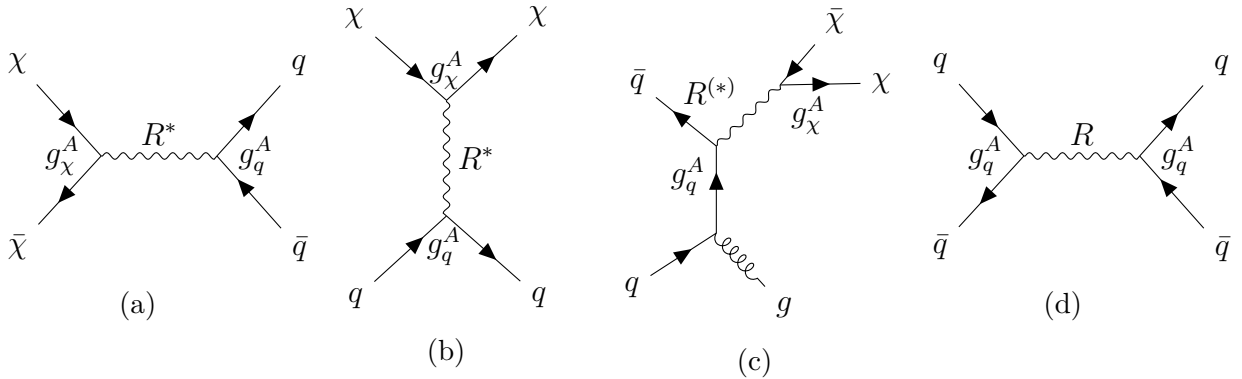


Figure 1.5: Underlying processes of methods to constrain the simplified model involving the DM particles  $\chi$ ,  $\bar{\chi}$ , quarks  $q$ ,  $\bar{q}$  and the on-shell (off-shell) mediator particle  $R$  ( $R^*$ ): (a) Annihilation, occurring in indirect detection experiments and setting the relic abundance, (b) DM - quark scattering, occurring in direct detection experiments, (c) collider monojet signature, composed of invisible DM particles and an initial state radiation gluon, (d) collider dijet resonance signature, where a produced mediator particle decays back into two quarks.

the overproduction parameterspace is dependent on the choice of coupling  $g \equiv (g_\chi^A g_q^A)^{\frac{1}{2}}$  and  $g_\chi^A/g_q^A$ . It is to note that not only the contour of the DM particle overproduction is interesting as it returns exactly the observed relic abundance, but also the parameterspace below because here the respective DM particles could still be a sub-component of the total DM content of the universe. Exclusions from direct detection experiments are strongest where the parameters predict a large DM particle density. Therefore the limits weaken when considering the annihilation enhancement due to  $m_\chi = M_R/2$  or when  $g_q^A$  becomes smaller. Monojet searches provide stronger constraints than direct detection experiments in regions where an on-shell production of the mediator and the DM particles is kinematically allowed. This corresponds to low mediator masses and  $m_\chi < M_R/2$ . Finally, dijet searches provide a powerful completion to the exclusion potential of the other detection methods. For  $g_\chi^A/g_q^A = 1$  a large mediator mass range  $130 \text{ GeV} < M_R < 2.5 \text{ TeV}$  can be excluded by dijet measurements. For  $g_\chi^A/g_q^A > 1$  the dijet exclusion power is weakened, especially for  $m_\chi < M_R/2$ , where the mediator decays primarily to DM particles instead of quarks. This dependence is opposite from monojet searches, which demonstrates the strong complementarity between the two methods. With particular relevance to this work, it is to note that for several choices of coupling, e.g. in Figure 1.6d, there is a large area of unexcluded parameter space for mediator masses smaller than those currently excluded by dijet searches. Furthermore it can be seen that to ensure perturbativity, the DM particle mass  $m_\chi$  must not be much larger than the mediator mass  $M_R$ , especially for couplings  $g$  close to unity. This is not necessarily a hard constraint on the underlying physics, but rather a constrain on the expressiveness of the simplified model. [46]

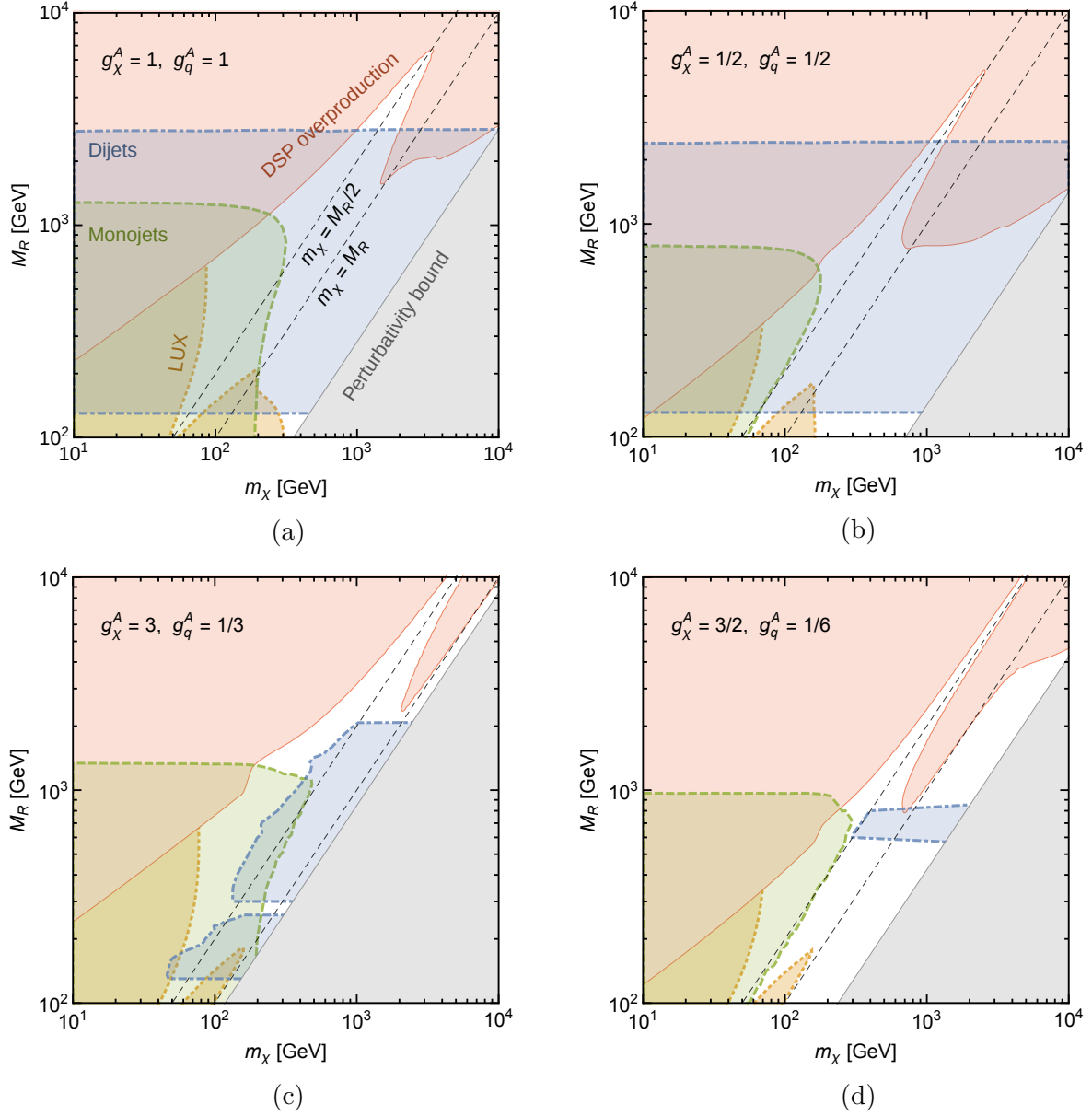


Figure 1.6: Combined (95% C.L.) exclusion contours in the  $(g_\chi^A, g_q^A, m_\chi, M_R)$  parameter space from the observed relic density (red), direct detection experiments (orange, dotted), monojet searches (green, dashed) and dijet searches (blue, dot-dashed). The perturbativity bound is given in gray. The plots on the left (right) show different couplings with  $g \equiv (g_\chi^A g_q^A)^2 = 1$  (1/16), while the upper (lower) plots have coupling ratios of  $g_\chi^A/g_q^A = 1$  (9). The plots are taken from [46].



# Chapter 2

## Experimental Foundation

The far-reaching theoretical predictions of the BSM physics models are matched by the large-scale technical effort in the experimental searches for them. The experimental data for this work was recorded by the ATLAS detector, a large general-purpose particle detector, measuring the proton-proton collision products by the LHC, the world's most powerful particle accelerator. Both machines are introduced in the following sections, starting with the LHC based on [58], followed by the ATLAS detector based on [59] with a focus on the physical principles of particle detection [60, 61].

### 2.1 The Large Hadron Collider

The Large Hadron Collider located at CERN, Geneva, is a 26.7 km circumference storage ring, accelerating counter rotating beams of protons<sup>1</sup> and colliding them at four equally spaced interaction points. Protons are injected into the LHC as pre-accelerated *bunches*, clusters of  $\sim 10^{11}$  protons, using the CERN accelerator infrastructure with the LINAC2, PS and the SPS for pre-acceleration and a duoplasmatron to extract the protons from hydrogen gas. Having bunches of protons rather than a continuous beam allows for the acceleration mechanism by radio frequency cavities, where the protons receive a momentum increase in a certain phase of an electromagnetic field oscillating at 400 MHz with an effective field strength of 2 MV/m. The maximum acceleration corresponds to a kinetic energy of 7 TeV. In contrast to lepton colliders, at the LHC this energy is not limited due to the compensation of energy losses from synchrotron radiation, but due to the bending power of the magnets keeping the protons on the required circular trajectory. To ensure a maximized magnetic field strength to moderate cost, the LHC uses 1232 superconducting dipole magnet coils made of NbTi, a type-II superconductor with high critical field and current densities. The coils sustain nominal currents of 11.85 kA producing a magnetic field of 8.33 T. For stable operation they need to be cooled down to 1.9 K realized by the excellent heat conduction properties of superfluid helium. Therefore the LHC hosts the

---

<sup>1</sup>The LHC can also be filled with heavy ions such as *Pb*. This mode of operation is not relevant for this thesis and is therefore not described.

largest cryogenic system in the world to ensure a stable superconducting state. The LHC employs further 392 quadrupole magnets, used to squeeze the beam to counteract the beam dispersion and to focus the beam towards an interaction point inside the detectors. While the center-of-mass energy depends on the dipole magnets' performance, it's the quadrupole magnets' performance that sets the maximum achievable instantaneous luminosity of the LHC, given by

$$L = \frac{N_b^2 n_b f_{rev} \gamma_r}{4\pi \epsilon_n \beta^*} F, \quad (2.1)$$

where  $N_b$  is the number of protons per bunch,  $n_b$  is the number of bunches per beam,  $f_{rev} = 11.2 \text{ kHz}$  is the revolution frequency and  $\gamma_r$  is the relativistic gamma factor.  $\epsilon_n$  is the normalized transverse beam emittance which is a measure for the beam dispersion in terms of the average spread of particle coordinates in position and momentum phase space and  $\beta^*$  approximates the distance from the focus point at which the beam width is twice as wide as at the focus point.  $F$  is a correction factor accounting for the loss in luminosity due to the non-zero beam crossing angle. The LHC houses up to 2808 proton bunches per beam with a bunch spacing of 25 ns. They are organized in “bunch trains” to leave larger spaces for beam injection and beam dump mechanisms. This way, luminosity values of up to  $17.4 \times 10^{33} \text{ cm}^{-2}\text{s}^{-1}$  are achieved [62]. High luminosity values allow studying rare processes since the event rate of a given process is proportional to its cross-section  $\sigma$  times the luminosity:  $\frac{dN}{dt} = L \cdot \sigma$ . For a fixed  $n_b$ , high instantaneous luminosities make high demands on the experiments' abilities to select the process of interest in high *pile-up* environments, where many collisions occur within the same bunch crossing and “pile” onto the hard scatter process of interest.

A large provided *integrated luminosity*  $L_{int} = \int L dt$  is also of high relevance since it corresponds to the total amount of data that can be taken by the experiments. It depends

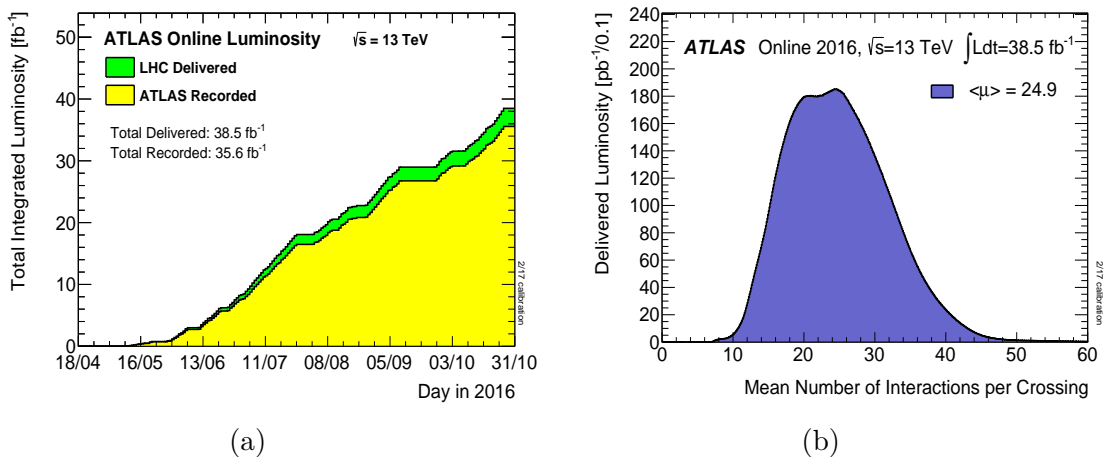


Figure 2.1: Integrated luminosity versus day as it was delivered to ATLAS (green) and recorded by ATLAS (yellow) during the 2016 data-taking period (a) and the distribution of the mean number of interactions per bunch crossing  $\mu$  (b). [62]

largely on the smoothness of operations in and between fills. Injecting and accelerating a complete LHC fill takes approximately 1 to 2 hours, followed by an up to 30 hour *run* in which the experiments record their data. Due to the colliding bunches and other beam losses the instantaneous luminosity gradually decreases throughout a run, which eventually justifies a new filling cycle. Runs of similar filling conditions are grouped into alphabetically enumerated *run periods* which ranged from period A to period L during 2016 data-taking. The progression of integrated luminosity during the data-taking periods relevant for this work can be seen in Figure 2.1(a).

The total integrated luminosity delivered by the LHC during the year 2016 amounts to  $38.5 \text{ fb}^{-1}$  while the integrated luminosity recorded by ATLAS is  $35.6 \text{ fb}^{-1}$ .

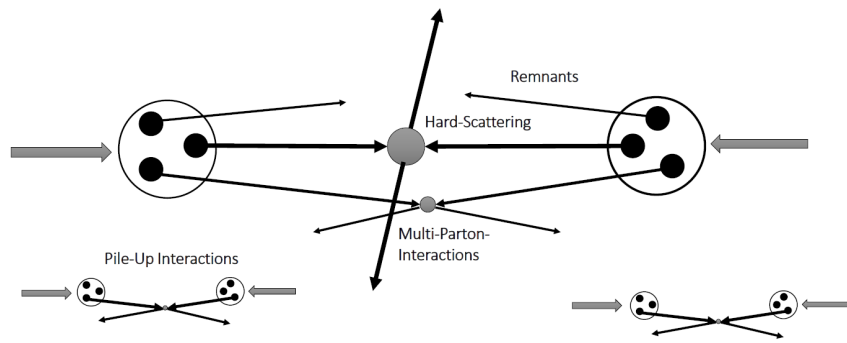


Figure 2.2: Illustration of the underlying event and pile-up interactions.

Despite the many proton-proton interactions occurring at the LHC interaction points, a hard-scattering to occur is not the rule. Typically around 40% of bunch crossings are dominated by diffractive and elastic processes [63]. If a hard-scattering occurs, its final state products are usually accompanied by a number of by-products from a variety of processes as illustrated in Figure 2.2. These can come from the very same proton-proton collision due to multiple parton interactions (MPIs) or the remnants from colliding protons, summarized under the term *underlying event*. Furthermore, the process of interest is accompanied by the products of neighboring proton-proton interactions, known as *pile-up*. These can come from proton-proton interactions within the same bunch crossing (*in-time pile-up*), but also from the remnants of past and even future bunch crossings influencing the time-evolution of the detector signals of interest (*out-of-time pile-up*). Further background activity comes from cosmic radiation and from background radiation of the detector cavern as well as detector noise.

The pile-up distribution parametrized as the mean number of interactions per bunch crossing  $\mu$  is shown in Figure 2.1(b).

## 2.2 The ATLAS Detector

The ATLAS detector is a multi-purpose particle detector enclosing one of the four interaction points of the LHC. It is of forward-backward symmetric cylindrical geometry wrapping the beam pipe with layers of tracking, calorimeter and muon detectors with the nominal interaction point at the detector center. An illustration of the dimensions and components of ATLAS is given in Figure 2.3.

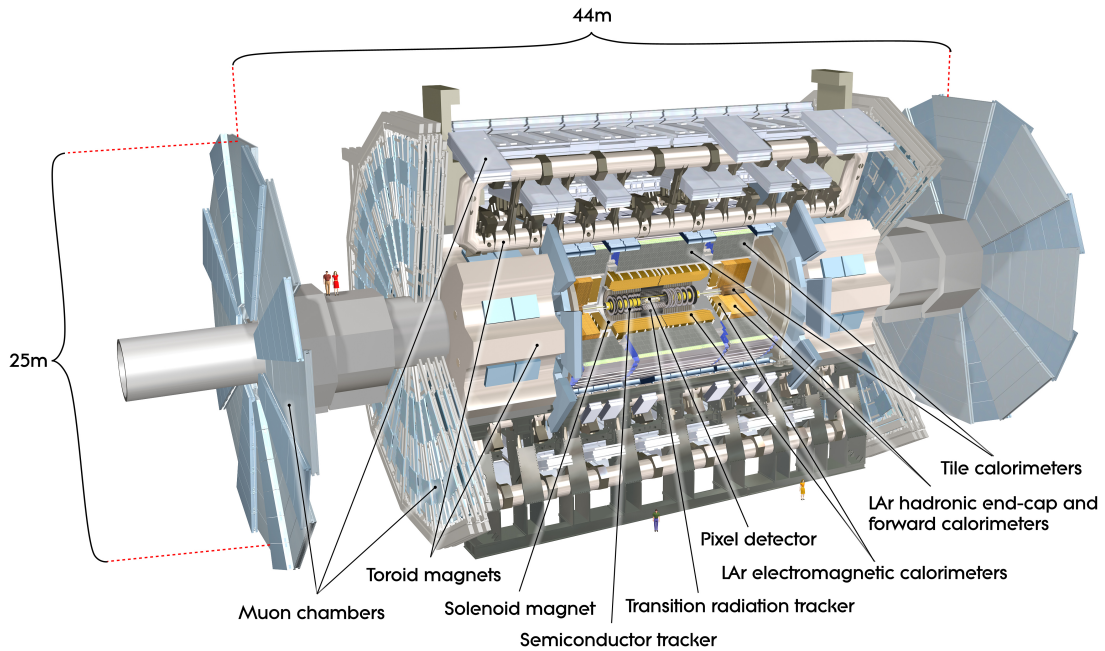


Figure 2.3: Computer generated image of the ATLAS detector and its main components [64].

In total ATLAS measures 44 m in length, 25 m in height and weighs over 7000 tons, consisting of micro- and macroelectronics, absorption and active material, superconducting magnet coils and support structures. Not shown are the computers of the trigger and data reconstruction system.

ATLAS uses a right hand coordinate system with the nominal interaction point at the origin and the beam direction as  $z$  axis. The  $x - y$  plane is transverse to the beam, with  $x$  pointing to the center of the LHC ring and  $y$  pointing skywards. The main observables of reconstructed particles are expressed with respect to this coordinate system. For example flight directions of particles can be expressed using angles. The azimuthal angle  $\phi$  is measured around the beam pipe and the polar angle  $\theta$  as well as the pseudo-rapidity  $\eta$  indicate the angle from the beam axis. The maximum  $\eta$  coverage of ATLAS reaches up to  $|\eta| = 4.9$  being limited by the beam pipe itself.

Among the many particles ATLAS can principally detect, a few of them are long-lived and

distinguished enough to be directly detectable on an event by event basis. An illustration of how these particles are identified by their interactions (or non-interactions) with the ATLAS sub-detectors is given by the “detection onion” in Figure 2.4.

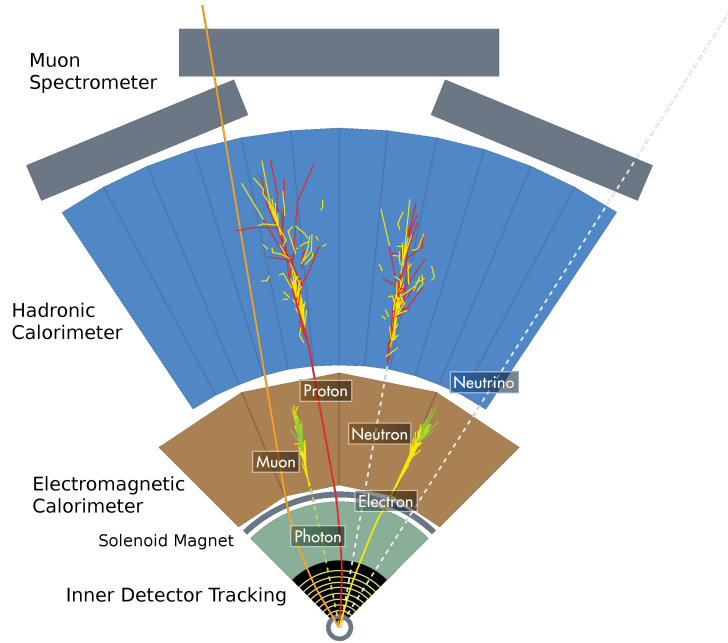


Figure 2.4: Computer generated image representing how ATLAS detects particles. Image modified from [65].

The long-lived particles produced at the interaction point will travel outwards, first encountering the inner detector, a collection of tracking detectors based on semiconducting or gaseous material. Charged particles ionize the material along their trajectory, allowing the precise reconstruction of their tracks. Affected by the strong homogeneous magnetic field of the solenoid, their trajectory follows a helical pattern with curvature revealing the particles’ momenta and sign of charge. The tracker features a high resolution such that a displaced vertex due to a small distance travelled by relatively short-lived particles such as  $b$ -hadrons or  $\tau$ -leptons can often be identified. Uncharged particles are not interacting with the tracker. The particles’ energy is measured in the next-outer layers, the calorimeters, made of alternating layers of absorbing (typically high- $Z$ ) and active material. The electromagnetic calorimeter is designed to absorb and detect light electromagnetically interacting particles such as electrons or photons. The hadronic calorimeter, being much thicker, is optimized to absorb and detect hadrons  $h$ , often in the form of hadronic jets, based on their nuclear interactions. The only established long-lived particles which are typically not absorbed in the calorimeters are muons and neutrinos. Muons can still be detected based on their tracks in the muon spectrometer, the outermost layer, with their tracks being bent by the magnetic field of the toroid magnet. The presence of neutrinos can only be inferred from transverse momentum imbalances  $E_T^{\text{miss}}$  among detected particles.

Leptons	Vertexing	Tracking	ECAL	HCAL	Muon Cham.
$e^\pm$	×	$\vec{p}$	$E$	×	×
$\mu^\pm$	×	$\vec{p}$	✓	✓	$\vec{p}$
$\tau^\pm$	✓×	✓	$e^\pm$	$h^\pm; 3h^\pm$	$\mu^\pm$
$\nu_e, \nu_\mu, \nu_\tau$	×	×	×	×	×
Quarks					
$u, d, s$	×	✓	✓	✓	×
$c \rightarrow D$	✓	✓	$e^\pm$	$h$ 's	$\mu^\pm$
$b \rightarrow B$	✓	✓	$e^\pm$	$h$ 's	$\mu^\pm$
$t \rightarrow bW^\pm$	$b$	✓	$e^\pm$	$b + 2$ jets	$\mu^\pm$
Gauge bosons					
$\gamma$	×	×	$E$	×	×
$g$	×	✓	✓	✓	×
$W^\pm \rightarrow \ell^\pm \nu$	×	$\vec{p}$	$e^\pm$	×	$\mu^\pm$
$\rightarrow q\bar{q}'$	×	✓	✓	2 jets	×
$Z^0 \rightarrow \ell^+ \ell^-$	×	$\vec{p}$	$e^\pm$	×	$\mu^\pm$
$\rightarrow q\bar{q}$	$(b\bar{b})$	✓	✓	2 jets	×

Table 2.1: Signatures of the elementary particles of the SM in the ATLAS detector. A check indicates that the particle can principally be detected by the respective method. A cross means, that it can't. Other symbols indicate either kinematic variables that can be inferred or decay products of the particle that are detectable using the respective method. Modified from [66].

This requires ATLAS to be hermetic, meaning that its acceptance covers almost  $4\pi$  in solid angle. Table 2.1 lists the traces elementary particles leave in the ATLAS sub-detectors. All subsystems of the detector, with a focus on the calorimeters, are explained in the following.

### 2.2.1 The Inner Detector

The ATLAS inner detector is designed to provide high-resolution charged particle tracks for momentum measurements, particle identification as well as the reconstruction of primary and secondary vertices. From innermost to outermost it consists of the Pixel Detector, the Semiconductor Tracker and the Transition Radiation Tracker, all of them enclosed in the 2 T homogeneous field of the solenoid magnet which extends over 5.3 m in length and 2.5 m in diameter. A graphical representation of the inner detector can be found in Figure 2.5. The Pixel Detector consists of 4 layers in the central “barrel” region and 3 disc-shaped layers as end-caps, housing in total 104.5 million semiconducting pixel sensors. Due to the high track density close to the interaction point they are of small size providing an intrinsic accuracy of  $10 \mu\text{m}$  in  $R - \phi$  and  $115 \mu\text{m}$  in  $z(R)$  for the barrel (end-caps). The high radiation environments makes high demands on the radiation hardness of the sensors,

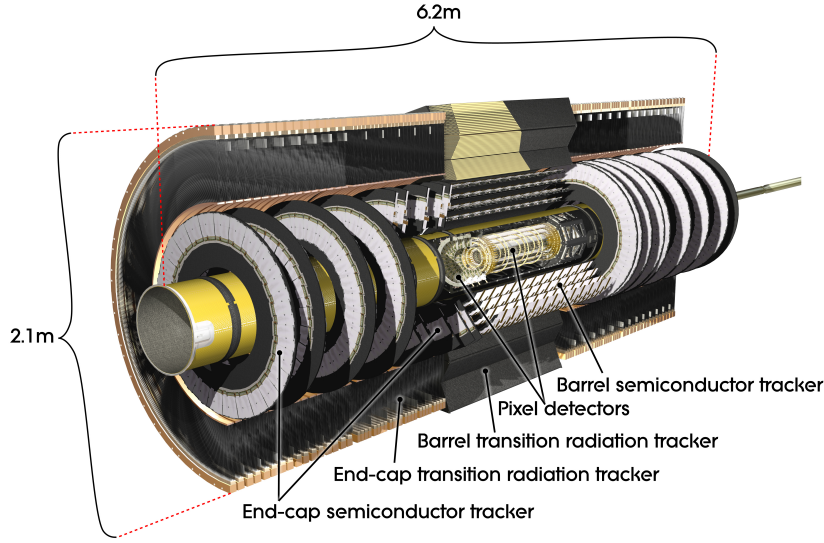


Figure 2.5: Computer generated image of the ATLAS inner detector [67].

which are therefore operated at sub-zero temperatures and are read out using a chip which is directly connected to the sensor. The Semiconductor Tracker consists of 4 barrel layers and 9 layers per end-cap. In contrast to the Pixel Detector each layer contains 6.3 million semiconducting strip sensors instead of pixels, providing with  $16\ \mu\text{m}$  a similar resolution in  $R-\phi$ , but a coarser resolution of  $580\ \mu\text{m}$  in  $z(R)$  for the barrel (end-caps). The advantage of the strip layout is a large area of  $61.1\ \text{m}^2$  that can be covered cost-effectively. The detection principle of both sub-detectors is based on a p-n junction, where traversing charged particles can create electron-hole pairs in the depletion zone, which then follow an applied voltage gradient creating a signal. The signals are combined into a set of space points forming the track. The particle's momentum and charge is inferred from the curvature of the track due to the Lorentz force. This way, tracking is provided over the range of  $|\eta| < 2.5$ . The Transition Radiation Tracker extends to  $|\eta| < 2.0$  with a total of 400000 straw tubes running parallel (perpendicular) to the beam in the barrel (end-caps). They are filled with a mixture of gaseous xenon, carbon-dioxide and oxygen which can be ionized by traversing charged particles. The freed charges are collected by gold coated tungsten wires serving as anode in the tube's center opposed to the cathode tube. The straws have a diameter of 4 mm and a length of 40-75 cm allowing for an average of 36 hits per traversing particle. The resolution amounts to  $130\ \mu\text{m}$  in  $R-\phi$  and 75-150 cm in  $z(R)$  in the center (end-caps). In addition, the straws are coated with a polyimide film provoking transition radiation with intensity inversely proportional to the mass of a traversing charged particle. Since electrons are much lighter than the other charged particles such as  $\pi^\pm$ , the transition radiation can be used to identify electrons. Combining the information of all inner detector components the ATLAS inner detector achieves a transverse impact parameter resolution of  $22.1\ \mu\text{m}$  and a relative momentum resolution  $\sigma_p/p$  of  $4.83 \times 10^{-4} \text{GeV}^{-1} \times p_T$  [68]. The amount of inner detector material is kept as low as possible to minimize energy losses, resulting in

radiation lengths<sup>2</sup> increasing with  $|\eta|$  between 0.1 and 1 [69]. For the work at hand, the inner detector information is not directly used to determine the observables of the analysis, but indirectly for calibration and validation purposes.

### 2.2.2 The Calorimeters

The two ATLAS calorimeters measure the energy of incident particles by their absorption. The electromagnetic calorimeter is optimized to stop light electromagnetically interacting particles such as electrons and photons, whereas the hadronic calorimeter is adapted to absorb hadrons based on their nuclear interactions. Therefore in contrast to the tracker, the calorimeters must consist of dense and ideally high- $Z$  absorber material in which incident particles lose their energy through their respective interactions provoking a shower of secondary particles. These in turn provoke a signal in the active material spatially located behind the absorber via ionization or scintillation. Absorber and active material alternate many times within the calorimeter layers (sampling calorimeter). With a total length of about 12 m and a 8.5 m outer diameter, the ATLAS calorimeter extends over a range of  $|\eta| < 4.9$ . Different materials and techniques are used to meet the different requirements posed by the physics processes and the radiation environments. A graphical representation of the ATLAS calorimeters is given in Figure 2.6.

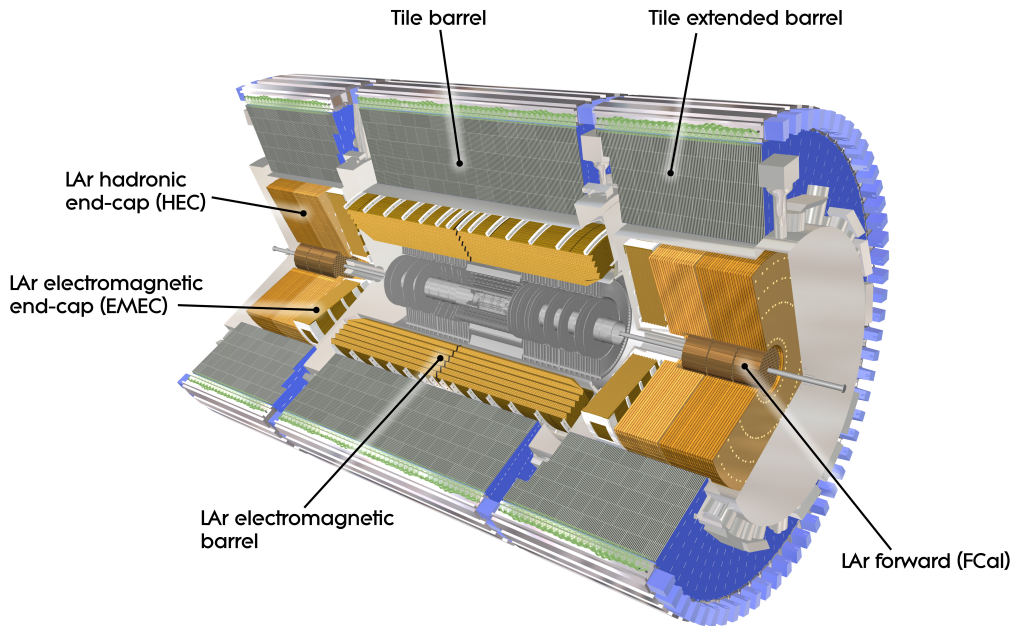


Figure 2.6: Computer generated image of the ATLAS calorimeters [70].

<sup>2</sup>The radiation length is defined as the distance a high-energy electron travels in a material until its energy is reduced by a factor of  $e$  due to bremsstrahlung.

The calorimeter parts closest to the beam pipe (the electromagnetic barrel and end-caps as well as the hadronic end-caps and forward calorimeters) use liquid argon as active material, which has been chosen for its stable, linear response and its radiation hardness (Liquid Argon Calorimeter). The solenoid magnet and the barrel calorimeter share the same cryostat and likewise the electromagnetic and hadronic end-cap components. The calorimeter parts furthest away from the beam pipe face a less dense particle influx and radiation environment, thus they can be made of cost-effective steel absorbers alternating with scintillating tiles operated at room temperature (Tile Calorimeter).

### The Electromagnetic Calorimeter

The electromagnetic calorimeter (ECAL) measures the energy of particles, such as electrons and photons, based on their electromagnetic interactions. The cross-section of the elementary processes by which particles traversing matter lose their energy is energy dependent. In the GeV range electrons and photons lose their energy in the absorber dominantly due to bremsstrahlung and pair-production, inducing an electromagnetic cascade of lower energetic secondary particles. Eventually, as the cascade develops, the energies of the secondary particles drop to the MeV range where ionization and the photo-effect become dominant and allow detection in the active material. The energy dependence of the elementary processes by which an electron or photon passing through lead loses its energy is given in Figure 2.7.

The ECAL consists of a barrel part ( $|\eta| < 1.475$ ) and two end-cap components ( $1.375 < |\eta| < 3.2$ ). Both use accordion-shaped lead plates as absorber material which are interleaved with 3 copper electrodes - the inner two at the high-voltage potential and the outer

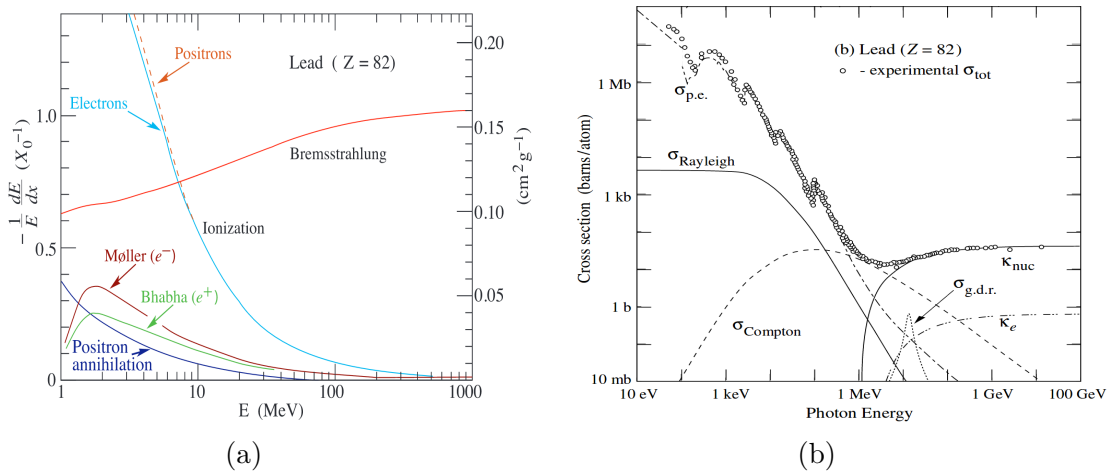


Figure 2.7: Energy dependence of the elementary processes by which an electron or photon passing through lead loses its energy. (a) Fractional energy loss per radiation length in lead as a function of electron or positron energy for various processes. (b) Photon total cross-section and contributions of different processes as a function of energy in lead. [71]

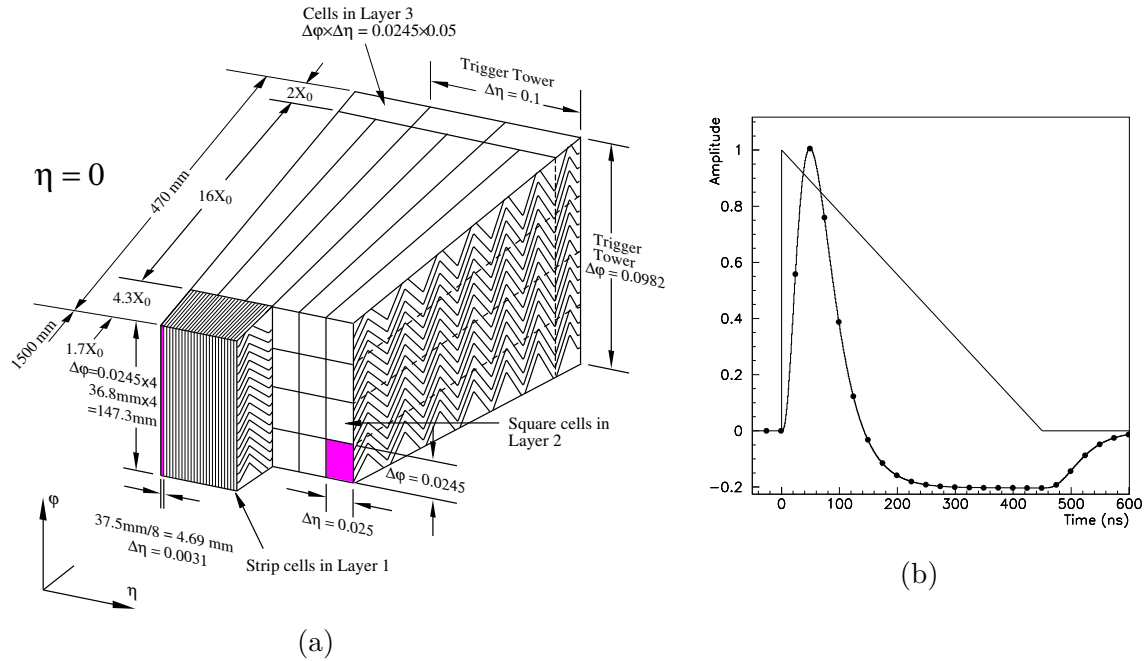


Figure 2.8: (a) Layout and dimensions of the sampled accordion-geometry of the ECAL at  $\eta = 0$ . (b) Amplitude of a signal current pulse of a liquid argon calorimeter cell as a function of time before (straight line) and after (dotted line) bi-polar shaping. [72]

one for signal readout via capacitive coupling. The accordion-shaped geometry naturally provides a full coverage in  $\phi$  without acceptance losses due to cracks as well as fast signal extraction capabilities. The barrel part, tuned for precision measurements, is segmented in R-direction into 3 samplings of decreasing granularity, whereas the end-cap consists of 2 samplings. The layout and dimensions of the sampled accordion-geometry at  $\eta = 0$  is given in Figure 2.8.

Lead has been chosen as absorber material for its intrinsic short radiation length of 0.56 cm. The lead absorbers, totalling to 4096 plates, vary in thickness between 1.13 and 1.54 mm, optimized to achieve a minimum of 24 (26) radiation lengths in the barrel (end-caps) while maintaining a high resolution at average energies and given spatial constraints. Secondary particles ionize the liquid argon which is flowing through the  $\sim 2$  mm sized gaps between the plate-electrodes. Their operating voltage of  $\sim 2000$  V corresponds to ion drift times of about 450 ns. Since the liquid argon is constantly replaced, it does not suffer any radiation damage over the course of the experiment. Any incident particle will already have traversed between 2 and 5 radiation lengths of upstream material before it reaches the first lead absorber. To partially compensate the associated loss in resolution, a presampler layer made of just the active material between electrodes is added before the first layer of the electromagnetic layer. It estimates the energy lost by collecting parts of the secondary particles of upstream interactions. Figure 2.8(b) illustrates the general shape of calorimeter signals by the example of a EM liquid argon cell as function of time as produced in the

detector and after it underwent a bi-polar shaping. The advantage of signal shaping is that many overlaying signals, i.e. from electronic and pile-up noise in previous and successive bunch crossings, cancel each other due to the zero net area of the bi-polar shape, thus ensuring an automatic baseline subtraction.

The energy resolution of the calorimeter is given by

$$\frac{\sigma(E)}{E} = \frac{N}{E} \oplus \frac{S}{\sqrt{E}} \oplus C. \quad (2.2)$$

The first term includes the noise term  $N$  with contributions from electronic and pile-up noise. It dominates the total resolution at relatively low energies  $E < 30$  GeV. The second term contains a statistical component  $S$  from shower evolution and the detector sampling. It becomes dominant for energies  $30 \text{ GeV} < E < 400 \text{ GeV}$ . At even higher energies, the constant term,  $C$ , becomes significant, accounting for the detector geometry, uninstrumented areas and non-uniformities in the response. In the barrel the resolution has been measured with electron test beams to  $\frac{\sigma_E}{E} = \frac{10.1\%}{\sqrt{E}} \oplus 0.17\%$  [73] and in the end-caps to  $\frac{\sigma_E}{E} = \frac{12.1\%}{\sqrt{E}} \oplus 0.4\%$  [74].

Hadrons typically do not lose all their energy in the ECAL, even if they are charged. They are much heavier than electrons which suppresses their rate of bremsstrahlung (proportional to  $m^{-4}$ ) and uncharged hadrons do not interact electromagnetically at all. These particles can be fully absorbed in the hadronic calorimeter.

### The Hadronic Calorimeter

The hadronic calorimeter (HCAL) is optimized to measure the energy of hadronically interacting particles, such as protons, neutrons, pions and kaons. These primary particles typically cause a hadronic shower based on their inelastic nuclear interactions with the absorber material, which is much more complex than an electromagnetic shower.

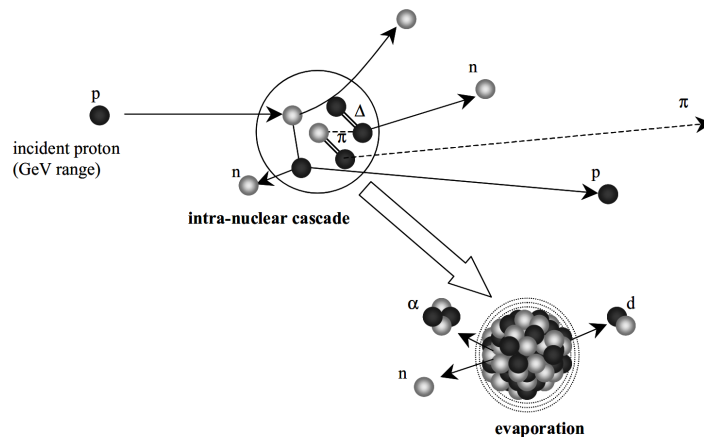


Figure 2.9: Sketch of a spallation process resulting in an intra- and internuclear cascade [75].

The most abundant process in hadronic showers is called *spallation* and is simplistically shown in Figure 2.9, where an incident proton interacts with a nucleus, releasing a cascade of secondary particles and nuclear fragments. In the first and highest energy stage of the hadron-nucleon interaction, the nucleon is split-up forming a string of  $q\bar{q}$  pairs in-between. The string eventually undergoes fragmentation and hadronization with particles like pions and kaons in the final state whose multiplicity scales with energy. In the medium to low energy regime the incident hadron traverses the nucleus at which it transfers energy to protons and neutrons, causing an intranuclear cascade with some neutrons and protons escaping the nucleus. The outgoing particles then interact with further nuclei downstream, leading to an internuclear cascade. The nuclei themselves remain in an excited state and relax by fission or evaporation, once again ejecting photons, nucleons or nuclear fragments. A good fraction of secondary particles are  $\pi^0$  mesons which quickly decay into two photons causing a detectable electromagnetic cascade. As the energy of the hadronic shower constituents decreases during the shower evolution, around 80% of the energy of the low energy charged hadrons can be visibly detected as well via ionization in the active material. Also the energy of slow neutrons can partially be recovered in the active material due to their energy and momentum transfer to charged nuclei. However the energy which is carried by escaping neutrinos or muons is lost undetected, as is the binding energy from the nuclear break-ups. The energy fractions deposited according to the different mentioned mechanisms is given in Figure 2.10 as a function of incident proton energy.

The energy losses as well as the different calorimeter responses to the hadronic and electromagnetic shower components require a sophisticated calibration procedure to compensate

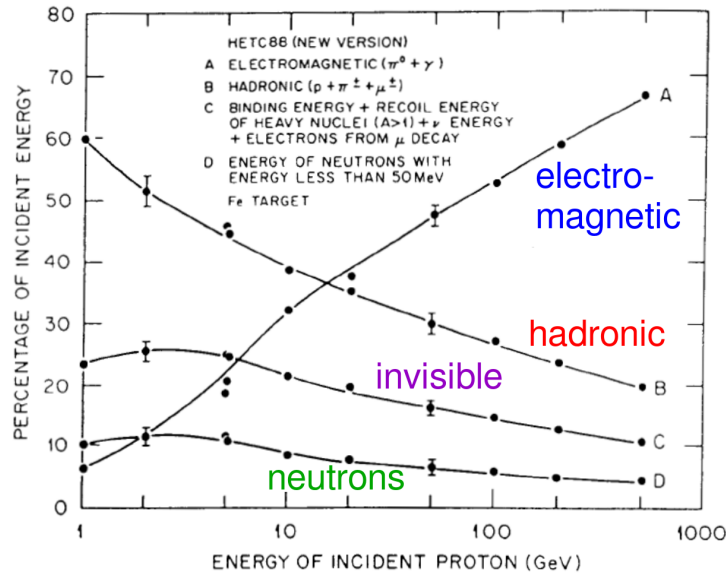


Figure 2.10: Fractional energy deposition of a proton incident on an iron target according to electromagnetic showers, charged particle production, neutrons and undetectable energy as a function of the proton energy. Figure modified from [76].

the losses in resolution. The calibration procedure brings the jets from the scale of the detector response at the *electromagnetic energy scale* to the more accurate *jet energy scale* (JES). This is explained in more detail in Chapter 5.1.

The nuclear interaction length  $\lambda_{int}$ , defined as the mean distance travelled by a hadronic particle until its energy is reduced by a factor of  $e$  due to inelastic nuclear interactions, is much larger than the radiation length  $\chi_0$  for electromagnetic particles, with  $\frac{\lambda_{int}}{\chi_0} \sim A^{\frac{1}{3}}$ . Thus, hadronic showers build up more slowly and are spatially more extended, requiring the HCAL to be significantly thicker than the ECAL.

The ATLAS HCAL is located radially behind the ECAL and consists of the tile barrel and extended barrel ( $|\eta| < 1.7$ ), the hadronic end-cap ( $1.5 < |\eta| < 3.2$ ) and the forward calorimeter ( $3.1 < |\eta| < 4.9$ ). The tile calorimeters have a thickness of 1.97 m corresponding to approximately  $7.4\lambda_{int}$ . Each barrel consists of 64 modules of size  $\Delta\phi \sim 0.1$  which are sketched in Figure 2.11. They are made of steel plates alternating periodically with scintillating tiles with a volume ratio of  $\sim 4.7 : 1$  and a corresponding readout optic.

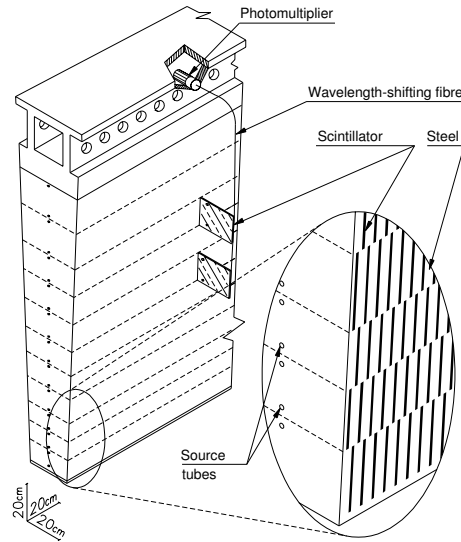


Figure 2.11: Sketch of the mechanical arrangement and optical readout assembly of a tile module. [59]

Steel provides a relatively short interaction length of  $\lambda_{int} \approx 16.8$  cm, which is even shorter than for lead and very cost efficient. The scintillating tiles are made of a polystyrene matrix as base material doped with paraterphenyl as a scintillator. In the scintillator, ionizing particles produce scintillation light with intensity proportional to their energy. The light is collected by two wavelength-shifting optical fibres at both ends of the tiles and transmitted to a photomultiplier, a pulse shaper and a compressor, resulting in a signal pulse of fixed width (50 ns full width at half maximum) with amplitude proportional to the energy deposited in the cell [77][78]. To account for the showers from the passive material in the gap between the tile central and tile extended barrel, this “crack region” is instrumented with additional thin scintillating tiles. The tile calorimeter reaches its design

resolution with  $\frac{\sigma_E}{E} = \frac{52.7\%}{\sqrt{E}} \oplus 5.7\%$  as determined from pion test beams [79].

Due to the demanding rate and radiation environment in the forward region, the hadronic end-cap and the forward calorimeter use copper or tungsten as absorber plates, alternating with liquid argon as active material and a readout design similar to the ECAL. The hadronic end-cap uses plates of 25-50 mm thickness layered in the z-direction and separated by a 8.5 mm gap filled with liquid argon. The forward calorimeter is required to be extremely dense due spatial limitations and therefore uses 250-375  $\mu\text{m}$  sized tube-gaps of liquid argon embedded into a matrix of absorber, rather than plates of absorber immersed into liquid argon. The absorber is made of copper in the first layer, followed by tungsten in the second and third layer. Pion test beam measurements determine the resolution to  $\frac{\sigma_E}{E} = \frac{70.6\%}{\sqrt{E}} \oplus 5.8\%$  in the hadronic end-cap [80] and to  $\frac{\sigma_E}{E} = \frac{94.2\%}{\sqrt{E}} \oplus 7.5\%$  in the forward calorimeter [81].

The only electromagnetically interacting particle which is typically not absorbed in the calorimeters due to its high invariant mass, is the muon. It can be tracked in the muon spectrometer, which is described in the following.

### 2.2.3 The Muon Spectrometer

The muon spectrometer, located outside of the calorimeters has the purpose to measure the momenta of muons according to the curvature of their trajectory in the 2-8 T field of the toroid magnets. In the barrel region it consists of three cylindrical shells of precision tracking chambers around the beam axis at radii of 5 m, 7.5 m and 10 m. In the end-caps the muon chambers are arranged in 4 large wheels perpendicular to the beam axis located at distances of  $|z| \approx 7\text{ m}, 11\text{ m}, 14\text{ m}$  and  $22\text{ m}$  from the interaction point, covering a pseudo-rapidity range of  $|\eta| < 2.7$ . Four different types of muon chambers are employed: Monitored Drift Tubes (MDTs) and Cathode Strip Chambers (CSCs) provide precision coordinate measurements in the bending plane, whereas Resistive Plate Chambers (RPCs) and Thin Gap Chambers (TGCs) deliver fast tracking information only a few tens of nanoseconds after the passage of the particle to provide reliable bunch crossing assignments and triggering. The MDTs consist of 30 mm diameter drift tubes, operating with a 93 : 7 mixture of Ar and CO<sub>2</sub> at 3 bar. Ionization electrons are collected by a 50  $\mu\text{m}$  diameter tungsten-rhenium wire at a potential of 3080 V in the tube's center and their drift times give information about the muons' exact trajectory. The MDTs cover a pseudo-rapidity range of  $|\eta| < 2.7$  and are present in every layer of the muon system except in the  $2.0 < |\eta| < 2.7$  range of the innermost end-cap layer, where CSCs are employed due to their higher rate capability and time resolution. CSCs consist of arrays of positively charged "anode" wires and segments of perpendicular and parallel negatively charged "cathode" copper strips immersed in a 80 : 20 mixture of Ar and CO<sub>2</sub>. Interpolation between charges induced to neighboring strips following ionization yields the precision coordinates in the bending plane for perpendicular cathode strips and the transverse coordinate for parallel cathode strips respectively. The RPCs consist of two highly resistive parallel electrode-plates separated at a distance of 2 mm enclosing a (flourinated)hydrocarbon and SF<sub>6</sub> gas mixture. At an

applied voltage of 9.8 kV, a gas molecule which was ionized by a traversing muon causes an avalanche along the ionizing tracks towards the anode. A signal is read out via capacitive coupling resulting in relatively short signal widths of 5 ns full width at half maximum, which allows the RPCs to be used reliably for bunch crossing identification. RPCs are employed for fast triggering in the barrel ( $|\eta| < 1.05$ ), whereas in the end-cap ( $1.05 < |\eta| < 2.4$ ) TGCs are used. These consist of an array of wires at 2.9 kV (anode) running through a chamber with grounded conducting walls serving as cathode. The chamber is filled with a highly quenching gas mixture of CO<sub>2</sub> and n-pentane, which is ionized by traversing muons. The high electric field and the small distance between wires lead to a high time-resolution on the resulting avalanche signals which is crucial for the purpose of triggering. As it is the case for the inner detector, the muon spectrometer is not directly used to determine the observables of the analysis subject to this work, but indirectly for calibration and validation purposes.

## 2.3 The ATLAS Trigger and Reconstruction System

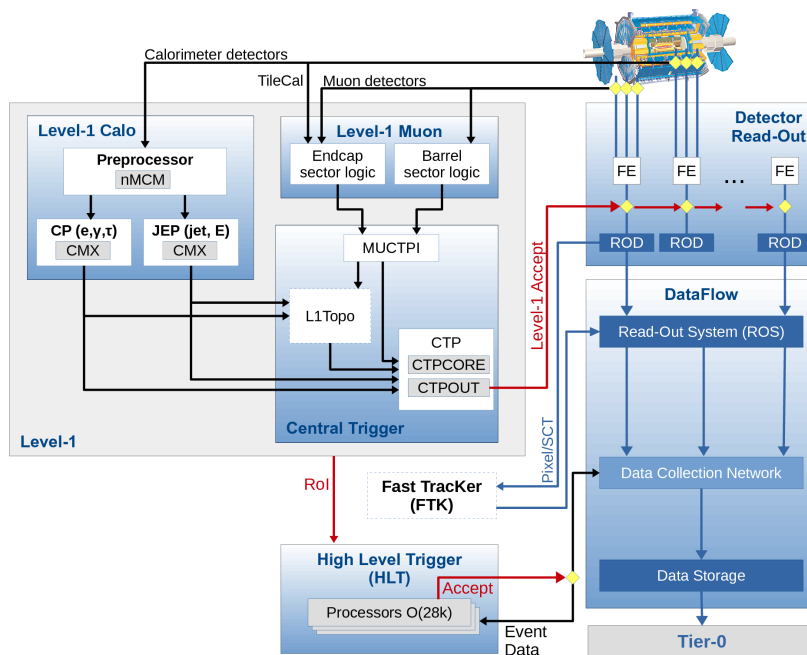


Figure 2.12: Overview of the ATLAS trigger system [82].

At each of the LHC interaction points, bunch crossings occur at a rate of 40 MHz. A fully recorded event containing the information of all final state products of one bunch crossing has a size of about 1.6 MB and takes a CPU about 15 s to reconstruct. This makes it obvious that neither disc space or bandwidth, nor reconstruction computing resources of any present day data acquisition and reconstruction system allow the recording of every event. There has to be some kind of selection reducing the recording rate by several orders

of magnitude. This is the purpose of the ATLAS trigger system, which reconstructs the event in parallel to the run “online” in coarse granularity and decides whether the event is interesting and worth saving. Here “interesting” means that the event fulfills one of several conditions, called *trigger items*, which are listed in the *trigger menu*. These trigger items specify conditions i.e. on the particle content in the event as well as kinematic thresholds and are motivated by the experimental searches and measurements. Due to the cleaner signature, a slight preference is put on leptonic over jet trigger signatures, meaning that a higher fraction of the bandwidth capacities is reserved for leptonic trigger signatures and therefore their kinematic thresholds are looser compared to jet trigger signatures. The ATLAS trigger system is organized in two levels - the Level-1 (L1) Trigger and the High Level Trigger (HLT) - with an overview given in Figure 2.12.

### 2.3.1 The Level-1 Trigger

The L1 Trigger is based on custom-made hardware, utilizing mostly ASICs and FPGAs, and uses coarse granularity information from the calorimeters and the muon systems. It determines a trigger decision based on  $E_T$  sums, such as missing transverse energy and total energy, as well as multiplicities of objects such as photons, electrons,  $\tau$ -leptons, muons and jets exceeding certain energy thresholds. Inner detector information is not used at L1. It consists of four sub-systems. The level-1 calorimeter trigger (L1Calo) and the level-1 muon trigger (L1Muon) both process the data from their respective sub-detectors. The level-1 topological processor (L1Topo) combines the information of L1Calo and L1Muon and extracts topological information of the event. Finally, the central trigger processor (CTP) takes the trigger decision based on the combined information from the aforementioned L1 sub-systems. The data input to the L1Calo system are 7200 analog sums of signals from calorimeter segments which are roughly radially aligned - so-called *trigger towers*. This significantly reduces the granularity, especially the radial component which is summed over. The trigger tower signals enter first the L1Calo *PreProcessor* (PPr) where they are digitized, assigned to a certain bunch crossing and calibrated to a transverse energy. The  $E_T$  values are then distributed in parallel to the *Cluster Processor* (CP) and the *Jet/Energy Processor* (JEP). Both processors identify localized energy depositions using sliding window algorithms. In the CP, this process is optimized towards photon, electron and  $\tau$ -lepton objects, whereas the JEP is specialized on jet identification and calculation of  $E_T$  sums. The coordinates of the windows containing localized maxima define the objects’ regions of interest (RoIs).

The L1Muon trigger is based on signals from the RPCs and TGCs which provide the required timing resolution for bunch crossing identification. It fires upon coincidences of hits in different trigger stations within a road leading towards the interaction point.

All candidate objects above certain thresholds as identified by L1Calo and L1Muon are input to topological algorithms at L1Topo. These determine whether thresholds of complex physics quantities, such as angular distances and the invariant mass of objects are exceeded. The multiplicities of objects exceeding a kinematic or topological threshold as well as  $E_T$  sum information are inputs to the CTP, where they are compared to a programmable

L1 trigger menu, consisting of up to 512 trigger items. Each trigger item is a logical combination of multiplicity requirements on objects above a given threshold. In addition, every trigger item has a prescaling factor which is used to reduce the amount of events accepted by a trigger item. For example for a prescaling factor of 10, only one of 10 events, fulfilling the trigger requirement, will be accepted.

If the logical OR of all trigger items is fulfilled, an L1-accept (L1A) is fired and the event is read out by dedicated readout drivers (RODs) allowing it to be reconstructed by the HLT. Until L1 determines its L1A decision, the raw event information needs to be buffered. This happens in pipeline memories granting the L1 trigger system a time frame of  $2.5 \mu\text{s}$ . This way the total rate is reduced from 40 MHz to 100 kHz.

### 2.3.2 The High Level Trigger

The HLT, a cluster of  $\sim 40000$  commercial CPUs, is seeded with the L1 trigger items consisting of the L1 trigger items and their associated RoIs. The HLT reconstructs all events flagged with an L1A at full granularity using one or more reconstruction chains which depend on the seeding trigger items. Each reconstruction chain, or *trigger chain*, determines a sequence of algorithms using increasing amounts of detector information which is both necessary and sufficient in order to ensure both fast and reliable determination of particle content, kinematics and topology. Trigger chains consist of feature extraction algorithms (FEXes) interleaved with hypothesis algorithms (HYPOs). FEXes perform CPU-intensive operations such as the extraction of detector data and identification of features like tracks and calorimeter-clusters. To save time and computing resources, FEXes often request detector data from within the respective RoI only, which is especially important for inner detector data. HYPOs subsequently determine whether an extracted feature satisfies a given criterion (e.g. track-cluster match,  $E_T$  threshold, prescale, etc.) at the current stage of the chain. When the required criteria in a HYPO are not met, the chain is not processed

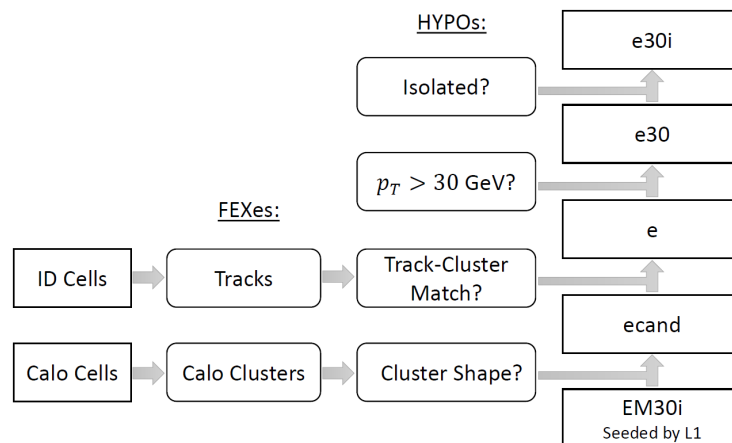


Figure 2.13: Illustration of the HYPOs and FEXes invoked at the different stages of the trigger chain for an electron object.

Trigger	Typical Offline Selection	Trigger Threshold		Peak Rates	
		Level-1	HLT	Level-1	HLT
Single Jet	Jet $p_T > 420$ GeV	100 GeV	380 GeV	3 kHz	38 Hz
Single Electron	Isolated $e$ $p_T > 27$ GeV	22 GeV	26 GeV	20 kHz	133 Hz
Single Muon	Isolated $\mu$ $p_T > 27$ GeV	20 GeV	26 GeV	13 kHz	133 Hz
Single Photon	Photon $p_T > 145$ GeV	22 GeV	140 GeV	20 kHz	30 Hz
$E_T^{\text{miss}}$	$E_T^{\text{miss}} > 200$ GeV	50 GeV	110 GeV	6 kHz	230 Hz

Table 2.2: The lowest unprescaled single object triggers and their thresholds and peak rates at Level-1 and the HLT from the 2016 trigger menu [83].

further. If no active chain is left, the event is discarded. Thereby, the possibility for early rejection is another mechanism to save computing resources within the HLT. The typical nomenclature of a trigger chain reflects the object of interest, its multiplicity, the exceeded thresholds and additional criteria. For example HLT\_2e30i indicates two electrons with  $p_T > 30$  GeV which are isolated. Figure 2.13 illustrates the algorithms invoked at the different stages of a trigger chain at the example of a single e30i electron trigger element. The lowest unprescaled L1 and HLT single object triggers and their respective rates during 2016 are listed in Table 2.2. The HLT decision-making happens on average within  $\sim 200$  ms while the data is temporarily saved in a data collection network. If at least one HLT trigger chain is passed, the event is directed into an *output stream* and recorded for offline reconstruction. At this point the total rate is reduced to 1 kHz.

### 2.3.3 Output Streams and Reconstruction

An event accepted by the HLT will be saved into various output streams and reconstructed at the ATLAS offline reconstruction site *Tier-0* at full granularity using the readout of all ATLAS sub-systems. Events that were triggered by the physics trigger menu are reconstructed from the main physics stream. Conventional ATLAS physics analyses use the main physics stream as their main source of input. There are additional data streams such as the calibration streams, which are dedicated to events triggered for calibration purposes, for example from empty bunch crossings, or the express stream which provides fast access to data quality control and monitoring data and contains only a subset of the total events. Tier-0 starts the reconstruction as soon as the first triggered events from a run arrive and is designed to have finished the reconstruction of the full run on average within one LHC filling cycle. A special case among the data streams is the so-called *Delayed Stream*. Here, the data from dedicated triggers is not reconstructed, but saved as raw cell-level data to be reconstructed when required at a later time when Tier-0 is otherwise idle, for example during an LHC technical stop. The key to the Trigger-Object Level Analysis as presented in this thesis, is an additional data stream, called the *Data Scouting Stream*. Since its implementation is dedicated to this particular analysis, it is reviewed in detail in Chapter 4.1.

## Chapter 3

# Reconstruction of Dijet Events

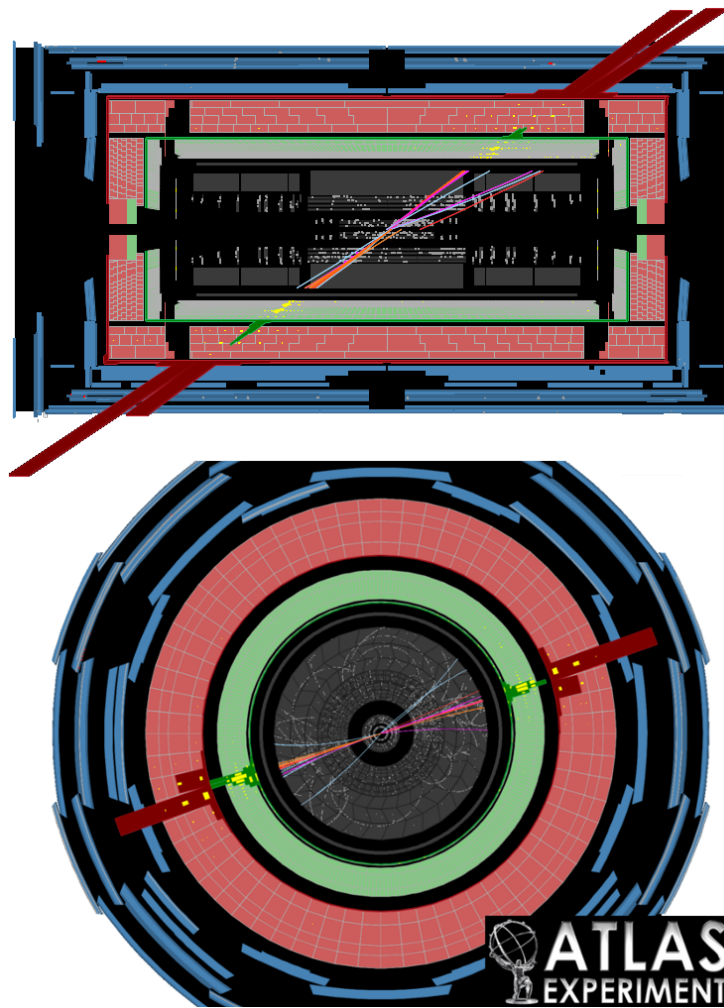


Figure 3.1: ATLAS event display of a dijet event with dijet invariant mass of 2.8 TeV in a radially logarithmic representation. The leading jet has a  $p_T = 310$  GeV at a rapidity  $y = -2.0$ . The subleading jet has a  $p_T = 280$  GeV at a rapidity  $y = 2.5$ . Only tracks with  $p_T > 2$  GeV are shown for the display. The pile-up activity is extraordinarily low and not representative for the events analyzed in this work. Figure modified from [84].

### 3.1 Jet Reconstruction

The hadrons of the particle jet produce a distinct signature in the detector. Charged hadrons will leave tracks in the tracking system and both the neutral and the charged hadrons will generate a hadronic shower in the calorimeters which is modelled via string fragmentation and inter- and intranuclear cascades. An ATLAS event display of a dijet event in the detector at a dijet invariant mass of 2.8 TeV is given in Figure 3.1. The image gives an impression of the longitudinal and lateral dimensions of the jet and the calorimeter shower in comparison to the calorimeter segments and the ATLAS detector as a whole. The jet as a whole extends over several calorimeter segments, especially in depth. For the coarse granularity reconstruction at the Level-1 trigger it is therefore sufficient and efficient to use as input signals the analog signal sum of radially aligned calorimeter segments to identify jets as a whole. The full granularity of the calorimeter cells allows to resolve the jet as a combination of energy deposits from the showers of single hadrons. This is realized both in the HLT and in the Tier-0 offline reconstruction where clustering algorithms are employed to resolve the hadronic shower energy deposits and recombination algorithms (*jet algorithms*) are used to combine the clusters into jets in an infrared and collinear safe manner. The underlying event activity in Figure 3.1 is extraordinarily low and not representative for the events analyzed in this work

#### 3.1.1 Level-1 Jet Reconstruction

At L1 the Jet Energy Processor uses a sliding window algorithm (Figure 3.2) based on the coarse granularity of jet elements (neighboring trigger towers adding up to  $0.2 \times 0.2$  in  $\eta - \phi$ ) to identify jets.

Three different window sizes of  $2 \times 2$ ,  $3 \times 3$  and  $4 \times 4$  jet elements are used for the sliding windows corresponding to an area of 0.4, 0.6 and 0.8 in  $\Delta\eta$  and  $\Delta\phi$ , respectively. The windows slide in steps of one jet element at a time through the calorimeter. When the  $E_T$  sum in a window exceeds a certain threshold, it is checked whether this corresponds to a local maximum. This is realized by a  $2 \times 2$  window within the sliding  $2 \times 2$ ,  $3 \times 3$  and  $4 \times 4$  windows which must be a local maximum, meaning that its  $E_T$  sum must be

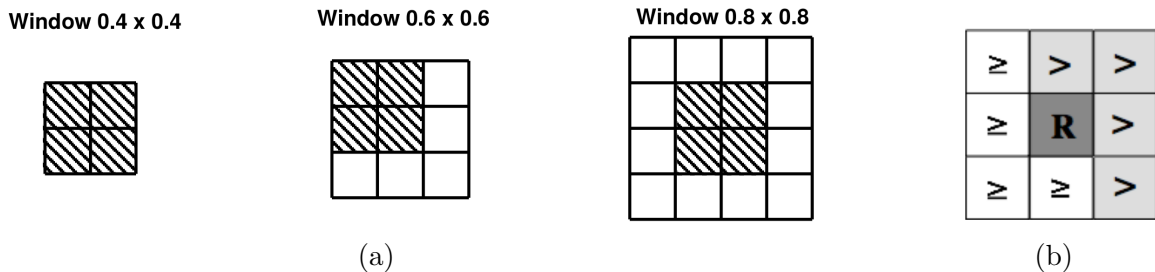


Figure 3.2: The different windows sizes based on  $2 \times 2$ ,  $3 \times 3$  and  $4 \times 4$  jet elements for the sliding window algorithm (a). The  $2 \times 2$  RoI is given by the shaded area. The requirement criterion for a local maximum is illustrated in (b), where R is the RoI window. [59]

greater or greater-equal than its neighbors, as indicated in Figure 3.2(b). For a sliding  $2 \times 2$  and  $4 \times 4$  window the position of the inner  $2 \times 2$  windows is unambiguously fixed as indicated in Figure 3.2(a), but for the  $3 \times 3$  window there are 4 configurations. In this case the configuration with the highest  $E_T$  sum is taken. The L1 jet RoIs are then defined by the positions of the  $2 \times 2$  windows and the  $E_T$  sums in the outer windows denote the jet energies. Larger windows are more efficient because they include more energy, however smaller windows have a better spatial resolution and are able to distinguish between closely neighbored jets.

### 3.1.2 High Level Trigger Jet Reconstruction

The High Level Trigger reconstructs jets at full calorimeter granularity. Upgrades on the HLT infrastructure and the development of more efficient reconstruction algorithms during the first long shutdown of the LHC made it possible to reconstruct jets in a *full scan*. This means that the jet reconstruction algorithms are not restricted to the L1 RoIs but run on the whole calorimeter. Information from the tracking system is available only in the limited spatial regions of the L1 RoIs and is therefore not used by default. The HLT jet reconstruction is initialized when the event is seeded by a L1 jet trigger item. In the first step the calorimeter cell energy deposits are extracted and subjected to a BCID dependent pile-up correction. Afterwards the cells are topologically clustered and the clusters themselves are sequentially combined within a jet algorithm to form a reconstructed calorimeter jet.

#### Topological Clustering

The topological clustering algorithm follows the so-called “420-scheme”. This means that a cluster is seeded by a cell with energy at least 4 standard deviations above the mean electronic + pile-up noise level in that cell. In the second step all neighboring cells with energy above 2 standard deviations are included to form a proto cluster. This step is

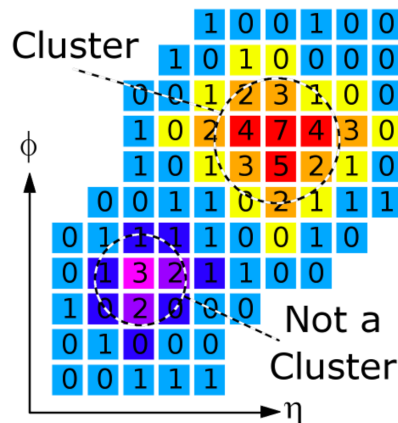


Figure 3.3: Two-dimensional illustration of the topological clustering algorithm [85].

repeated until no additional cells fulfill the energy requirement. In the last step all nearest neighbors are added to the proto cluster without energy requirement.[86] A two-dimensional illustration of the topological clustering algorithm is given in Figure 3.3 as an example.

It may happen that proto clusters originating from different seeds will eventually merge. In these situations a cluster splitting algorithm acts on the cells of the previously defined proto clusters and ensures that in the end each cell representing a local maximum corresponds to exactly one cluster. Cells which can be assigned to two proto clusters will be shared between them and their energy will be separately re-weighted with respect to the energy  $E_{1,2}$  of the adjoint proto clusters and the distance  $d_{1,2}$  to the proto cluster centroids. The weights applied to the energy of the shared cell are

$$w_1 = \frac{E_1}{E_1 + rE_2}, \quad w_2 = 1 - w_1, \quad r = \exp(d_1 - d_2) . \quad (3.1)$$

The resulting topological clusters are “three dimensional energy blobs in the calorimeter that sometimes share cells on the border between them”[86].

### Jet Algorithms

To reconstruct the kinetic variables of the original parton, the associated calorimeter clusters need to be combined into a single jet object in a well defined and collinear/infrared safe manner. In the context of jets infrared safety implies that the constituents included into the jet by the jet algorithm should not change under the soft radiation of an additional object.

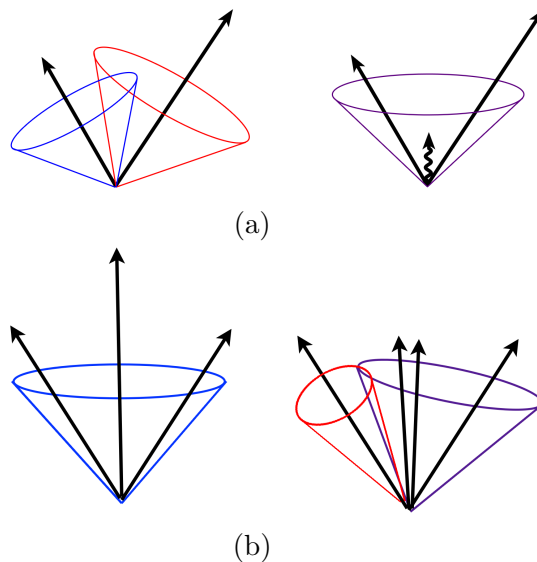


Figure 3.4: Illustration of an infrared unsafe jet algorithm (a), where the soft radiation of an additional object leads to the combination of two jet into a single jet, and a collinear unsafe algorithm (b), where the collinear splitting of an object leads to the splitting of a single jet into two jets. Figure modified from [87].

An example of an infrared unsafe jet definition is given in Figure 3.4(a), where two jets merge when an additional soft object (e.g. from soft gluon radiation) is included. Collinear safety requires the jet to stay invariant under small angle splitting of one constituent into two. Figure 3.4(b) illustrates a collinear unsafe case where one jet is split into two jets due to the collinear splitting of a constituent (i.e. parton splitting). A family of jet algorithms that are both collinear and infrared safe are the so-called *sequential recombination algorithms*. These algorithms successively combine cluster pairs  $(i, j)$  with transverse momenta  $p_{Ti}, p_{Tj}$  into a jet based on two relative distance measures

$$\begin{aligned} d_{ij} &= \min(p_{Ti}^{2p}, p_{Tj}^{2p}) \frac{\Delta R_{ij}^2}{R^2}, \\ d_{iB} &= p_{Ti}^{2p}, \end{aligned} \quad (3.2)$$

where  $R$  is the distance parameter of the jet algorithm and  $p = 1, 0, -1$  defines different recombination schemes corresponding to the  $k_T$  [88], Cambridge/Aachen [89] and the anti- $k_T$  [90] algorithm. The squares guarantee positive distance measures. The jet algorithm operates as follows:

1. Find minima of  $d_{ij}$  and  $d_{iB}$  among all possible clusters  $i$  and pairs of clusters  $(i, j)$ .
2. If  $d_{ij}^{\min} < d_{iB}^{\min}$  combine 4-vectors of clusters  $i$  and  $j$  into a proto jet.
3. If  $d_{ij}^{\min} > d_{iB}^{\min}$  the 4-vector of  $i$  becomes a jet.
4. Repeat until  $d_{ij}^{\min} > d_{iB}^{\min}$  for all clusters  $j$ .

Thus, the different recombination orderings of the recombination schemes become obvious. For the  $k_T$  algorithm nearby clusters with low  $p_T$  will be included first. Cambridge/Aachen jets are the result of a purely geometrical combination of the nearest clusters, regardless of their  $p_T$ . Finally, the anti- $k_T$  algorithm prioritizes nearby clusters with large  $p_T$ . Here “nearby” is expressed with respect to the distance parameter  $R$  which is nominally  $R = 0.4$  in ATLAS.

Figure 3.5 illustrates how the different sequential recombination algorithms reconstruct the jets in the same simulated event. As the  $k_T$  algorithm starts with low  $p_T$  clusters, the proto jet axis can be significantly influenced by the successive addition of higher  $p_T$  clusters resulting in typically irregular shapes. Though not as pronounced, this is also true for the Cambridge/Aachen algorithm. Contrary, in the anti- $k_T$  algorithm the first and largest  $p_T$  cluster largely defines the jet axis and the addition of further lower  $p_T$  clusters does not sizably affect it. For isolated or relatively high- $p_T$  jets this leads to circular jet area shapes of radius corresponding to roughly the radius parameter  $R$  and the highest  $p_T$  cluster at its center. Adjacent lower  $p_T$  jets are typically crescent shaped around the higher  $p_T$  jet. The anti- $k_T$  algorithm is the default algorithm by which jets are reconstructed at the ATLAS HLT.

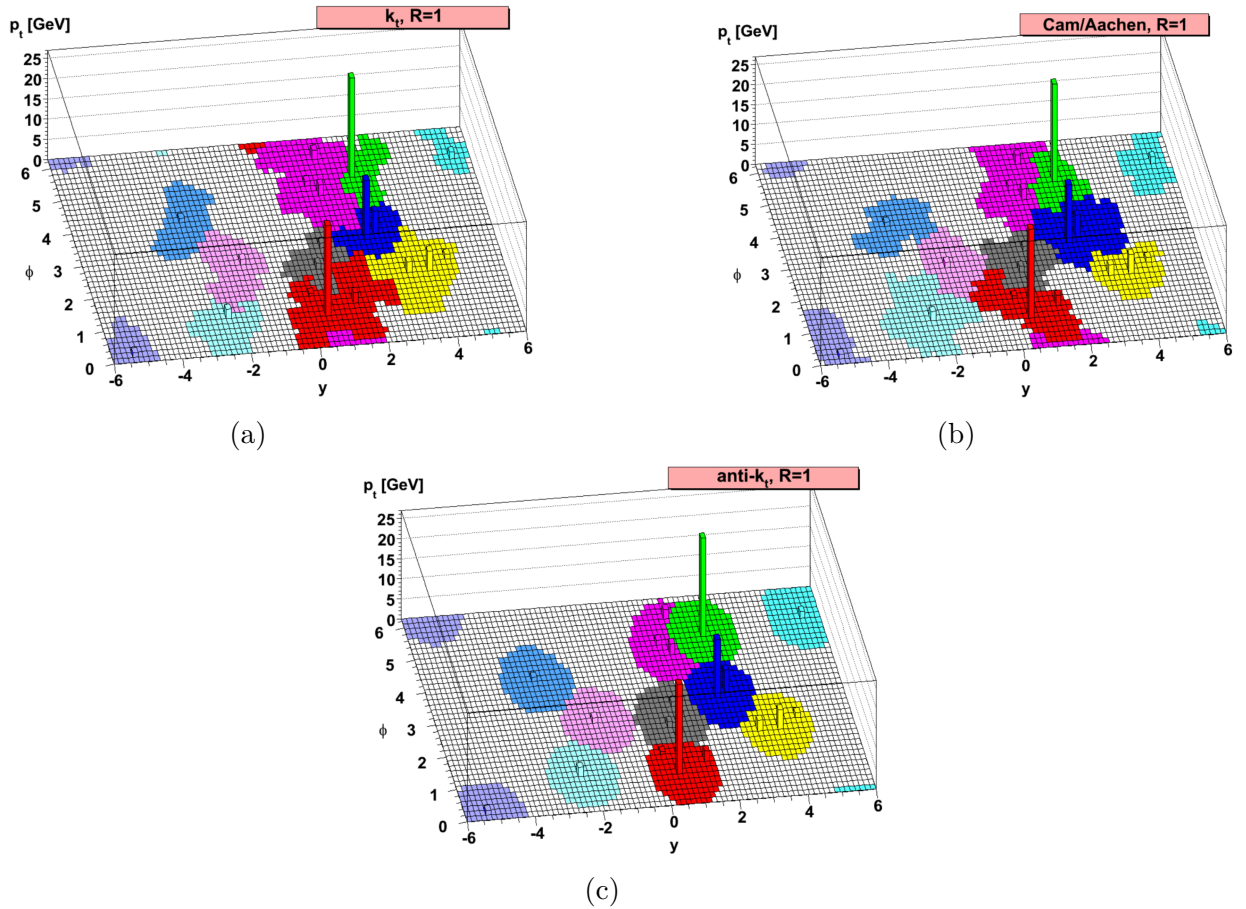


Figure 3.5: Illustration of jet catchment areas according to different sequential recombination algorithms operating on the same simulated event [90].

Within the HLT, the clustering and jet algorithms are executed in a full scan for every L1-accepted event flagged with an L1 jet trigger item, resulting in the reconstruction of all *calorimeter jets* of those events. The jet-related, calorimeter-based algorithms are the same as those employed by the offline reconstruction. RoI based tracking algorithms however are only initialized for the purpose of  $b$ -tagging for individual jets. Therefore the tracking information is not stored in the HLT jet collection unless a  $b$ -jet trigger chain is passed.

### 3.1.3 Offline Jet Reconstruction

The first steps of the offline jet reconstruction are the same as the previously described HLT jet reconstruction, however further jet algorithms and distance parameters are used to retrieve also jets from different jet definitions. In an additional step in the offline reconstruction the sequential recombination algorithms are invoked to operate on tracks as well, leading to the reconstruction of *track jets*. Track jets and calorimeter jets can be matched to each other such that a combination of variables from both jet types can be

used to describe the jet. In most cases however, the calorimeter jet remains the basis for an offline jet with a few variables from the matched track jet and activity in the muon system behind the jet being associated to it. The only difference between calorimeter jets reconstructed offline and at the HLT arises from different algorithms used to calculate the cell energy and timing of signals in the tile calorimeter. The offline algorithms calculate the pedestal<sup>1</sup> on an event-by-event basis in data, whereas the HLT algorithms retrieve the value of the pedestal from a database.

## 3.2 Monte Carlo Simulations

All stages from the proton-proton collision to the reconstruction of jets are emulated in sophisticated Monte-Carlo (MC) simulations [91]. The hard-scattering of physics processes such as QCD  $2 \rightarrow 2$  parton scattering or a BSM process is simulated at *generator level*. The resulting event is evolved according to parton-showering and hadronization models. Particle-level jets at this stage are often referred to as “truth jets”. These are overlaid with simulations of the final states of the underlying event and pile-up interactions. The parametrizations of various settings and approximations of the generators are combined in sets, referred to as *tunes*. The interactions of the final state particles with the absorber-, active- and passive material of the ATLAS detector is simulated using the GEANT4 toolkit [92]. From there on the digitization of simulated signals and the reconstruction of objects is performed by the very same algorithms that are used on the data which ensures a high comparability between both domains. The Monte-Carlo samples used in this work are the following:

- PYTHIA [93] is used as a dijet event generator, simulating both the hard-scatter and the underlying event. LO and optionally NLO matrix elements are evaluated. To model the hadronization phase, the Lund string model [94] is employed. PYTHIA is employed in version 8, using the A14 tune [95] together with the NNPDF23LO PDF set [96]. For this work PYTHIA serves as the default generator to simulate reconstructed dijet events from the QCD background.
- SHERPA [97] is used to generate events with up to three jets in the final state, also simulating hard-scattering and the underlying event. Initial- and final state emissions are matched to the matrix element evaluation using the CKKW method [98]. Partons hadronize according to the cluster model [99]. SHERPA is employed in the CT10 tune and PDF set [100]. For this work SHERPA is used to derive modelling uncertainties.
- POWHEG+PYTHIA is used as another dijet event generator. The hard-scattering and parton shower is simulated with the POWHEG method [101] and is interfaced to PYTHIA to perform the simulation of the underlying event and the hadronization. POWHEG+PYTHIA is employed in the A14 tune [95] together with the NNPDF23LO

---

<sup>1</sup>The pedestal is the baseline of signals in a calorimeter cell, which is affected by both electronic and pile-up noise.

PDF set [96]. For this work POWHEG+PYTHIA is used to derive modelling uncertainties.

- NLOJET++ [102] is used to generate NLO predictions of observables in events with up to three jets in the final state. The calculation is performed on parton level using the dipole-method [103]. NLOJET++ is employed with the CTEQ6.6 PDF set [104]. For this work NLOJET++ is used to generate high-statistics particle-level dijet invariant mass spectra to study the background estimation procedure.
- MADGRAPH+PYTHIA is used to generate signal events within the leptophobic  $Z'$  model presented in Chapter 1.3.4 with two partons in the final state. The LO matrix element of the model is evaluated with MADGRAPH5 which is interfaced to PYTHIA8 to simulate the parton shower, hadronization and the underlying event. The signal samples are generated for mediator masses  $m_R$  between 450 and 1700 GeV and couplings  $g_{SM}$  between 0.05 and 0.40. MADGRAPH+PYTHIA is employed in the A14 tune [95] together with the NNPDF23LO PDF set [96]. For this work MADGRAPH+PYTHIA serves as the default generator to simulate reconstructed dijet events from potential signal models.

# Chapter 4

## The Dijet Trigger-Object Level Analysis (TLA)

The dijet Trigger-Object Level Analysis is a search for low mass, low cross-section dijet resonances exploiting the high statistical power of partially built events that were reconstructed online at the HLT. In the following, the analysis of 2016 data is presented, which is a further development of the analysis on 2015 data [105]. Both analysis iterations are largely influenced by the ATLAS high-mass dijet analysis [106]. The unconventional TLA approach allows for the population of a higher-statistics dijet invariant mass spectrum and is detailed in the following.

### 4.1 The TLA Approach

Traditionally dijet searches have been statistically limited towards low mass regions due to the single jet trigger prescale factors that are needed to keep the bandwidth manageable for trigger, data acquisition and reconstruction systems. The effect of this limitation can be seen in Figure 4.1, where the upper limits on the vector coupling  $g_B$  between quarks and a new  $Z'$  particle are compared among historic collider experiments as a function of the mass of the new particle. Increasing machine luminosities and energies at hadron colliders, has lead to experiments having to employ increasingly higher prescale factors. As a result new generations of experiments such as ATLAS and CMS have stopped improving on limits for lower masses and the best limits from conventional dijet searches still come from SPS and Tevatron experiments.

The dijet TLA circumvents the limitations from the HLT jet trigger prescales by employing a separate data stream called “Datascouting Stream” in which events are saved that were reconstructed online by the HLT. The reconstruction of events that are used for the analysis are independent of the HLT jet trigger prescales. These events follow a dedicated datascouting HLT trigger chain which is seeded by the lowest unprescaled L1 single jet trigger. Thus a dependence on trigger prescales remains, but it is now the L1 prescales that are the limitation. One could say that for the TLA, the role of the trigger is played by

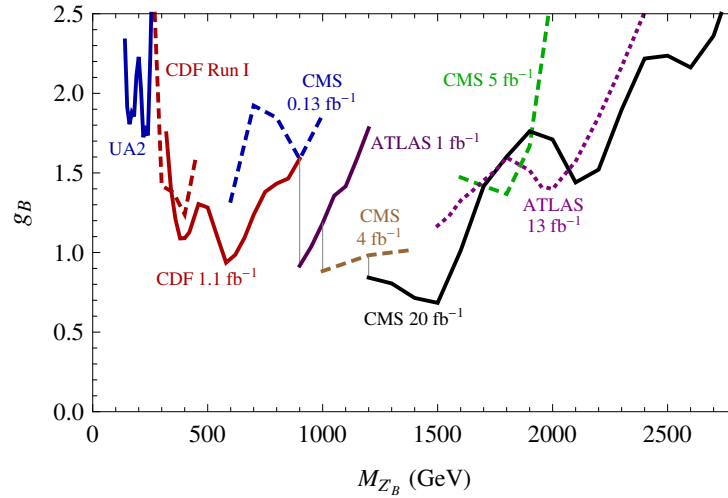


Figure 4.1: A comparison of upper limits on vector coupling  $g_B$  between quarks and a new  $Z'$  particle among historic collider experiments [107].

the L1 trigger and the role of the Tier-0 event reconstruction is played by the HLT. This paradigm shift in the trigger and reconstruction hierarchy is the key to the TLA allowing event recording at a drastically increased rate.

At the same time a large bandwidth is avoided by recording only the information in the event that is indispensable for the search. For the dijet TLA this information is considered to be the calorimeter jet information. Any information from individual calorimeter cells, the muon spectrometer or the inner detector is neglected, reducing the size of these partially built events to a small fraction of the original size. During the 2016 data-taking periods the

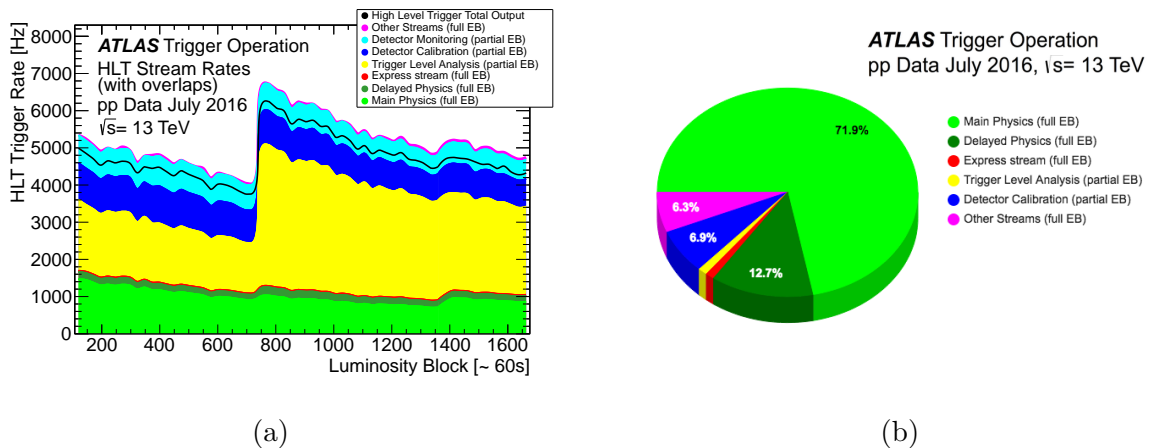


Figure 4.2: Rate (left) and bandwidth (right) of events being recorded to the datascouting stream for the TLA in comparison to the remaining ATLAS data stream [108].

lowest unrescaled single jet triggers were either L1\_J75 or L1\_J100 seeding two separate datascouting trigger chains which trigger the recording of the event header and all HLT jet objects above a  $p_T$  threshold of 20 GeV to the datascouting stream. Associated jet variables such as jet timing, quality variables and jet structure variables are also saved. With sizes of  $\sim 10$  kB/event, event recording rates of  $\sim 3$  kHz are reached which corresponds to  $\sim 43\%$  of the total recording rate of ATLAS while at the same time occupying less than 1% of the total ATLAS bandwidth. This is illustrated in Figure 4.2 in comparison to the other data streams in ATLAS. In contrast, fully reconstructed offline dijet events have sizes of  $\sim 2$  MB/event and are recorded at  $\sim 300$  Hz occupying more than 10% of the total ATLAS bandwidth.

## 4.2 Analysis Strategy

The jet events reconstructed in the datascouting stream serve as the inputs for the TLA analysis. In a first step, they are subjected to a jet quality selection detailed in Appendix A.1 in which jets from non-collision backgrounds (such as cosmic rays or detector noise) are rejected using the available calorimeter jet variables. Whole events can be discarded as well.

A major part of the analysis is the subsequent jet calibration procedure which restores the reconstructed energy of the HLT jets to the jet energy scale (JES).

The TLA jet calibration procedure is based on the well-established procedure for offline jets but is modified when the offline jet calibration procedure is not applicable, i.e. it needs to account for the lack of full detector information in the datascouting stream. Yet it is designed to stay as close as possible to the offline procedure and wherever possible the same calibration factors are applied that were derived for offline jets. This bears an intrinsic source of uncertainty because the dataset used for the derivation of the calibration is only a small fraction of the TLA analysis dataset where the calibration is employed. Apparent insignificant fluctuations in the calibration curves could become sizable within the statistical precision of the analysis dataset. For this reason the TLA imposes stronger demands on the smoothness of the calibration curves than it is foreseen for conventional offline analyses.

The performance of the HLT jet reconstruction, cleaning and calibration is characterized and validated with respect to offline jets in data and in MC.

Once the HLT jets are calibrated, the TLA follows for the most part the analysis approach of a standard resonance search. After an event selection step which optimizes the signal over background ratio, the invariant mass distribution of the two highest  $p_T$  jets is formed. A sliding window fit (SWiFt) provides a data-driven<sup>1</sup> background estimation and is used in conjunction with the BUMPHUNTER-algorithm to identify bump-like excesses from potential low-cross-section signals in the large QCD background of the dijet invariant mass spectrum. Unlike conventional dijet searches, the TLA provides the option to apply

---

<sup>1</sup>Not based on MC, but extrapolated from the employed data itself.

systematic uncertainties in the search phase to account for potential unphysical unsmoothness in the calibration. If no significant excesses are found, Bayesian limits are to be set on leptophobic  $Z'$  signals and on generic Gaussian resonances. In case of an excess, the analysis can be repeated using the full event information which can be recovered from raw events in the delayed stream triggered by L1Topo invariant mass trigger items.

Note that the TLA is a “blinded” analysis, meaning that the full 2016 dataset is not used to derive and validate the basic parameters of the analysis. Only after the analysis procedure has been tested on MC and a small subset of the data, is it executed in a strictly defined order on the full dataset.

### 4.3 Event Selection and Signal Regions

Events are required to have at least two clean jets within  $|\eta| < 2.8$  to avoid the forward region along with the transition region from the hadronic end-cap, where the jet energy resolution decreases. They should have a  $p_T > 85$  GeV because the number of jets above this threshold is independent of the amount of pile-up in the event. The leading jet is furthermore required to have a  $p_T$  greater than the point of 99.5% efficiency<sup>2</sup> of the L1\_J75 or L1\_J100 trigger. The “turn-on” curves for the trigger efficiencies of both triggers are shown in Figure 4.3. This sets the leading jet  $p_T$  cut to 220 GeV for the L1\_J100 trigger and to 185 GeV for the L1\_J75 trigger. A  $y^*$  requirement is additionally applied to suppress the small angle  $\hat{t}$ -channel processes of QCD. A study showed that the signal over background ratio, as determined from  $Z'$  benchmark-signal MC and QCD MC, is maximized for values

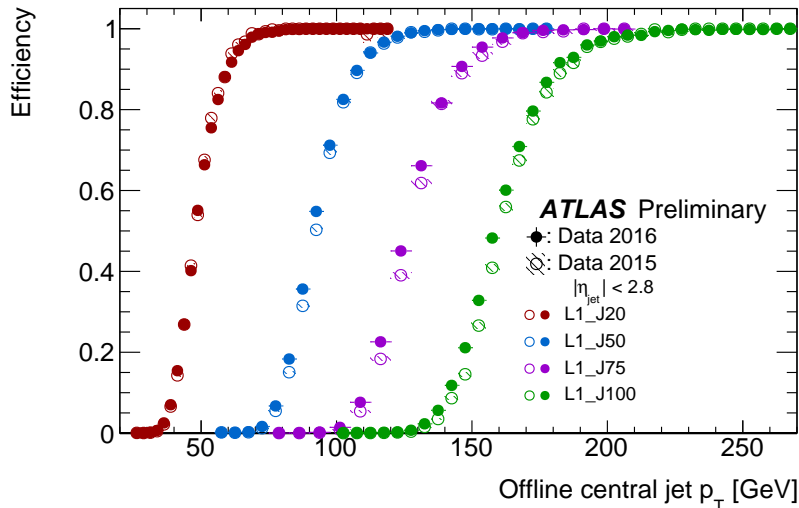


Figure 4.3: Efficiencies of L1 single-jet triggers as a function of leading offline jet  $p_T$  [109].

<sup>2</sup>The trigger efficiency characterizes the fraction of events that are triggered by the respective trigger with respect to the total number of events according to a reference selection. It is limited by the decreased resolution of the trigger system at the kinematic trigger threshold compared to the reference.

between 0.5 and 0.7 for any coupling-mass parametrization [110]. Also the point at which the dijet invariant mass spectrum becomes unbiased of the  $p_{\text{T}}$  selection criteria depends on the  $|y^*|$  requirement. The smaller the difference between the rapidities, the sooner will the mass spectrum become unbiased. For this reason  $|y^*| < 0.6$  is chosen as the nominal requirement and  $|y^*| < 0.3$  is used to extend the unbiased invariant mass spectrum towards lower masses. The two signal regions of the TLA are summarized in Table 4.1.

Trigger	$ y^* $	Leading jet $p_{\text{T}}$	Unbiased $m_{jj}$
L1_J100	$< 0.6$	$> 220 \text{ GeV}$	$> 520 \text{ GeV}$
L1_J75	$< 0.3$	$> 185 \text{ GeV}$	$> 397 \text{ GeV}$

Table 4.1: The two signal regions of the TLA.



# Chapter 5

## TLA Jet Calibration and Performance

### 5.1 Jet Calibration

The reconstructed energy of the jets in the datascouting stream is determined by their calorimeter energy, which does not necessarily reflect their true energy. The calorimeter response correctly reflects the energy of electromagnetic showers, but does not take into account losses in terms of binding energy or escaping particles in hadronic showers. Further energy losses can arise due to uninstrumented detector material, leakage of jet energy falling outside the calorimeters, jet constituents falling outside the jet distance parameters (*out-of-cone radiation*), and furthermore parts of the jet energy may not surpass the noise thresholds during clustering. In order to take all of these effects into account, the originally measured jet energy at the *electromagnetic scale* needs to be calibrated to the *hadronic scale*, or *jet energy scale* (JES). The correction affects the full four-momentum of the jet, scaling jet energy,  $p_T$  and mass. The TLA jet calibration strategy follows the centrally derived<sup>1</sup> jet calibration procedure for offline jets, which is not always possible due to the missing information from the inner detector and muon systems. Therefore parts of the procedure need to be modified for the TLA. The general goal of the process is to correct the reconstructed jet energy with respect to the energy of a particle-level truth jet in MC and to use in-situ methods in well understood topologies to correct for differences in the reconstructed jet energy between data and MC. However several preceding and intermediate steps are similarly crucial. All TLA calibration steps, with differences to the offline procedure being highlighted, are illustrated in Figure 5.1 and discussed in the following.

---

<sup>1</sup>The derivation of the JES calibration and its associated uncertainties is an extensive and sophisticated procedure and is therefore usually derived centrally to be used for all ATLAS analyses together.

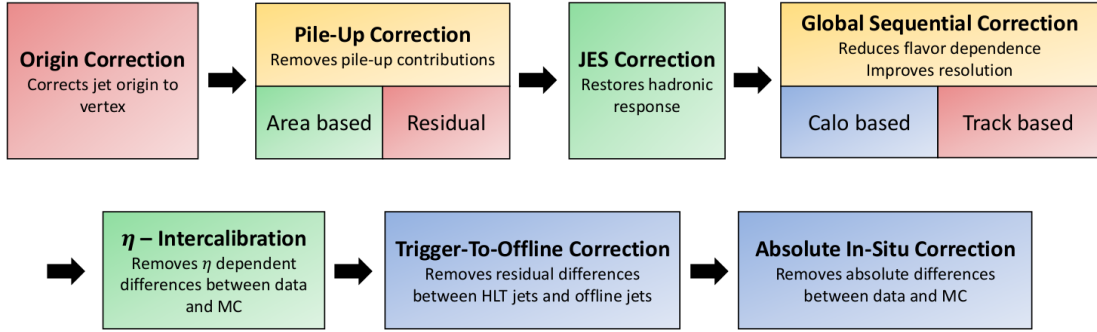


Figure 5.1: Overview of the calibration steps applied on HLT jets within the TLA. Corrections that are identical in the offline scheme are marked in green, whereas those available offline only are marked in red. The blue color indicates dedicated correction steps derived specifically for the TLA.

### 5.1.1 Origin Correction

The origin correction is the first step in the offline calibration procedure. It uses information on the displacement of the primary vertex with respect to the nominal interaction point to derive a correction on the  $\eta$  of the jet. Therefore the jet energy remains unaffected, but the jet angular resolution improves and also the  $p_T$  response improves by a small amount ( $< 1\%$ ) with it. Since primary vertex information is not available in the datascouting stream, this correction step cannot be applied in the TLA.

### 5.1.2 Pile-Up Correction

In the second step each jet is corrected for the contribution to the jet energy from both in-time and out-of-time pile-up interactions. A detailed description of this step can be found in [111, 112]. The correction is parametrized in terms of three pile-up related variables according to

$$p_T^{\text{corr}} = p_T^{\text{reco}} - \rho \times A - \alpha \times (N_{\text{PV}} - 1) - \beta \times \mu, \quad (5.1)$$

where  $\rho$  is the median  $p_T$  density in the event,  $N_{\text{PV}}$  is the number of primary vertices and  $\mu$  is the average number of interactions.  $\rho$  is calculated by the median of the  $p_T$  density of any jets without threshold within  $|\eta| < 2.0$ :

$$\rho = \text{median} \left\{ \frac{p_{T,i}^{\text{jet}}}{A_i^{\text{jet}}} \right\}, \quad (5.2)$$

where  $A_i^{\text{jet}}$  is the area of the jet  $i$  in the  $\eta - \phi$  plane. The product of  $\rho$  and the area  $A$  of the jet is the *jet area based pile-up correction*. A further dependence on pile-up variables remains and is corrected for by the *residual pile-up correction* based on  $N_{\text{PV}}$  and  $\mu$  with their coefficients  $\alpha, \beta$  determined from MC. Since  $N_{\text{PV}}$  is a tracking variable which is undetermined in the datascouting stream and because  $\alpha$  and  $\beta$  have not been derived

independently, the jet area based correction is the only pile-up correction step applied within the TLA.

Uncertainties on the pile-up contributions to the jet energy scale are derived from differences on the slope of jet  $p_T$  as a function of  $\mu$  and  $N_{PV}$  between offline jets and HLT jets.

### 5.1.3 MC-Based Jet Energy Scale Correction

The MC-based jet energy scale correction step corrects the jet energy at EM scale after pile-up removal to the particle-level jet energy scale as a function of the jet energy and  $\eta$ . It is therefore often called MCJES or  $\eta$ -JES. With a detailed description of the procedure given in [113], it is summarized in the following.

In MC simulations, isolated reconstructed jets at EM scale are matched within  $\Delta R < 0.3$  to particle-level jets. In bins of  $\eta_{\text{det}}$  and  $E_{\text{truth}}^{\text{jet}}$  for each matched jet pair the jet response  $\mathcal{R}^{\text{jet}} = E_{\text{EM}}^{\text{jet}}/E_{\text{truth}}^{\text{jet}}$  is computed and the distribution is fitted with a Gaussian to determine the mean response  $\langle \mathcal{R}^{\text{jet}} \rangle$ . Figure 5.2 shows this response as a function of  $\eta_{\text{det}}$  in different  $p_T$  bins. The dependence of  $\langle \mathcal{R}^{\text{jet}} \rangle$  on  $E_{\text{EM}}^{\text{jet}}$  is fitted with a ‘‘Groom’s function’’ in each  $\eta$  bin to ensure a smooth response function:

$$\mathcal{F}_{\text{calib},k} \left( E_{\text{EM}}^{\text{jet}} \right) = \sum_{i=0}^{N_{\text{max}}} a_{i,k} \left( \ln E_{\text{EM}}^{\text{jet}} \right)_k^i, \quad (5.3)$$

where  $a_i$  are free fit parameters and  $N_{\text{max}}$  is an integer between 1 and 6. The measured jet

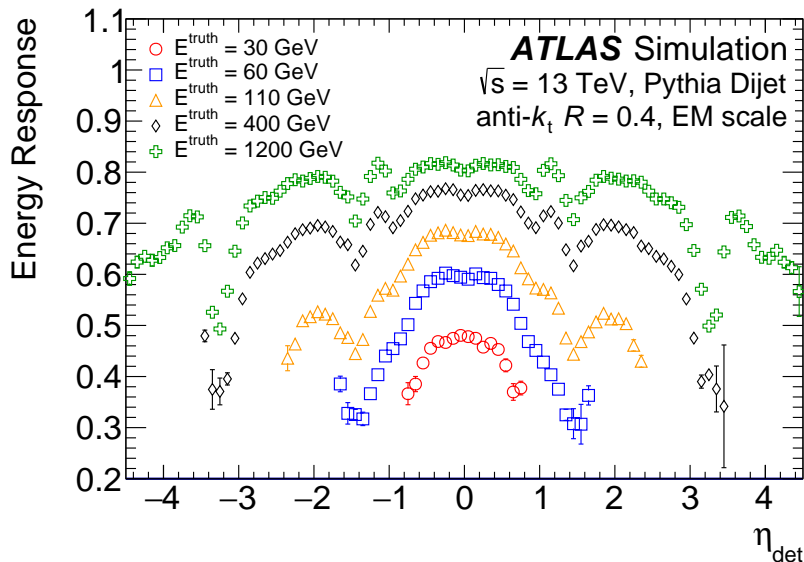


Figure 5.2: Jet response as a function of  $\eta_{\text{det}}$  in different  $p_T$  bins [112].

energy is corrected to the jet energy scale according to

$$E_{\text{EM+JES}}^{\text{jet}} = \frac{E_{\text{EM}}^{\text{jet}}}{\mathcal{F}_{\text{calib}} \left( E_{\text{EM}}^{\text{jet}} \right) \Big|_{\eta_{\text{det}}}} . \quad (5.4)$$

The MCJES calibration constants derived for offline jets can also be used for the TLA. The difference (or *non-closure*) between the energies of HLT jets and offline jets is below 1% for the most part of the TLA signal region. Low  $p_{\text{T}}$  jets in the transition regions perform slightly worse, with agreements below 3% at EM scale and below 4% at EM+JES as it was shown in [114].

### 5.1.4 Global Sequential Correction

The correction factors applied within the calibration do not have to be constrained to be functions of  $p_{\text{T}}$  and  $\eta$  as the only kinematic variables. They can be extended towards further variables characterizing the properties of the detector-level jet. This is achieved in a next calibration step, called Global Sequential Correction (GSC). The GSC is a MC-based method where jets are sequentially calibrated with respect to the particle-level jet energy as a function of several jet property variables. While this correction leaves the average jet response largely unchanged, the jet resolution can be significantly improved. Since the magnitude of some jet property variables differs on average between quark- and gluon-initiated jets, the GSC also has a sizable potential to reduce flavor related response differences and uncertainties. In the GSC for offline jets [115], the following jet property variables are used:

- $f_{\text{Tile}_0}$ , the fraction of the jet energy deposited in the first tile layer
- $f_{\text{EM}_3}$ , the fraction of the jet energy deposited in the third electromagnetic layer
- $N_{\text{Trk}}$ , the number of tracks associated to the jet
- $\text{Width}_{\text{Trk}}$ , the track width, defined as the average  $p_{\text{T}}$ -weighted distance between the tracks  $i$  associated to the jet and the calorimeter jet axis:

$$\text{Width}_{\text{Trk}} = \frac{\sum_i p_{\text{T}}^i \Delta R(i, \text{jet})}{\sum_i p_{\text{T}}^i} \quad (5.5)$$

- $N_{\text{Segments}}$ , the number of muon segments associated to a jet, characterizing the activity in the muon chambers behind the jet

From these variables only  $f_{\text{Tile}_0}$  and  $f_{\text{EM}_3}$  are available in the datascouting stream. Their MC based modelling with respect to data has been checked in a shape comparison using PYTHIA MC. This is demonstrated for different pile-up environments in Figure 5.3 for HLT jets with  $p_{\text{T}}$  around the leading jet  $p_{\text{T}}$  cut, where the highest statistics for the TLA is expected.

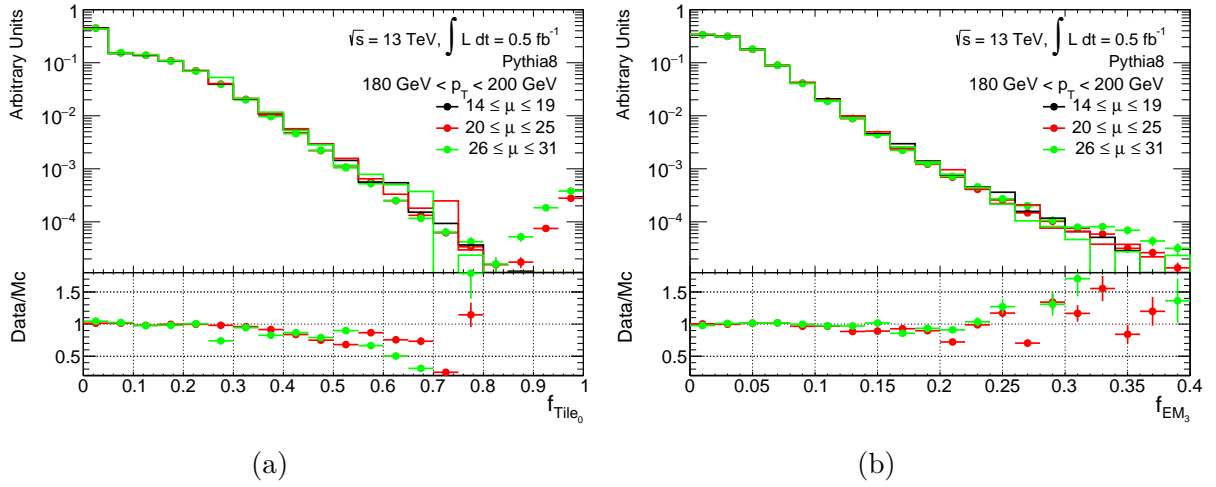


Figure 5.3: Shape comparison of the  $f_{\text{Tile}_0}$  and  $f_{\text{EM}_3}$  variables between data and MC for jets with  $200 \text{ GeV} < p_{\text{T}} < 250 \text{ GeV}$  and different  $\mu$  environments. The dotted datapoints represent data and the lines represent MC.

The agreement is within 5% in the intervals containing more than 99% of the jets for all tested pile-up environments. Further calorimeter-based variables that are available to the TLA have been studied to potentially replace the other offline variables. As a replacement for  $N_{\text{Trk}}$ , the following calorimeter-based variables have been considered:

- $N_{\text{Constituents}}$ , the number of constituents (topological clusters) of the jet
- $N_{90\text{Constituents}}$ , the number of constituents of the jet responsible for 90% of the total jet energy

Again the MC modelling for both variables are compared to data in Figure 5.4.

The agreement for  $N_{90\text{Constituents}}$  is within 5% for 90% of the jets and thus more eligible than  $N_{\text{Constituents}}$  to replace  $N_{\text{Trk}}$ . The modelling of the influence of pile-up on  $N_{90\text{Constituents}}$  is also studied more explicitly and presented in Figure 5.5 showing the arithmetic mean of  $N_{90\text{Constituents}}$  as function of  $\mu$  and  $N_{\text{PV}}$  respectively.

The overall agreement between data and MC is within 2%.  $N_{90\text{Constituents}}$  features significantly distinctive shapes for quark- and gluon initialized jets as it is shown in Figure 5.6, suggesting promising potential to reduce flavor response differences and uncertainties.

A potential replacement for  $\text{Width}_{\text{Trk}}$  is the calorimeter width  $\text{Width}_{\text{Calo}}$ , defined similarly to the track width but using calorimeter constituents instead of tracks. However this variable has not been scheduled in the HLT reconstruction chain during 2016 data-taking and is therefore not available for this iteration of the TLA. Still being potentially applicable for future iterations of the analysis, its modelling is studied as well. Since a restriction on constituents responsible for 90% of the jet energy proved to be superior to the  $N_{\text{Constituents}}$  variable, the  $\text{Width}_{\text{Calo}}$  variable is constrained similarly, defining a dedicated  $\text{Width}_{\text{Calo}90}$  variable. The modelling of both variables are compared in Figure 5.7.

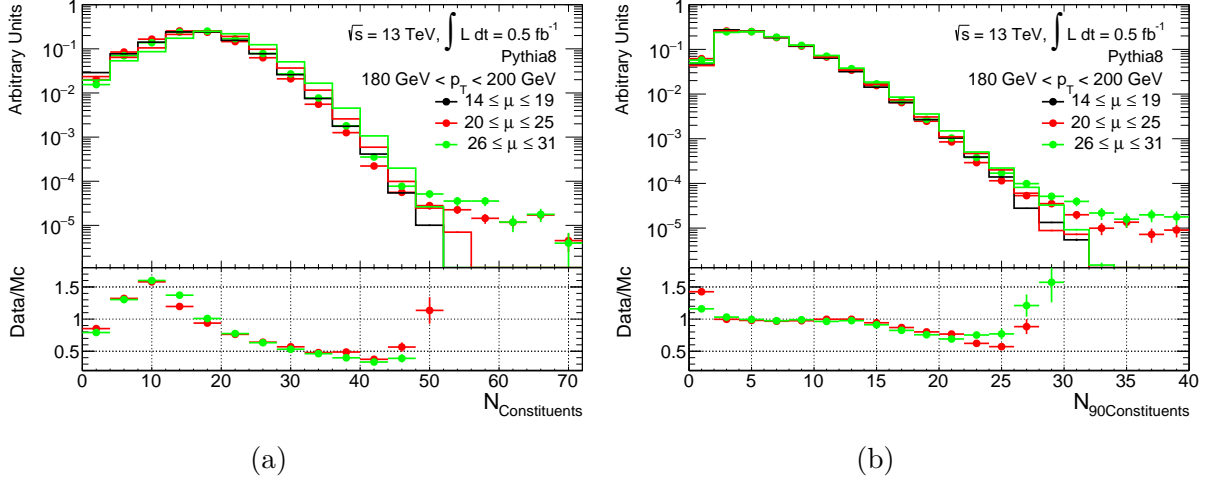


Figure 5.4: Shape comparison of the  $N_{\text{Constituents}}$  and  $N_{90\text{Constituents}}$  variables between data and MC for jets with  $200 \text{ GeV} < p_T < 250 \text{ GeV}$  and different  $\mu$  environments. The dotted datapoints represent data and the lines represent MC.

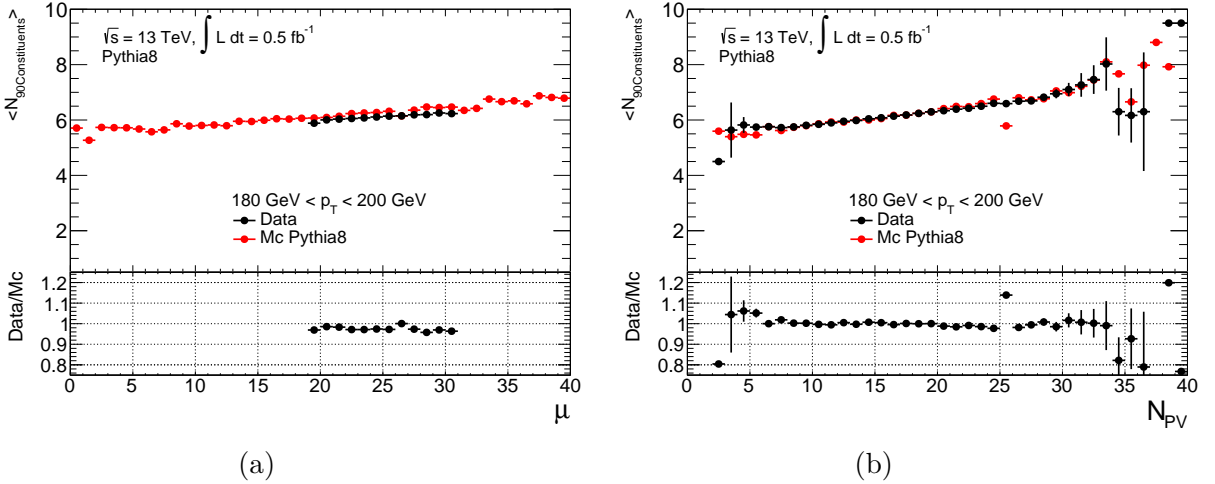


Figure 5.5: Comparison of the arithmetic mean of the  $N_{90\text{Constituents}}$  variable as a function of  $\mu$  and  $N_{PV}$  between data and MC for jets with  $200 \text{ GeV} < p_T < 250 \text{ GeV}$ .

It can be seen that the modelling is generally unimpressive with an agreement ranging between  $< 5\%$  and  $< 40\%$  for  $90\%$  of the jets, and with  $\text{Width}_{\text{Calo}90}$  having no significant advantages over  $\text{Width}_{\text{Calo}}$ . A calorimeter-based variable to replace  $N_{\text{Segments}}$  to account for leakage has not been found. Further shape comparisons close to the subleading jet  $p_T$  cut for all variables to be employed in the TLA in the current iteration,  $f_{\text{Tile}0}$ ,  $f_{\text{EM}3}$  and  $N_{90\text{Constituents}}$ , are given in the Appendix A.2.

Using the aforementioned jet property variables based on HLT jets, the GSC calibration factors are derived with the same technique as described in [115]. The exact procedure is

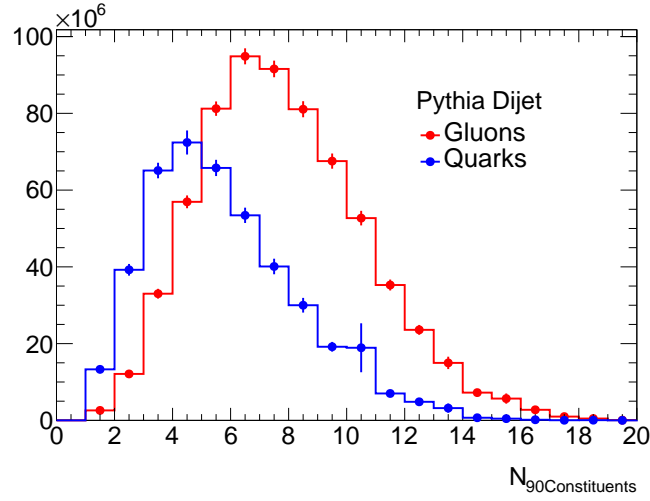


Figure 5.6: A comparison of the  $N_{90\text{Constituents}}$  distribution for quark- and gluon-initiated jets.

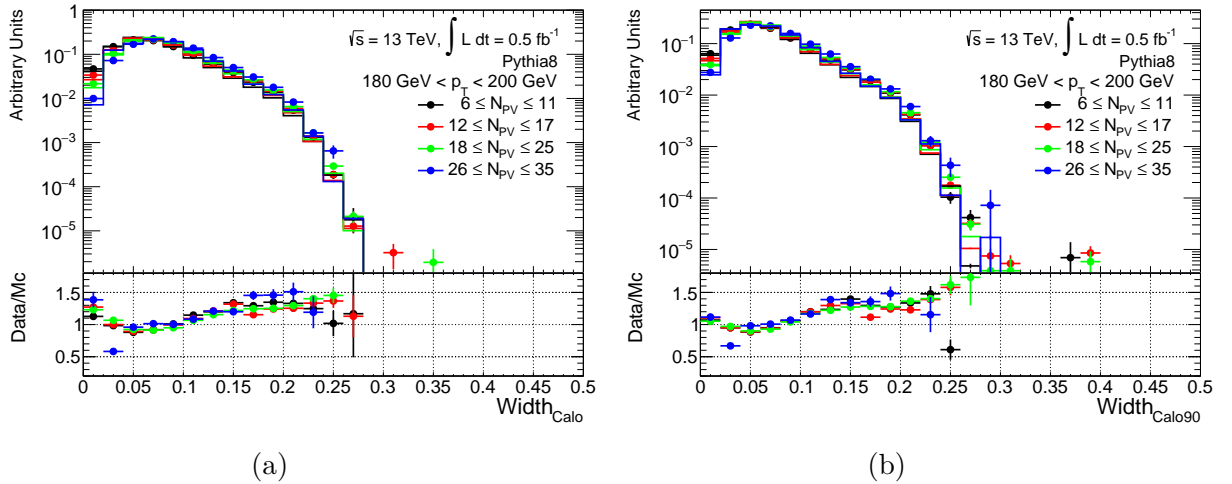


Figure 5.7: Shape comparison of the  $\text{Width}_{\text{Calo}}$  and  $\text{Width}_{\text{Calo90}}$  variables between data and MC for jets with  $200 \text{ GeV} < p_T < 250 \text{ GeV}$  and different  $N_{PV}$  environments. The dotted datapoints represent data and the lines represent MC.

detailed in the following.

The MC samples used are PYTHIA dijet samples with at least two HLT jets within  $|\eta| < 4$  and  $p_T > 7 \text{ GeV}$ . Each HLT jet considered is required to match a truth jet within  $\Delta R < 0.3$ . It also needs to be isolated from the nearest truth jet within  $\Delta R < 1.0$  and from the nearest HLT jet within  $\Delta R < 0.6$ .

The procedure is divided into three sequences. The calibration factors for one of the jet variables are determined in each sequence. In the first sequence the HLT jets are calibrated

to EM+JES and the HLT jet response ( $p_{T,HLT} / p_{T,truth}$ ) distribution is measured in bins of  $p_T$ ,  $\eta$  and the  $f_{Tile_0}$  variable. In each bin the response distribution is fitted with a Gaussian where the fit range is chosen to be dynamical, ranging from the first till last bin with number of entries greater then 5% of the maximum of the Gaussian. The additional requirement that the fit range should cover at least three bins stabilizes the fitting procedure on narrow response curves. For each  $p_T$  and  $\eta$  bin the means of the Gaussian response fits are determined as a function of  $f_{Tile_0}$ . The resulting response distribution is smoothed along  $f_{Tile_0}$  and  $p_T$  in bins of  $\eta$  using a two dimensional Gaussian kernel. The final calibration factors are extracted as a function of  $p_T$ ,  $\eta$  and  $f_{Tile_0}$  as the inverse of this smoothed response distributions. In the second sequence, the HLT jets are calibrated using again the MC-based JES factors, but in addition using the  $f_{Tile_0}$ -dependent calibration factors derived in the first step. Then the  $f_{EM_3}$  calibration factors are derived in the same way as it was done for  $f_{Tile_0}$ . In the third step the  $N_{90Constituents}$  calibration factors are derived based on the HLT jets calibrated using the MC-based JES,  $f_{Tile_0}$  and  $f_{EM_3}$  factors.

Figures 5.8, 5.9, 5.10 (a) show the mean HLT jet response determined from the Gaussian fits as a function of each jet property variable before the GSC has been applied. The dependence on the jet property variables is clearly visible. Due to calorimeter non-compensation, jets have a lower response the more energy they deposit in the deep calorimeter layers  $Tile_0$  and  $EM_3$ . For small deposited energy fractions, the response can differ by up to 10% from unity. Jets containing many particles/constituents tend to be softer, resulting in a lower response as well. The inverse of these response curves gives rise to the sequentially applied calibration curves. In contrast Figures 5.8,5.9,5.10 (b) show the response dependence after the full GSC has been applied, thus demonstrating that the response dependency of the

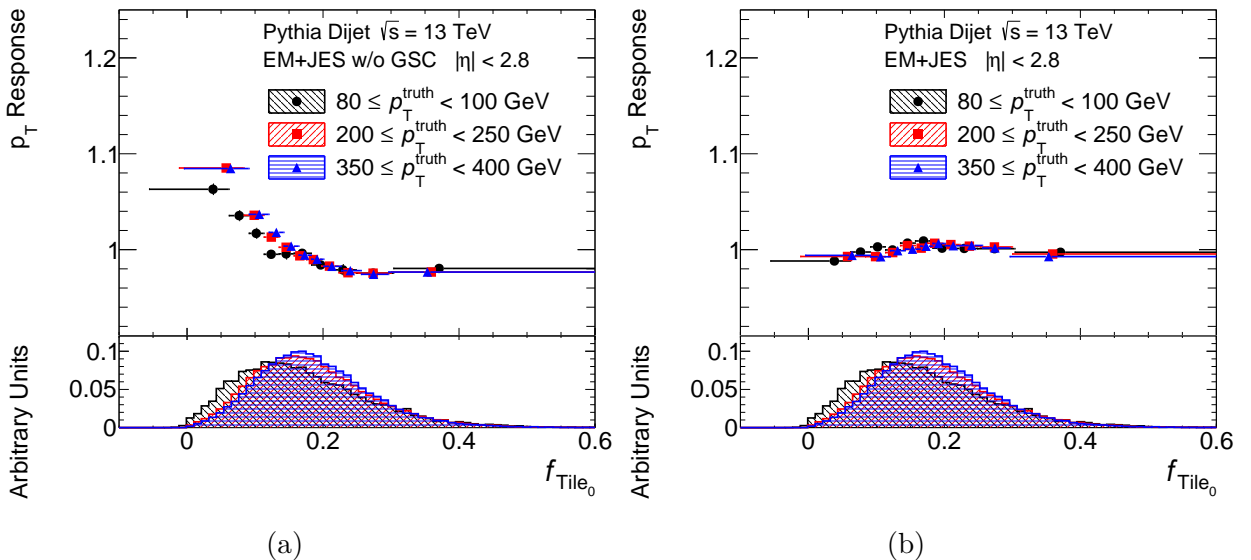


Figure 5.8: The response as a function of  $f_{Tile_0}$  at EM+JES (a) and after the GSC has been applied (b).

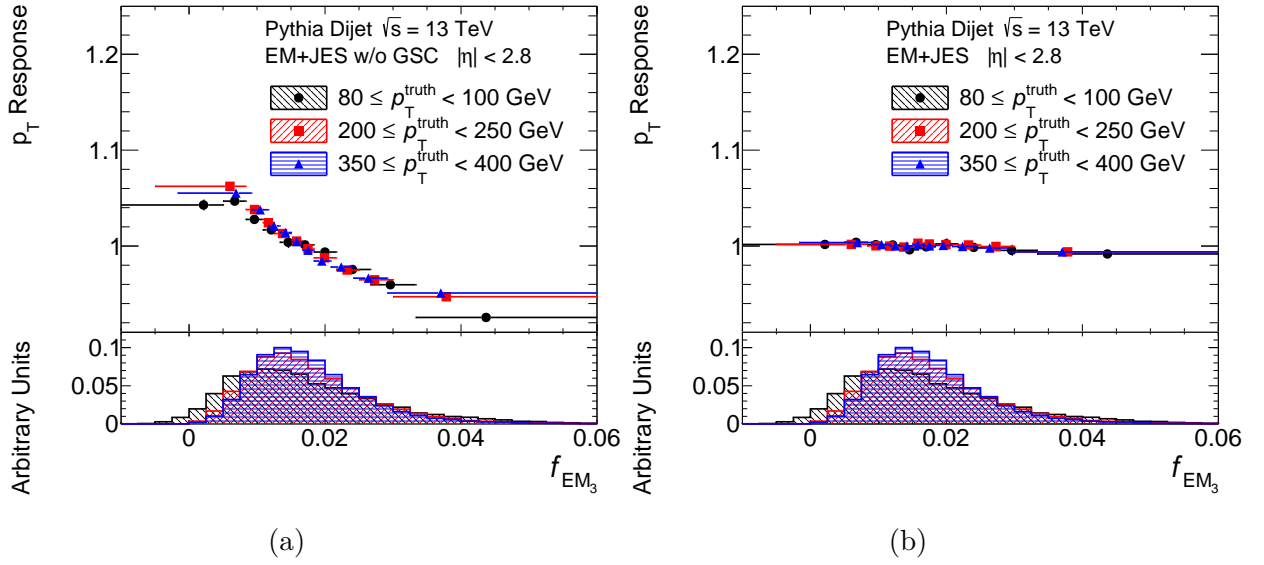


Figure 5.9: The response as a function of  $f_{EM_3}$  at EM+JES (a) and after the GSC has been applied (b).

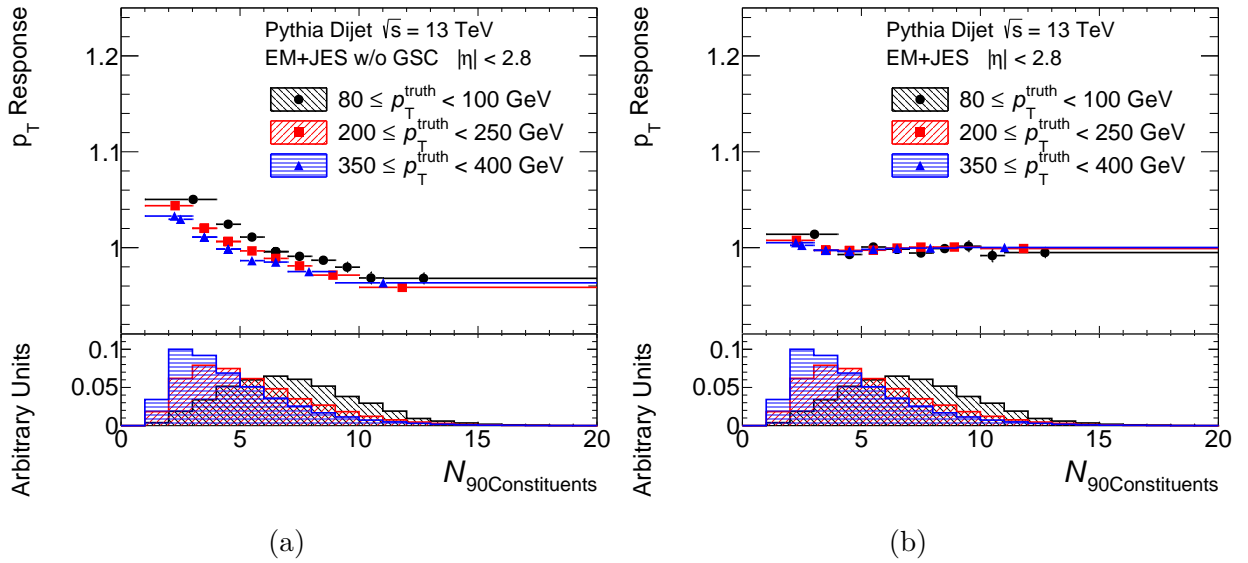


Figure 5.10: The response as a function of  $N_{90Constituents}$  at EM+JES (a) and after the GSC has been applied (b).

jet variables largely vanishes after the application of the GSC. The residual deviation from unity is below 1% for all jet property variables.

A comparison of the HLT jet response as a function of  $p_T$  at EM+JES and after EM+JES+GSC can be found in Figure 5.11. The non-closure before and after the GSC is within 1%. For  $|\eta| < 1.5$  the response is improving, whereas elsewhere it degrades slightly. The improve-

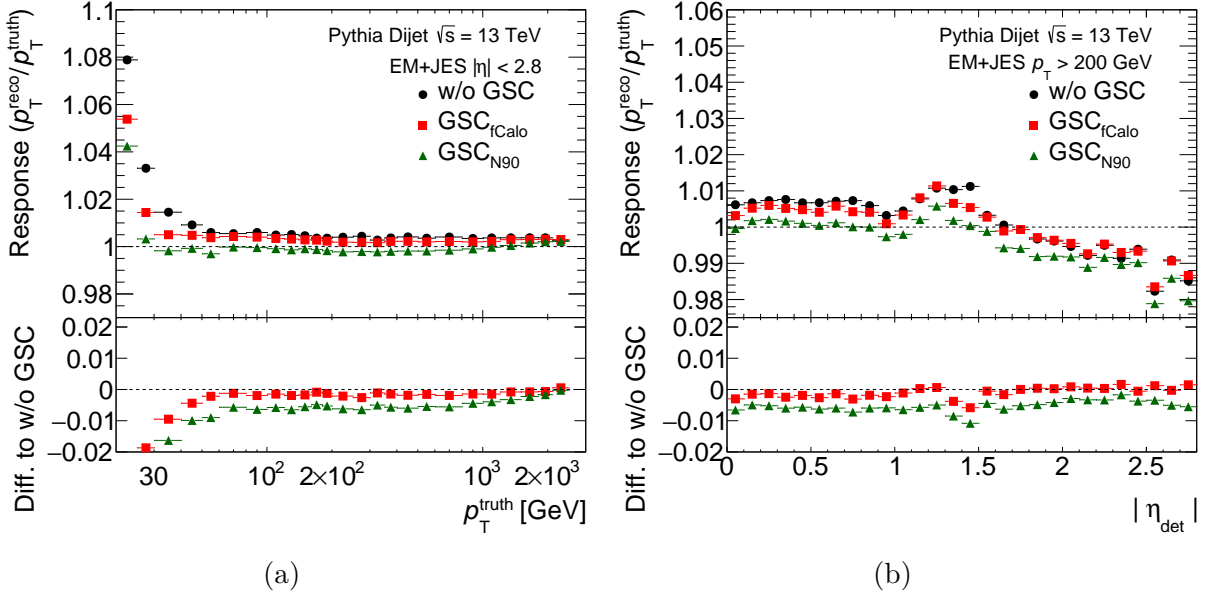


Figure 5.11: The response as a function of  $p_T$  (a) and  $\eta$  (b) at different stages of calibration: EM+JES, after  $f_{T_{\text{ile0}}}+f_{EM3}$  (calo) and after the whole calo based GSC including  $N_{90}$  Constituents.

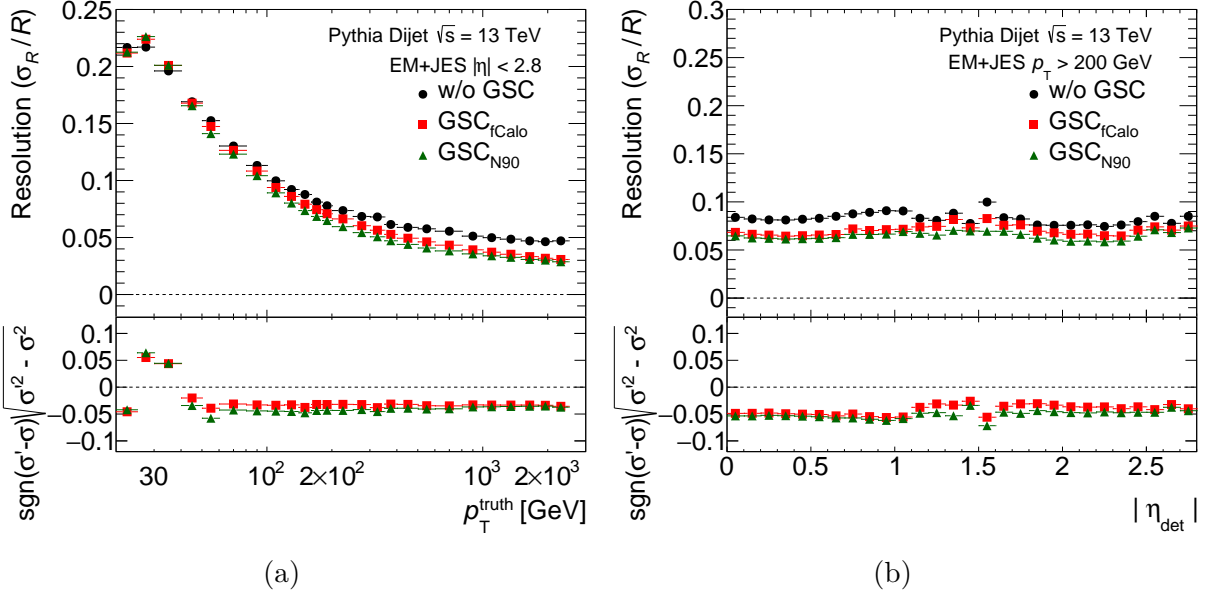


Figure 5.12: The jet energy resolution as a function of  $p_T$  (a) and  $\eta$  (b) at different stages of calibration: EM+JES, after  $f_{T_{\text{ile0}}}+f_{EM3}$  (calo) and after the whole calo based GSC including  $N_{90}$  Constituents.

ment in jet energy resolution due to the GSC is sizable, as demonstrated in Figure 5.12, amounting to around 20% for jets with  $p_T > 200$  GeV. The improvement is relatively constant in  $\eta$ , with a gain due to  $N_{90\text{Constituents}}$  that is especially significant for  $|\eta| > 1.2$  and counterbalances the loss in improvement due to  $f_{\text{Tile0}}$  and  $f_{\text{EM3}}$ . An explanation for this could be that the losses in the poorly instrumented calorimeter transition region are correlated to the number of particles/constituents of the jet.

The performance of a GSC procedure that uses the  $\text{Width}_{\text{Calo}}$  variable in an additional sequence is illustrated in Figure 5.13 and 5.14. It is apparent that due to correlations between  $\text{Width}_{\text{Calo}}$  and  $N_{90\text{Constituents}}$ , a large dependence on  $\text{Width}_{\text{Calo}}$  has already been removed in the preceding GSC sequences and only a slight improvement can be achieved. This is also reflected in 5.14 showing no significant improvement in jet energy resolution for the  $\text{Width}_{\text{Calo}}$  variable.

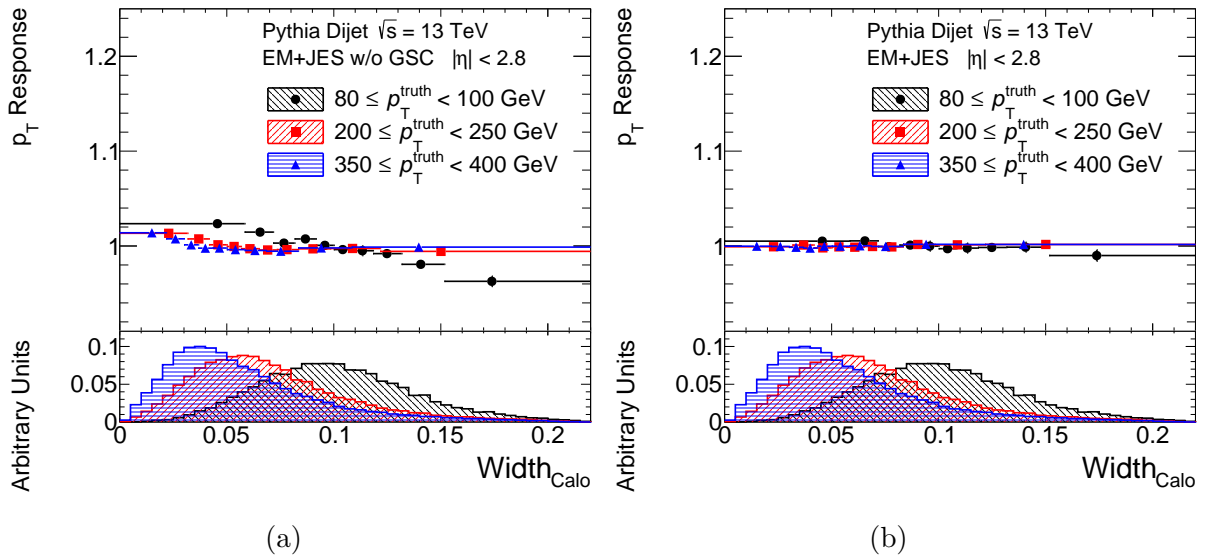


Figure 5.13: The performance of a GSC procedure that uses the  $\text{Width}_{\text{Calo}}$  variable in addition to the other calorimeter variables described in the text. The response as a function of  $\text{Width}_{\text{Calo}}$  is shown before (a) and after (b) an additional calibration sequence based on  $\text{Width}_{\text{Calo}}$ .

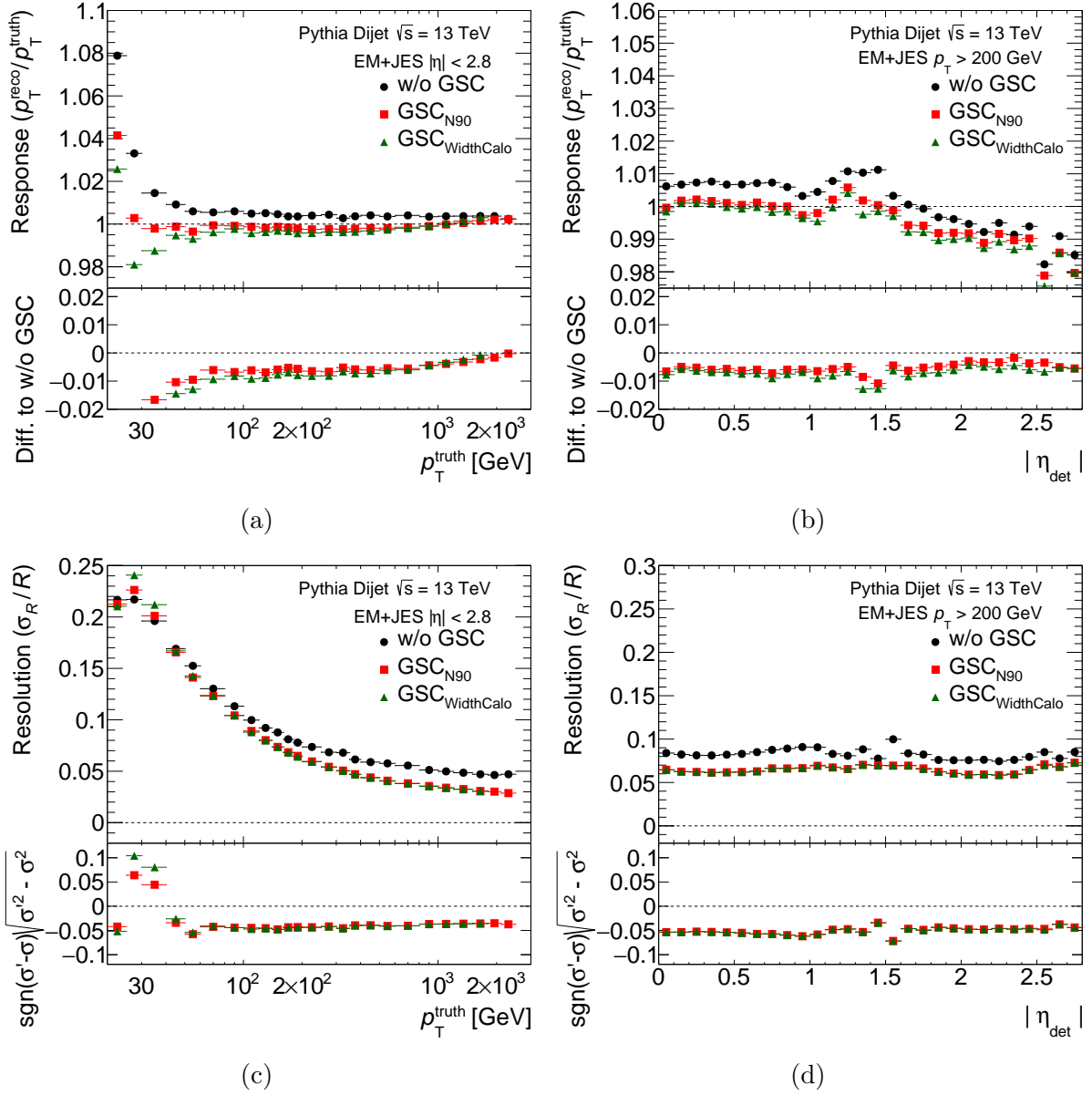


Figure 5.14: The performance of a GSC procedure that uses the  $\text{Width}_{\text{Calo}}$  variable in addition to the other calorimeter variables described in the text. The response is shown as a function of  $p_T$  (a) and  $\eta$  (b) at different stages of calibration: EM+JES, after the whole calo based GSC including  $N_{90\text{Constituents}}$  and after an additional calibration sequence based on  $\text{Width}_{\text{Calo}}$ . The comparison is given for the jet energy resolution in (c) and (d).

### 5.1.5 Relative In-Situ Calibration ( $\eta$ - Intercalibration)

The *in-situ* calibration corrects for differences between reconstructed jets in data and MC using information from events with well-understood reference topologies. The difference between data and MC are not necessarily constant throughout the detector but largely depend on the detector region and are thus  $\eta$  dependent with the most discrepancies arising in the forward region. In the first step of the in-situ calibration, the “ $\eta$  - intercalibration” or “relative in-situ calibration”, these relative differences in  $\eta$  are equalized. This is achieved using a  $p_T$  balance method in dijet events in both data and MC where a forward probe jet is balanced against a central jet serving as a reference object to determine the relative response. The ratio of this relative response in data and MC gives rise to the  $\eta$  - intercalibration factors. The dijet  $p_T$  balance between the probe and reference jet is quantified by their asymmetry:

$$\mathcal{A} = \frac{p_T^{\text{probe}} - p_T^{\text{ref}}}{p_T^{\text{avg}}}, \quad (5.6)$$

where  $p_T^{\text{avg}}$  refers to the average  $p_T$  of the balancing jets. The asymmetry distribution is Gaussian in bins of  $p_T^{\text{avg}}$  making it a more useful parametrization than the plain  $p_T^{\text{probe}}/p_T^{\text{ref}}$ . Using the mean of the asymmetry distribution  $\langle \mathcal{A} \rangle$  in bins of  $p_T^{\text{avg}}$  and  $\eta_{\text{det}}$ , the relative jet response can be expressed as:

$$\mathcal{R} = \left\langle \frac{p_T^{\text{probe}}}{p_T^{\text{ref}}} \right\rangle \approx \frac{2 + \langle \mathcal{A} \rangle}{2 - \langle \mathcal{A} \rangle}. \quad (5.7)$$

The final correction in each  $p_T$  and  $\eta$  bin (i,j) is given by:

$$c_{i,j} = \left( \frac{\mathcal{R}_{\text{MC}}}{\mathcal{R}_{\text{data}}} \right)_{i,j} \quad (5.8)$$

Systematic uncertainties arise from physics and detector mismodellings, as well as requirements on the event topology. They are derived from differences between various MC generators (POWHEG+PYTHIA vs. SHERPA), pile-up contributions and variations of the requirements in the event selection procedure.

The derived  $\eta$  - intercalibration factors for offline analyses are employed within the TLA as well. The agreement between HLT jets and offline jets at  $\eta$  - intercalibration scale is within 4% as it was shown in [114].

### 5.1.6 In-Situ Trigger-to-Offline Correction

After  $\eta$  - intercalibration, the residual differences between HLT jets and offline jets are removed in a dedicated in-situ calibration step via the application of scale factors that bring the HLT jets to the scale of offline jets at this stage of calibration. The calibration factors for this step are derived by matching HLT jets and offline jets within  $\Delta R < 0.4$  and

determining their average ratio in bins of offline jet  $p_T$  and  $\eta_{det}$  from Gaussian fits to the ratio distribution. The resulting distribution of the average ratios is smoothed along  $p_T$  and the final correction factors

$$c_{i,j} = \left\langle \frac{p_T^{\text{offline}}}{p_T^{\text{HLT}}} \right\rangle_{i,j} \quad (5.9)$$

are extracted for each  $p_T$  and  $\eta_{det}$  bin (i,j). After they have been applied to each HLT jet in data, the agreement between HLT jets and offline jets is within 2% [114]. This discrepancy is covered by an associated non-closure uncertainty which is applied in magnitude equal to the scale factors'. Note that the offline events used in the derivation of the scale factors are triggered by prescaled triggers from the statistically limited main physics stream.

### 5.1.7 Absolute In-Situ Calibration

Going into the last stage of the in-situ calibration, the relative responses of central and forward HLT jets have been equalized and also residual differences between the responses of HLT jets and offline jets have been removed up to this point. However absolute ( $\eta$  - independent) discrepancies between the jet response in data and in MC generally still persist. These are removed in the ‘‘absolute in-situ calibration’’ where the  $p_T$  balance of a jet and a well-measurable reference object is determined in data and MC and their ratio is being applied as the correction factor. The method is explained in more detail in [116] and is summarized in the following. Three different topologies are used to derive the correction factors for jets in different  $p_T$  regions. For low  $p_T$  jets with  $20 \text{ GeV} \leq p_T^{\text{jet}} < 500 \text{ GeV}$   $Z$  bosons in  $Z$ +jet events can be used as reference objects. The intermediate range of  $36 \text{ GeV} \leq p_T^{\text{jet}} < 950 \text{ GeV}$  is covered by the analysis of  $\gamma$ +jet with photons as the reference objects. The  $Z/\gamma$ +jet calibration employs two methods to measure the probe jet response. In the *direct balance* method the response is simply

$$\mathcal{R}_{\text{DB}} = \frac{p_T^{\text{probe}}}{p_T^{\text{ref}}} \quad (5.10)$$

with

$$p_T^{\text{ref}} = p_T^{Z/\gamma} \times \cos(\Delta\phi) , \quad (5.11)$$

where the dependence on  $\Delta\phi$  between the probe and reference objects reduces the effect of additional parton radiation. In the alternative *missing projection fraction* (MPF) technique the response is derived from the  $p_T$  balance between the reference object and the full hadronic recoil with

$$\mathcal{R}_{\text{MPF}} = 1 + \frac{\hat{n}_{Z/\gamma} \cdot \vec{E}_T^{\text{miss}}}{E_T^{Z/\gamma}} , \quad (5.12)$$

where  $\vec{E}_T^{\text{miss}}$  is the missing transverse energy reconstructed from calorimeter cells at EM scale and  $\hat{n}_{Z/\gamma}$  is the direction of the reference object. In both methods the average response is derived in bins of  $p_T^{\text{ref}}$  from the mean of a modified Poisson maximum likelihood fit to the response distribution in each bin. To derive calibration factors beyond the ranges of

the  $Z/\gamma$ +jet calibration, the *multijet balance* (MJB) technique is employed, which uses topologies where the probed jet recoils against a system of two or more lower  $p_T$  jets that fall in the range of the  $Z/\gamma$ +jet calibration and are therefore fully calibrated. The MJB response is defined as

$$\mathcal{R}_{\text{MJB}} = \frac{p_T^{\text{probe}}}{p_T^{\text{recoil}}} \quad (5.13)$$

and the average response is obtained in bins of  $p_T^{\text{recoil}}$  similarly to the  $Z/\gamma$ +jet method. This technique can be used sequentially where gradually higher  $p_T$  jets can be calibrated using the MJB result from the previous sequence. With current statistics a range of  $300 \text{ GeV} \leq p_T^{\text{jet}} < 2000 \text{ GeV}$  is covered by the MJB method.

Systematic uncertainties arise from physics and detector mismodellings, as well as requirements on the event topology. They are derived from modelling differences between different MC generators (POWHEG+PYTHIA, PYTHIA, SHERPA, HERWIG++), contributions from pile-up, fake objects and out-of-cone radiation as well as variations of the requirements in the event selection procedure. JES uncertainty components such as the flavor composition and flavor response uncertainty are propagated through each iteration of the MJB.

The data-to-MC response ratios from the  $Z/\gamma$ +jet and MJB calibrations as well as their associated systematic uncertainties are combined across overlapping  $p_T$  regions. Each in-situ method is weighted bin-by-bin according to its response and associated uncertainty, such that the method of greatest precision is favored in the combination. The resulting combined data-to-MC ratio is smoothed along  $p_T$  using a sliding Gaussian kernel in order to reduce statistical fluctuations. The absolute in-situ calibration curve after Gaussian smoothing as it is used by offline analyses is presented in Figure 5.15.

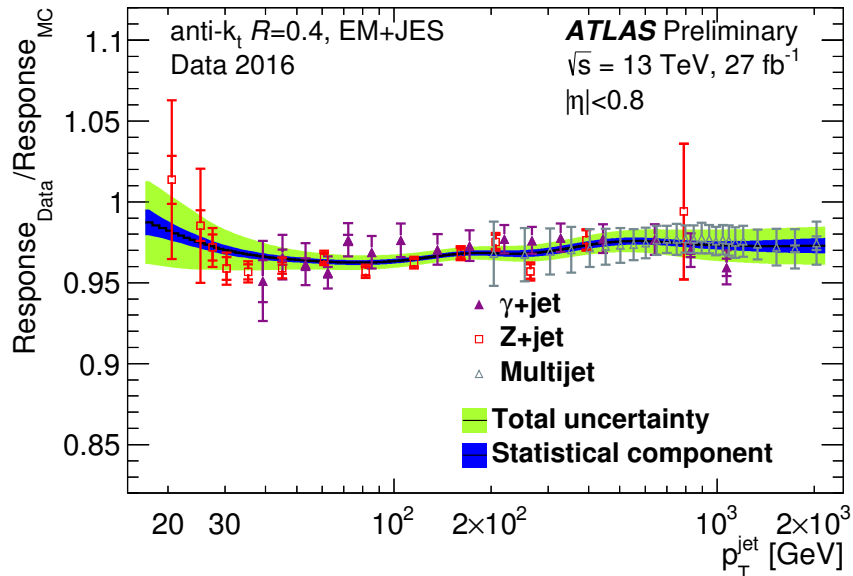


Figure 5.15: The absolute in-situ calibration curve and its associated uncertainties as derived from a Gaussian smoothing kernel operating on the in-situ measurements [117].

This absolute in-situ calibration curve obtained from Gaussian smoothing is not suitable for the TLA as it is demonstrated in a later Chapter 6.8.1. The reason is a statistical downward fluctuation of the  $Z$ +jet data-to-MC response ratio at  $p_T \approx 200$  GeV which bears the danger of inducing an excess in the  $p_T$  and  $m_{jj}$  distributions<sup>2</sup>. In principle, this downward fluctuation is covered by the associated uncertainties which also account for tension between the in-situ methods, however as it is common for dijet searches, the TLA does not apply systematic uncertainties corresponding to correlated sources (such as uncertainties on the absolute scale) in the search phase, since variations in these sources are irrelevant to the deviations identified by a data-driven background fit. The influence of uncorrelated sources of uncertainty (such as those connected to the smoothness of the calibration curve) can in many cases be assumed to be negligible, but not necessarily in the case of the high statistical power of the TLA. To keep these at a minimum an alternative in-situ calibration is derived for the TLA.

For an alternative absolute in-situ calibration to be suitable for the TLA without the danger of inducing excesses in the  $p_T$  and  $m_{jj}$  spectra it is required to be more smooth over small  $p_T$  ranges. This requirement is motivated by the linearity of the detector response  $R_d$  and is realized by using a polynomial fit  $f$  to the datapoints of the in-situ measurements as alternative calibration curve. The polynomial is chosen based on data/function com-

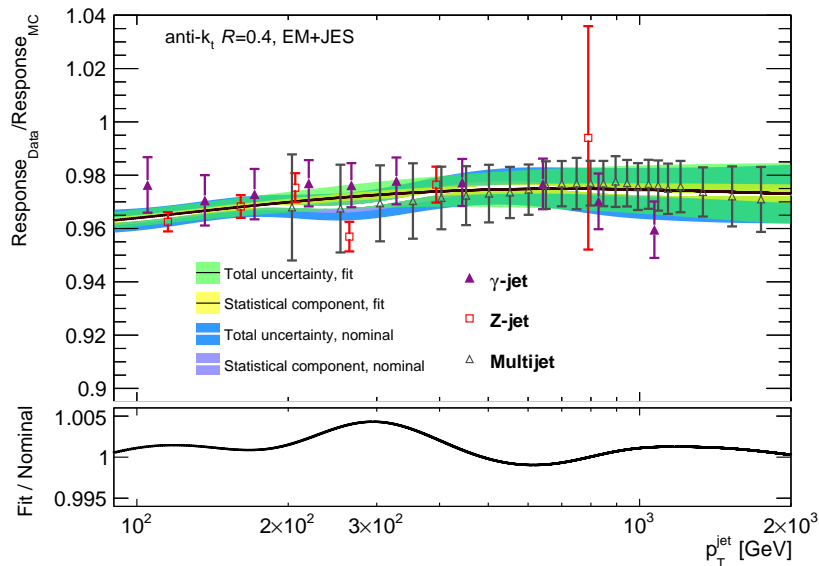


Figure 5.16: The alternative absolute in-situ calibration curve and its associated uncertainties as derived from a polynomial fit to the in-situ measurements. The bottom panel shows the ratio to the absolute in-situ curve from a Gaussian smoothing kernel operating on the in-situ measurements.

<sup>2</sup>The mechanism by which a dip in a calibration curve can cause an excess in a  $p_T$  distribution is that uncalibrated jets falling in the  $p_T$  range of the dip, will undergo a smaller  $p_T$  shift than their neighbors and thus coincide with them to the same  $p_T$  after calibration which results in an excess.

patibility while taking into account the correlations of the uncertainties. The agreement is quantified by  $\chi^2 = (f - R_d)C^{-1}(f - R_d)^T$ , where  $C$  is the correlation matrix containing the uncertainties and their correlations. Candidate fit functions are compared to the nominal in-situ calibration curve and its associated uncertainties. The fit function of choice is the one with the highest agreement to the nominal calibration curve across large  $p_T$  intervals and a similar magnitude of associated uncertainties:

$$f(p_T) = a_{n1} \cdot (\log p_T)^{-1} + a_0 + a_1 \cdot \log p_T + a_2 \cdot (\log p_T)^2 + a_3 \cdot (\log p_T)^3 + a_4 \cdot (\log p_T)^4 \quad (5.14)$$

The alternative absolute in-situ calibration curve and its associated uncertainties as derived from the polynomial fit are shown in Figure 5.16. As intended, the ratio to the nominal is largest for the  $p_T$  range around 200 GeV.

### 5.1.8 In-Situ Validation

The full calibration chain was validated using a similar  $\gamma$ +jet and a Z+jet balance technique used for the absolute in-situ calibration [118], with the difference that the ratio between the  $p_T$  response of fully calibrated offline jets and HLT jets is used as the figure of merit. In this data-driven method, the jet energy is probed in events with one jet recoiling against a well-calibrated  $\gamma$ /Z-boson as a reference object.

The balance, as the variable of interest, is constructed as  $\mathcal{B} = p_T^{\text{jet}}/p_T^{\text{ref}}$ . In an ideal case, where the reference object's four-momentum could be measured perfectly and the jet contains all (and only) the particles originating from the recoil against the  $\gamma$ /Z-boson, the jet response could be measured using  $p_T^{\gamma/Z}$  as the reference  $p_T$ . However, the measurement is affected by additional parton radiation, out-of-cone radiation, pile-up, the underlying event and the uncertainty in the photon energy. The effects of additional parton radiation can be partially reduced by using

$$p_T^{\text{ref}} = p_T^{\gamma/Z} \times |\cos \Delta\phi(\text{jet}, \gamma/Z)|,$$

as the reference  $p_T$ , where  $\phi(\text{jet}, \gamma/Z)$  is the azimuthal angle between the  $\gamma$ /Z-boson and the jet. The contributions are minimized further by applying strict event and object selection criteria.

For the  $\gamma$ +jet balance technique events are selected using trigger elements ranging from HLT\_g10 to HLT\_g140. Photons are selected using "tight" identification criteria [119] and they need to be isolated. The photon transverse momentum must be greater than 25 GeV and its  $|\eta|$  must be smaller than 1.37. In the case of photon conversion [120] in the tracker the ratio of photon cluster transverse energy and associated track transverse momentum  $E_T^{\gamma, \text{cluster}}/p_T^{\text{tracks}}$  is required to be between 0 and 2 (0.5 and 1.5) for single-track conversion (double track conversion).

For the Z+jet balance method events are selected using the HLT\_2mu10, HLT\_2mu14 and HLT\_2e15 trigger elements. The Z-boson is reconstructed from both, the  $Z \rightarrow e^+e^-$  and  $Z \rightarrow \mu^+\mu^-$  decay channels. Thus, exactly two leptons of same flavor and opposite charge

with a combined invariant mass in the range 80 – 116 GeV are required. Electrons (muons) are selected using "loose" ("very loose") identification criteria [119, 121]. Both leptons should be isolated and have a transverse momentum greater than 20 GeV. Further, electrons (muons) are required to be within  $|\eta| < 2.47$  (2.4) and electrons should not be in the calorimeter transition region.

Offline jets are subjected to a jet quality selection and fully calibrated according to the calibration procedure for offline jets with the exception that the alternative in-situ calibration curve is applied to them as well. They are selected requiring a transverse momentum of at least 20 GeV and  $|\eta| < 0.8$ . Further any jet with  $p_T > 50$  GeV and  $|\eta| < 2.4$  is required to have a  $JVF^3 < 0.64$ . As topological selection, the subleading jet must have a  $p_T < \max(15 \text{ GeV}, 0.1 \times p_T^{\text{ref}})$  and the azimuthal angle between each jet and the photon must be greater than 2.9 rad. Furthermore the jets must be isolated from any leptons. The leading offline jet passing this selection is used to construct the balance. To probe the corresponding balance for the HLT jets, the HLT jets are matched to the selected leading offline jet requiring  $\Delta R < 0.4$  between the HLT jet and the offline jet. The HLT jets were fully calibrated according to the full TLA calibration chain and subjected to a jet quality

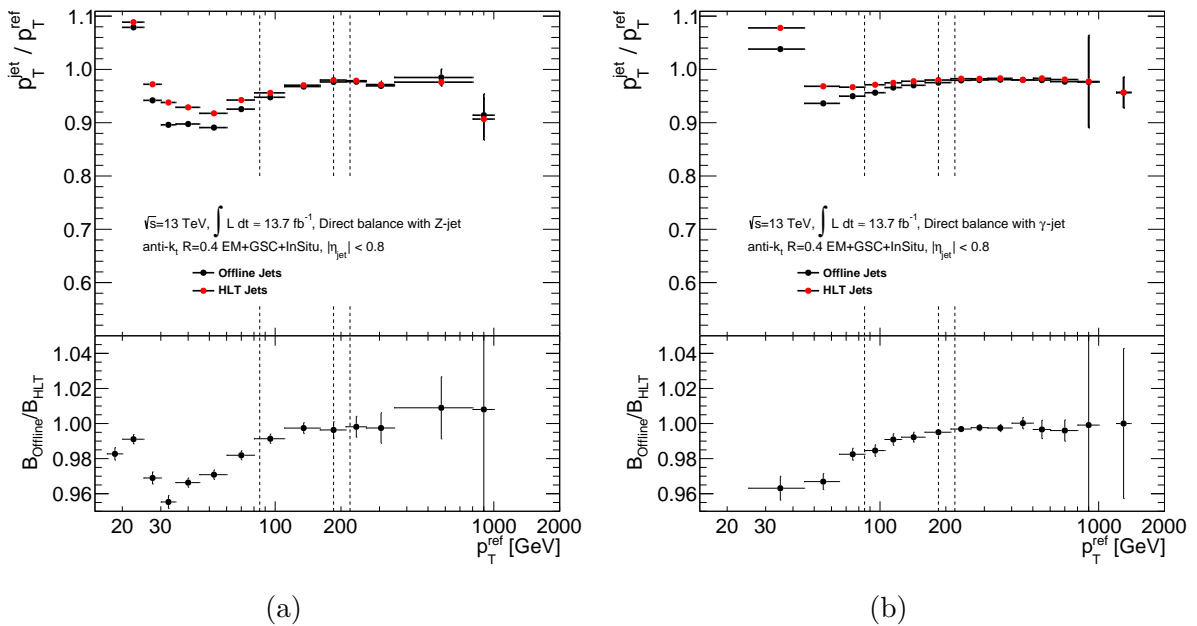


Figure 5.17: Z-jet (left) and  $\gamma$ -jet (right) direct balance validation for the dedicated calibration (EM+JES+GSC and in-situ calibration) sequence of HLT jets compared to offline jets. The dashed vertical lines indicate from left to right the subleading jet  $p_T$  threshold, the leading jet  $p_T$  threshold in the J75 signal region and the leading jet  $p_T$  threshold in the J100 signal region used in the TLA.

<sup>3</sup>The ratio of the  $p_T$  sum of tracks from the primary vertex associated to the jet and the total  $p_T$  sum of tracks associated to the jet.

selection.

Figure 5.17 shows the mean balance as taken from Gaussian fits to the balance distribution for offline jets as well as HLT jets and their ratio as a function of the photon or Z-boson  $p_T$  based on a fraction of the 2016 dataset. Throughout the TLA signal region (above 85 GeV) they agree within 1.5%. Above the leading jet  $p_T$  threshold the agreement is within 0.5%. A slight bias is observed indicating a higher response for HLT jets compared to offline jets. This bias is  $p_T$  dependent and grows for smaller  $p_T$ . An explanation is, that events were selected requiring photon, di-electron or di-muon triggers: HLT jets will not be reconstructed if no additional L1 jet trigger fired. This biases the method to include more HLT jets with a larger response because for those it is more likely that an additional L1 jet trigger fired. Due to the steeply falling jet  $p_T$  spectrum this can only be partially compensated by jets with a lower  $p_T$  response.

## 5.2 Jet Energy Scale Uncertainties

The TLA uses the jet energy scale uncertainties which are derived in the offline jet calibration procedure as well as further additions and re-derivations of individual components to account for the deficiencies of the TLA. Additional uncertainties arise for pile-up contributions and the non-closure uncertainty between offline and HLT jets derived from the scale factors. Further uncertainties that need to be re-derived are the flavor composition uncertainties based on the signal region selection of the TLA and flavor response uncertainties based on the calorimeter-based GSC. The complete set of JES uncertainties can be applied to signal MC templates and the background estimate to derive upper limits on BSM physics models within the TLA limit setting procedure. Unlike conventional dijet analyses [4], the TLA also provides for the option to apply systematic uncertainties on the JES during the search phase.

### 5.2.1 Flavor Uncertainties

In order to reduce flavor uncertainties - the most dominant contributions to the JES uncertainty in the 2015 iteration of the TLA - both the flavor composition and flavor response uncertainty are re-derived. The flavor composition uncertainty is decreased by a dedicated determination of the gluon fractions  $f_g$  and gluon fraction uncertainties  $\Delta f_g$  of both QCD background jets and signal jets using different MC generators. The quark fractions are given by  $f_q = 1 - f_g$ . The uncertainty also decreases by a reduction of the response difference  $R_q - R_g$  between quark- and gluon-initiated jets which is achieved with the introduction of the calorimeter-based GSC. The uncertainty in the flavor response is dominated by the uncertainty in the gluon response  $\Delta R_g$ , which is re-derived using different MC generators as well. The flavor uncertainty is given by

$$\Delta R_{\text{flav}} = \Delta f_g (R_q - R_g) + f_g \Delta R_g , \quad (5.15)$$

where the first and second term represent the flavor composition and flavor response uncertainty [116].

The gluon fractions  $f_g^{\text{QCD}}$  and the gluon fraction uncertainty  $\Delta f_g^{\text{QCD}}$  of the QCD background were derived based on three dijet MC generators, PYTHIA, POWHEG+PYTHIA and SHERPA, where PYTHIA is taken as the nominal and the latter two are used to determine the uncertainty.

In every event each HLT jet is matched to a truth jet requiring  $\Delta R < 0.4$ . If more than one truth jet fulfills this condition, the one with the highest energy is taken. For each matching truth jet the original parton which initiated the jet is identified such that the gluon fraction ( $f_g = N_{\text{gluons}}/N_{\text{partons}}$ ) is determined in bins of  $p_T$  and  $\eta$ . The resulting  $f_g^{\text{QCD}}$  is shown in Figure 5.18(a). To determine the uncertainty for  $f_g^{\text{QCD}}$  this procedure is repeated for POWHEG+PYTHIA and SHERPA. The systematic uncertainty is taken as the maximum difference among all generators in each bin. In bins with low statistics,  $f_g^{\text{QCD}}$  is set to 0.5 with an associated uncertainty of 100%. The resulting uncertainty  $\Delta f_g^{\text{QCD}}$  is presented in Figure 5.18(b).

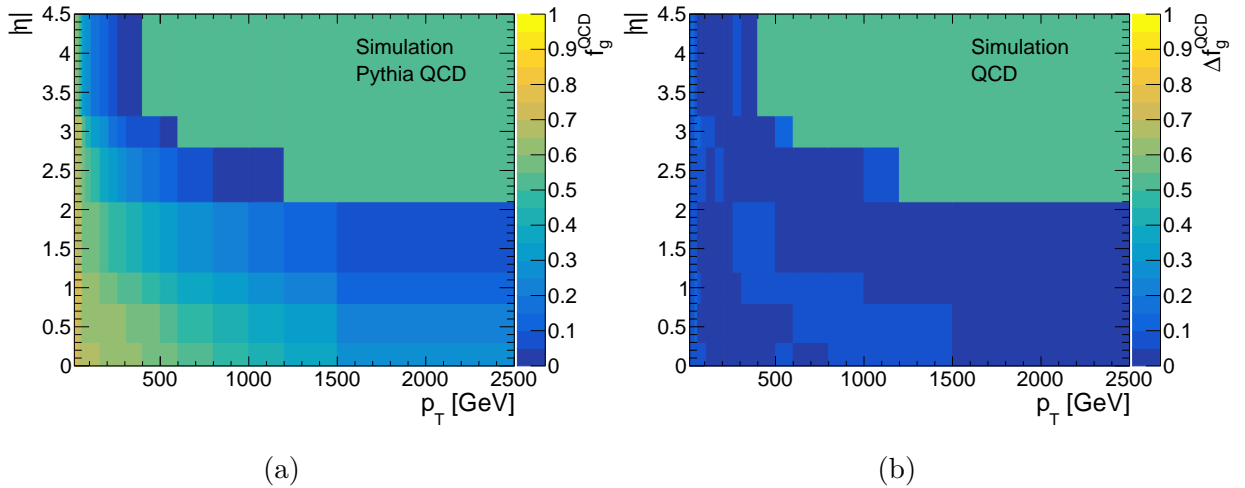


Figure 5.18: The gluon fraction of QCD background jets as determined from PYTHIA MC (left) and its associated uncertainty as derived from differences between different generators (right) as functions of  $p_T$  and  $\eta$ .

Figure 5.19(a) shows a comparison of the fractional JES uncertainty for HLT jets with unknown flavor composition as a function of  $p_T$ , as it was done for the 2015 iteration of the TLA, and the same using the flavor composition of a PYTHIA sample as determined by the previously described method. For example at  $p_T = 200$  GeV the flavor-related uncertainty is reduced by 55% and the total HLT JES uncertainty is reduced by 45%.

The gluon fractions for signal jets are determined from MC samples of a leptophobic  $Z'$  simplified model. Since no significant dependence of the gluon fractions on the coupling was observed, the gluon fractions are averaged over the different couplings separately for each mass point.

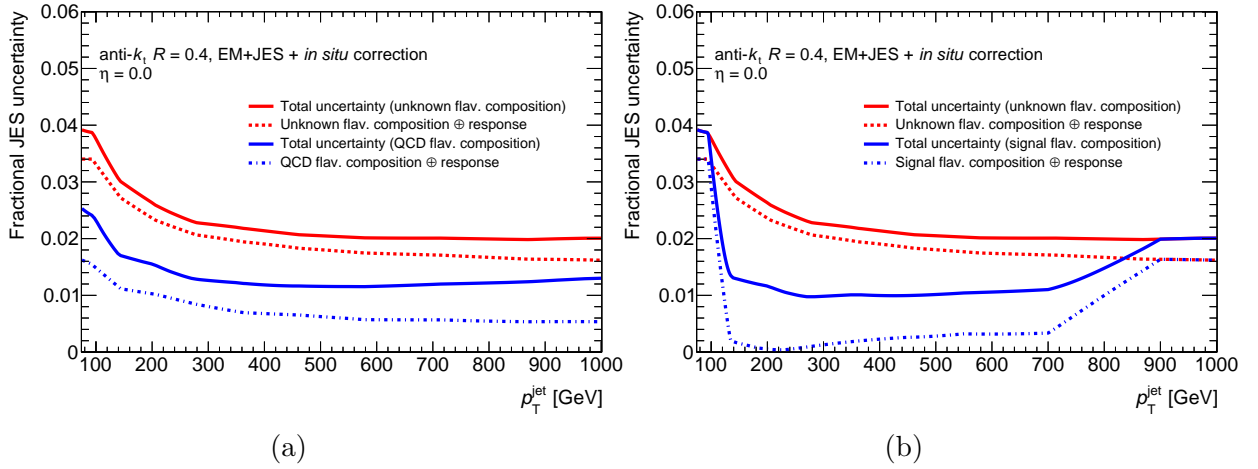


Figure 5.19: The fractional JES uncertainty and its flavor components for HLT jets as a function of  $p_T$  with and without a dedicated gluon fraction determination. The gluon fractions were determined from a Pythia QCD dijet sample (left) and a  $Z'$  signal MC with  $m_{Z'} = 550$  GeV.

The resulting gluon fractions are determined by the procedure described above. Due to the lack of different generators, the uncertainties were derived using the relative uncertainties from  $f_g^{\text{QCD}}$ . This is justified because the differences between the generators due to the matrix elements and PDFs are minimal and the main sources of differences result from showering modelling [122]. The same showering uncertainties should also be applicable to signal jets. The resulting gluon fractions and their uncertainties for two example mass parametrizations  $m_{Z'} = 550$  GeV and  $m_{Z'} = 1700$  GeV are given in Figures 5.20 and 5.21.

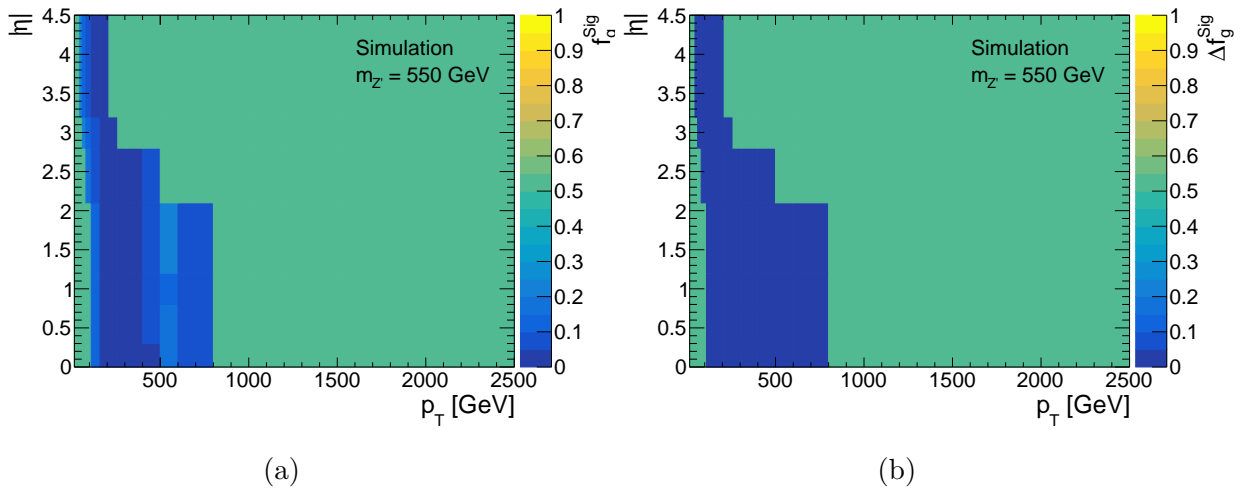


Figure 5.20: The gluon fraction of signal jets as determined from a MC  $Z'$  model with  $m_{Z'} = 550$  GeV (left) and its uncertainty (right).

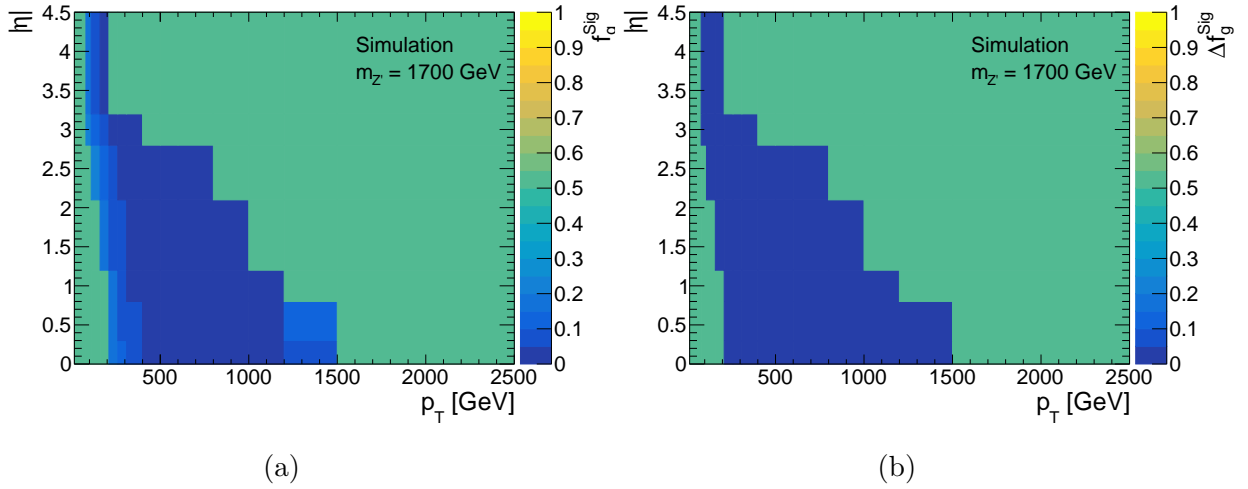


Figure 5.21: The gluon fraction of signal jets as determined from a  $Z'$  model with  $m_{Z'} = 1700$  GeV (left) and its uncertainty (right).

Figure 5.19(b) shows the  $p_T$ -dependent fractional JES uncertainty for HLT jets as determined from the  $Z'$  model with  $m_{Z'} = 550$  GeV compared to the scenario with unknown flavor composition. Since the signal dijets at  $p_T \approx m_{Z'}/2$  are almost exclusively composed of quark-initiated jets, the flavor-related uncertainty becomes almost negligible and the total uncertainty is reduced by up to 54%.

The flavor uncertainty can be further reduced by a determination of the difference of the response between quark- and gluon-initiated jets and the difference on the modelling of the gluon response  $\Delta R_g$  between different MC generators.

The response  $\mathcal{R} = \langle p_T^{\text{HLT}}/p_T^{\text{truth}} \rangle$  at GSC scale is determined in bins of  $p_T$  and  $\eta$  from the mean of Gaussian fits to the response distribution in each bin, where each HLT jet is required to match a truth jet stemming from a gluon or a quark respectively. For high  $p_T$  bins with insufficient statistics, the value of the highest  $p_T$  bin with sufficient statistics is “frozen”. The resulting response maps derived from PYTHIA MC for both cases are given in Figure 5.22.

To derive the uncertainty in the modelling of gluon-initiated jets, the gluon response is also determined from SHERPA (Figure 5.23(a)) and the calculated gluon response difference between PYTHIA and SHERPA is presented in Figure 5.23(b).

To further estimate the propagation of this gluon response difference through the multijet balance calibration, the ratio of the gluon response difference and the multijet balance propagation is assumed to be similar for offline jets and HLT jets. Thus the maximum discrepancy by which the gluon response difference of HLT jets exceeds the one for offline jets is multiplied by the offline multijet balance propagation to obtain a conservative estimate for the TLA multijet balance propagation. To obtain the highest exceeding value, the ratio of the gluon response for HLT jets and offline jets is taken as shown in Figure 5.24(a). The highest discrepancy in regions with sufficient statistics is found to be 1.3. The offline multijet balance propagation is multiplied by this number to obtain an estimate for the HLT

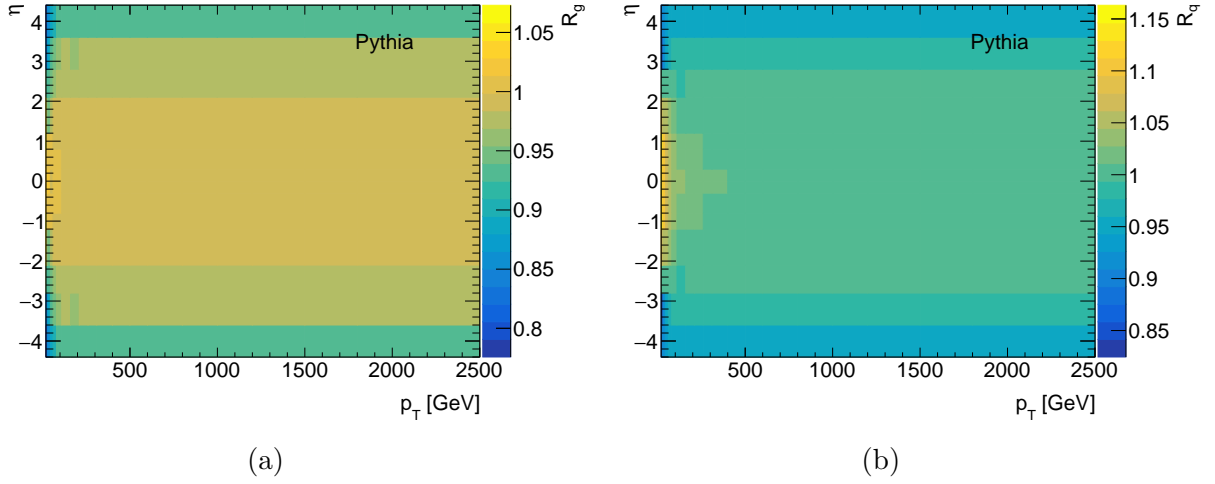


Figure 5.22: Average response of gluon-initiated jets (a) and quark-initiated jets (b) as a function of  $p_T$  and  $\eta$  as determined from PYTHIA MC.

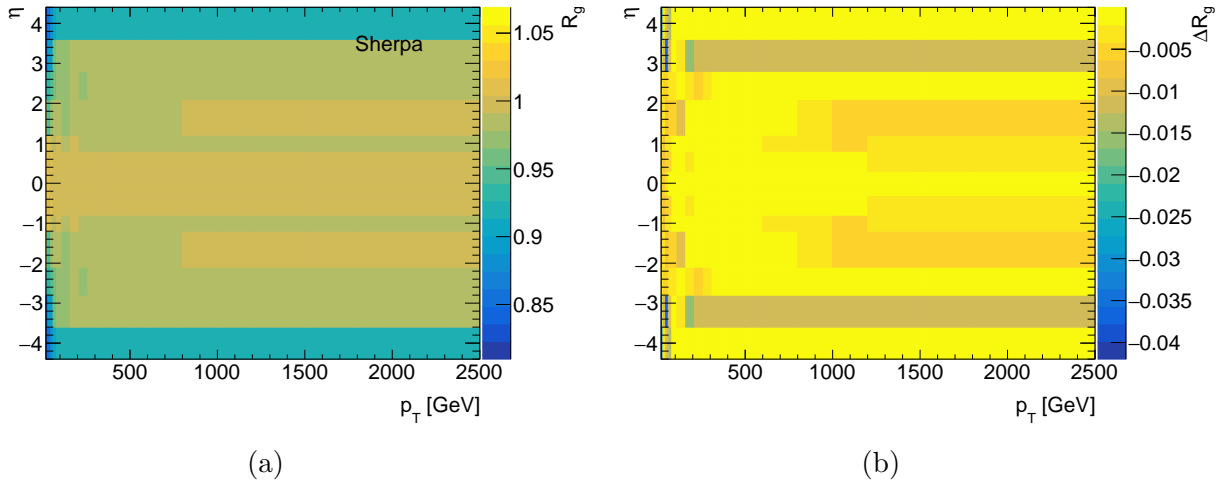


Figure 5.23: Average response of gluon-initiated jets as a function of  $p_T$  and  $\eta$  as determined from SHERPA MC and the difference between the gluon responses determined in PYTHIA and SHERPA (b).

multijet balance propagation which is shown in Figure 5.24(b) and compared to the offline multijet balance propagation and a scenario without GSC applied. It can be seen that for a large fraction of bins the determined gluon response difference between the generators is smaller for HLT jets than for offline jets. This is for a large part also a result of progress in modelling of the generators since the latest derivation of the gluon responses for offline jets.

Figure 5.25 compares the fractional JES uncertainty as a function of  $p_T$  for HLT jets with and without the re-derivation of the flavor uncertainties due to the calorimeter-based

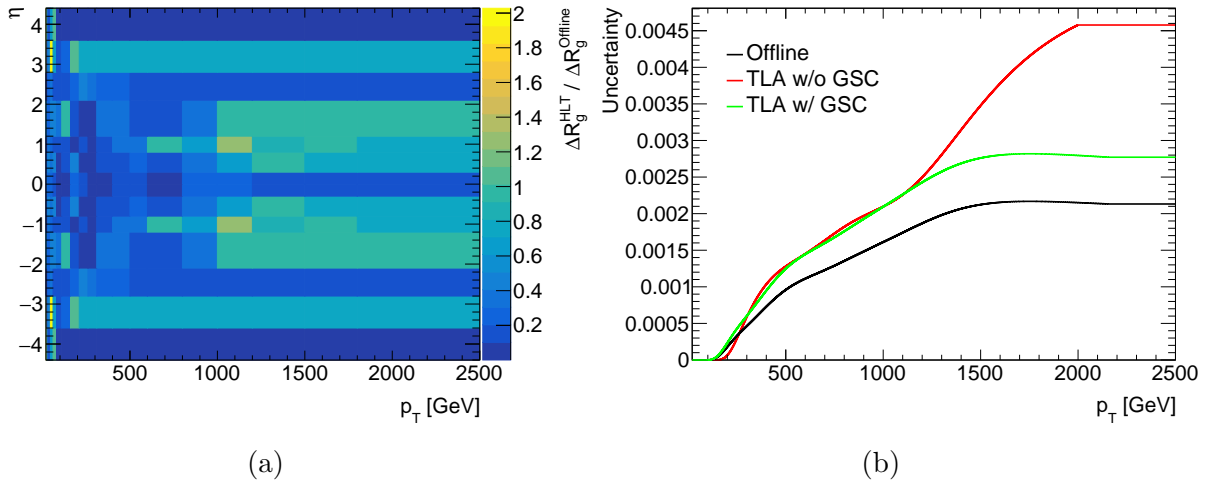


Figure 5.24: Left: Ratio between the gluon response differences for HLT jets and offline jets at the GSC scale. Right: Multijet balance propagation of the flavor response uncertainty.

GSC. This is shown in (a) assuming an unknown flavor composition of the sample and in (b) based on the flavor composition of the PYTHIA QCD sample. Using a sample with unknown flavor composition, the fractional flavor related JES uncertainty of HLT jets with  $p_T \sim 200$  GeV is reduced by  $\sim 50\%$ . For a sample with flavor composition of a PYTHIA QCD sample, the flavor-related uncertainty reduces by  $\sim 85\%$ .

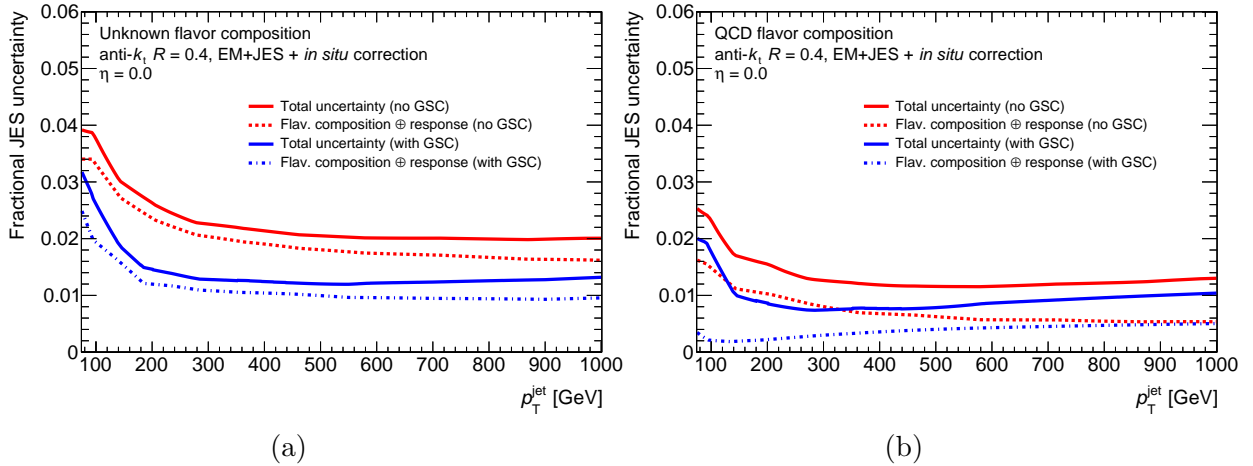


Figure 5.25: Fractional JES uncertainty for HLT jets as a function of  $p_T$  with and without the re-derivation of the flavor uncertainties due to the calorimeter-based GSC. The comparison is shown based on a sample with unknown flavor composition (left) and the flavor composition of a PYTHIA QCD sample (right).

### 5.2.2 Total Uncertainties

The total fractional JES uncertainties and their components are shown in Figure 5.26 for the flavor composition of the background (a) and for the flavor composition of a  $Z'$  signal sample with  $m_{Z'} = 550$  GeV (b). For  $p_T = 200$  GeV, the JES uncertainty for HLT jets is 30% larger than the JES uncertainty for offline jets. Up to  $p_T \approx 250$  GeV the dominant HLT JES component is the non-closure uncertainty between HLT jets and offline jets. Beyond this range, the largest contributions come from the absolute in-situ calibration and the flavor uncertainties.

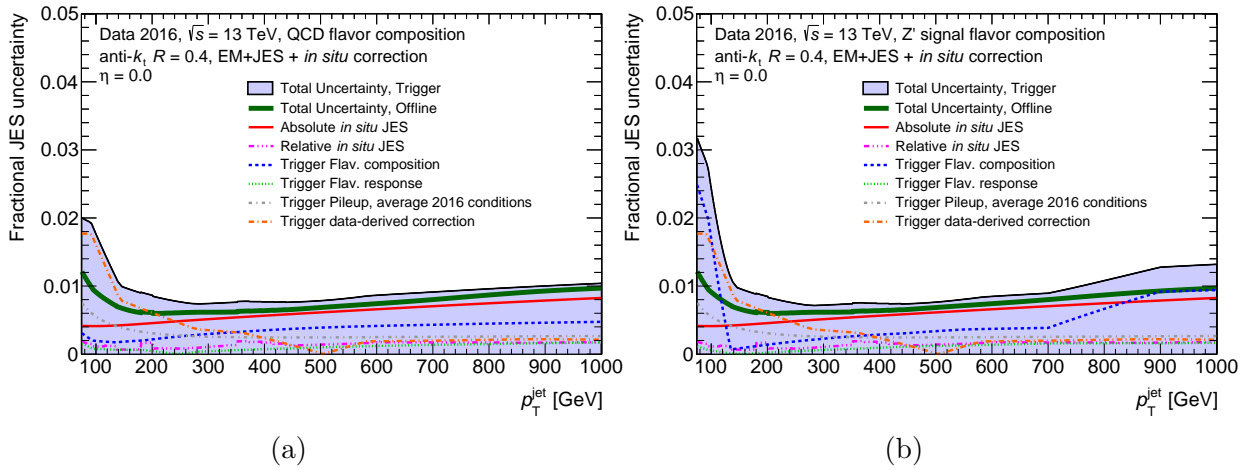


Figure 5.26: The total fractional JES uncertainties and their components for the flavor composition of the background (a) and for the flavor composition of a  $Z'$  signal sample with  $m_{Z'} = 550$  GeV (b)

## 5.3 Reconstruction Efficiency of TLA Jets

An essential validation test for the TLA approach itself is to probe the efficiency of the HLT jet reconstruction with respect to the offline jet reconstruction in the nominal TLA signal region. The reconstruction efficiency for HLT jets is determined using a tag-probe method within dijet events in data and MC. Every jet in the event is subjected to a jet quality selection and jet calibration procedure as outlined in Appendix A.1 and Chapter 5.1. The offline reconstructed events are required to pass one of a few separately tested HLT single jet triggers. The first two leading offline jets should satisfy  $|y^*| < 0.6$  and an invariant mass cut at  $m_{jj} > 400$  GeV. Furthermore every offline jet in the event must have a  $p_T > 50$  GeV and  $|\eta| < 2.8$ .

The tag jet is defined as the offline jet, which matches the trigger jet that fired the trigger within  $\Delta R < 0.4$ . If multiple jets fulfill this criterion, one jet among them is chosen randomly as the tag jet. The random choice avoids biases which could be introduced for example if always the highest  $p_T$  jet was chosen as this would be sensitive to certain event

topologies such as those containing sizable gluon radiation or resolution effects. Probe jets are any other offline jets in the event passing the aforementioned kinematic thresholds. The reconstruction efficiency is defined as the ratio between the number of probe jets that can be matched to a HLT jet within  $\Delta R < 0.4$  and total number of probe jets.

$$\text{Efficiency} = \frac{\#\text{ProbeJets}_{\text{Matched}}}{\#\text{ProbeJets}_{\text{Total}}} \quad (5.16)$$

Figure 5.27(a) shows the reconstruction efficiency as a function of the offline jet  $p_T$  for data (MC) with respect to the HLT\_j110 (HLT\_j100) trigger<sup>4</sup>. Figure 5.27(b) does the same for the HLT\_j380 (HLT\_360) trigger. The HLT\_j110 plot shows an efficiency well above 99.9% while HLT\_j380 is more than 99.8% efficient, within the statistical errors of the limited statistics due to selecting dijet events where the probe has significantly less energy than the tag jet. The overall difference between data and MC is less than 0.1%. Within the TLA signal region both cases show an efficiency above 99.9%.

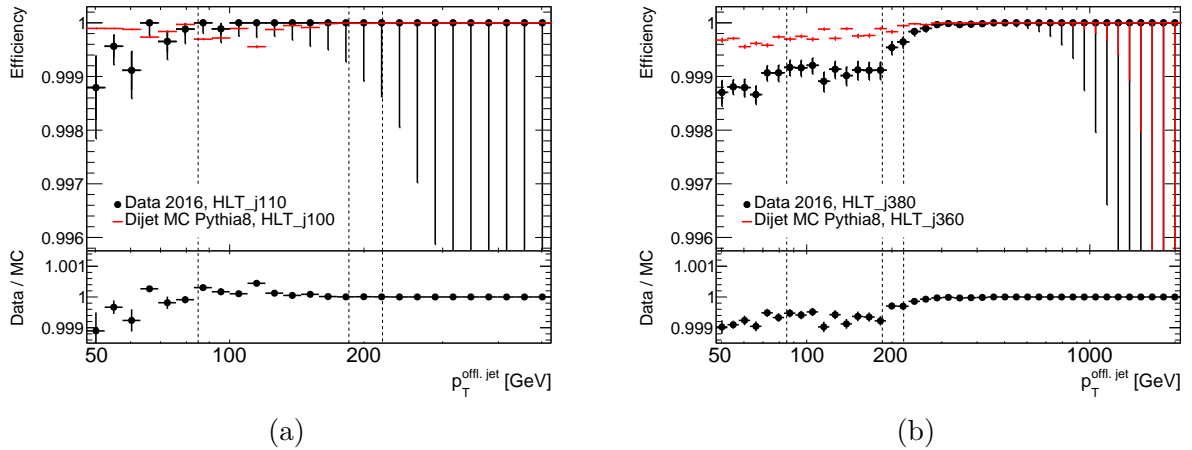


Figure 5.27: The reconstruction efficiency for trigger jets passing the HLT\_j110 (left) and HLT\_j380 triggers (right) with respect to the offline jet  $p_T$ . The upper panel shows the efficiency for data and dijet MC. The lower plot shows the ratio of data to MC. The vertical dashed lines indicate the TLA subleading jet  $p_T$  threshold at 85 GeV and the leading jet  $p_T$  thresholds in the  $|y^*| < 0.3$  and  $|y^*| < 0.6$  signal regions at 185 GeV and 220 GeV.

The fraction of fake jets among the trigger jets is determined in an inverse approach. Events are selected similarly as in the determination of the reconstruction efficiency. Offline jets must have a  $p_T > 25$  GeV and for  $p_T < 50$  GeV a  $JVF < 0.64$  is required to remove pile-up. Additionally  $|\eta| < 2.8(2.6)$  is required for offline (HLT) jets. The stricter kinematic criteria for HLT jets are used to avoid contributions due to resolution effects.

<sup>4</sup>Differences in the used trigger arise between data and MC due to a change in the trigger menu between the 2015 and 2016 data-taking period.

The fake fraction is determined as the number of HLT jets that are *not* matched within  $\Delta R < 0.4$  to a probe jet, in ratio to the total number of HLT jets in the event, not counting the HLT jet which fired the trigger.

$$\text{FakeFraction} = \frac{\#\text{HLTJets}_{\text{Unmatched}}}{\#\text{HLTJets}_{\text{Total}}} \quad (5.17)$$

Figure 5.28(a) shows the fake fraction as a function of the HLT jet  $p_T$  for both data and MC with respect to the HLT\_j110 trigger and Figure 5.28(b) does the same for the HLT\_j380 trigger. For regions with  $p_T > 60$  GeV, where resolution effects near the offline jet cuts have only minor contributions, the fake fraction for both data and MC is below 0.3%. The overall difference between data and MC is less than 0.1%. Within the TLA signal region the fake fraction reduces below 0.2%.

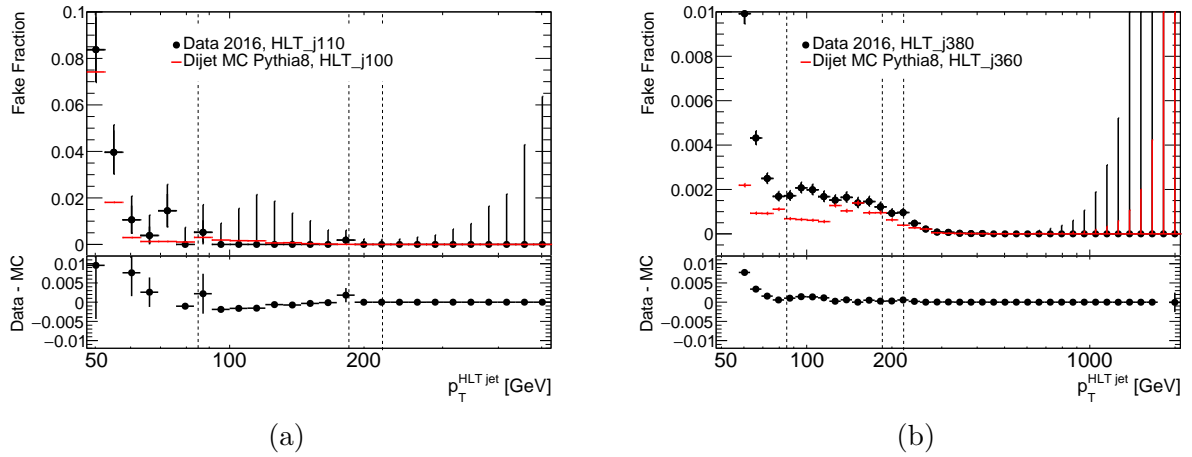


Figure 5.28: The fake fraction for trigger jets passing the HLT\_j110 (left) and HLT\_j380 triggers (right) with respect to the offline jet  $p_T$ . The upper panel shows the fake fraction for data and dijet MC. The lower panel shows the difference of data and MC. The vertical dashed lines indicate the TLA subleading jet  $p_T$  threshold at 85 GeV and the leading jet  $p_T$  thresholds in the  $|y^*| < 0.3$  and  $|y^*| < 0.6$  signal regions at 185 GeV and 220 GeV.

A large fraction of the inefficiencies and fakes result from unproblematic matching inefficiencies, where an offline jet and a HLT jet fall right above the  $\Delta R$  requirement. The remaining cases could result from differences in the jet cleaning procedure and timing differences in the HLT and offline jet reconstruction. In general the impact of these cases is considered negligible for the TLA.

## 5.4 The Dijet Invariant Mass Spectrum

For every event passing the selection criteria of the three TLA signal regions, the invariant mass of the two leading jets is computed to populate the dijet invariant mass spectrum. The  $m_{jj}$  resolution amounts to 4.7% for jets with  $p_T$  of 400 GeV and increases to 4.1% for jets with  $p_T$  of 1 TeV. This is an improvement by up to 22% with respect to the 2015 iteration of the TLA [105] which is largely due to the GSC, that was not derived in the 2015 iteration. The binning of the  $m_{jj}$  spectrum was chosen based on the  $m_{jj}$  resolution. I.e. narrow bins are of advantage to have a potential signal spread over multiple bins and to have a large number of input bins for the data-driven background fit, yet bin sizes should at the same time be greater than the resolution to limit bin migration effects due to the detector resolution. The nominal dijet invariant mass spectra of the TLA as seeded by the L1\_J75 and L1\_J100 triggers are shown in Figure 5.29. The integrated luminosity of the J75 spectrum amounts to  $3.6 \text{ fb}^{-1}$ . The J100 spectrum has an integrated luminosity of  $29.7 \text{ fb}^{-1}$  and is compared to the  $m_{jj}$  spectrum for offline jets from the lowest unrescaled HLT single jet trigger HLT\_j380 scaled to the same luminosity.

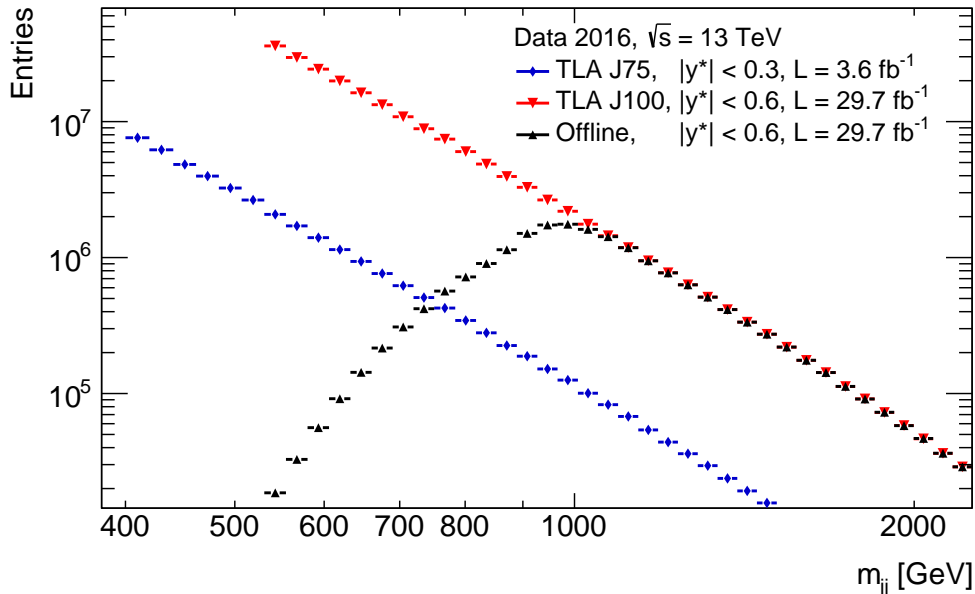


Figure 5.29: Nominal dijet invariant mass spectra of the TLA as seeded by the L1\_J75 and L1\_J100 triggers. The L1\_J100 spectrum is compared to the  $m_{jj}$  spectrum for offline jets, stemming from the lowest unrescaled HLT single jet trigger HLT\_j380.

In addition, the dijet invariant mass spectrum is calibrated with respect to variations between  $\pm 0.5\sigma$  and  $\pm 3\sigma$  of the sources of the JES uncertainty. For this the *strongly reduced representations* are used, in which the 67 independent sources of JES uncertainty are combined into a representation of only three nuisance parameters while preserving the JES correlation information [123]. The TLA scale factor non-closure uncertainty is

separately used as an additional nuisance parameter. The ratio of the JES variations of the mass spectrum with respect to the nominal mass spectrum is shown in Figure 5.30 with respect to the TLA J75  $|y^*| < 0.3$  signal region. These variations serve as templates to respect systematic uncertainties during the statistical analysis in the search phase of the TLA.

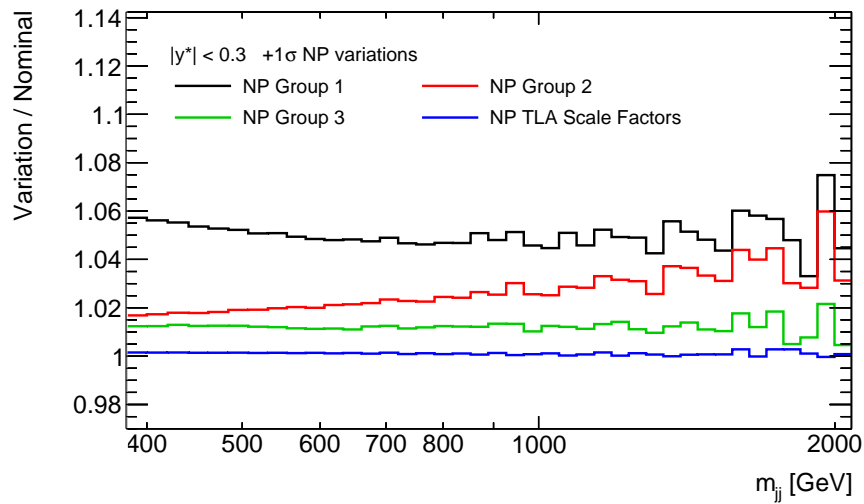


Figure 5.30: Ratio of  $m_{jj}$  spectra varied in the strongly reduced representations of the sources of JES uncertainty and the nominal  $m_{jj}$  spectrum from the J75  $|y^*| < 0.3$  signal region.

In each signal region the QCD background will be estimated from a data-driven background fit. This is achieved in a sophisticated procedure which is detailed in the following chapter.



# Chapter 6

## TLA Background Estimation

### 6.1 Background Estimation Strategy

The TLA background estimation presents one of the main challenges of the analysis. The QCD dijet background is a complex mixture of numerous relevant diagrams, PDFs, showering processes, the detector response and the kinematic selection. An adequate modelling using MC simulations is not possible due to the lack of computing resources required to simulate the high number of dijet events present in the collision data.

Historically, empirical fit functions of three to five free parameters were used to model the background in a single fit. This procedure is called the *global fit*. In the global fit procedure, smooth and monotonically decreasing functions of typically exponential or polynomial forms are employed to search for potential derivations from smoothness such as resonances in the data.

However, it is not *a priori* given that global fits of empirical functions will continue to be suitable as the experimental precision and amount of data increase. Beyond that, the use of the TLA approach brings several further challenges along. First, the statistical precision of the TLA is much larger than that of conventional offline analyses bearing the possibility that shape differences between QCD and the fit function approximations become more pronounced. Second, it is the aspiration of the TLA to cover the  $m_{jj}$  region from the kinematic selection constraint up to the region that is covered by offline analyses [106]. This corresponds to a range of approximately 400 to 2000 GeV. However, already at integrated luminosities of  $\sim 3.4 \text{ fb}^{-1}$  the maximum range where the global fit works reliably is a range of only 400 – 1200 GeV as it was found in the 2015 iteration of the TLA [105]. Third, the background estimation procedure is required to be robust with respect to uncorrelated JES uncertainties. This is especially important for the TLA because the calibration is largely based on a dataset that is smaller than the analysis dataset. Furthermore, the background estimation should be both sensitive and robust with respect to potential signals.

To meet all these goals and requirements for the 2016 analysis iteration, the TLA extends the global fit procedure to a *sliding window fit* (SWiFt). The SWiFt background estimate and the data are the inputs to a statistical analysis procedure in which the goodness of

the fit as well as potential localized excesses are quantified. If a significant excess is found, the mass spectrum is re-fitted with the excess region excluded from the fit. This reduces influence of a potential signal on the background estimate. In this case, the statistical analysis procedure is also repeated with the inclusion of systematic uncertainties. Both SWiFt and the statistical analysis which both make up the “search phase” of the analysis are explained in detail in the following.

## 6.2 Sliding Window Fit (SWiFt)

SWiFt is an extension of the global fit procedure to achieve a reliable background estimate for wider mass ranges. It employs an empirical fit function as well, but applies it only to a window smaller than the total mass range to be fitted. The window then slides bin-by-bin through the total mass range to be fitted and the background estimation is evaluated from the fit result in the central bin of the window at each window position.

Since the  $m_{jj}$  region biased by the kinematic selection cannot be fitted by the monotonically falling functions, the fit cannot be evaluated at the window center at the lower end of the mass range. Here instead, the window is positioned at the lowest possible point and the

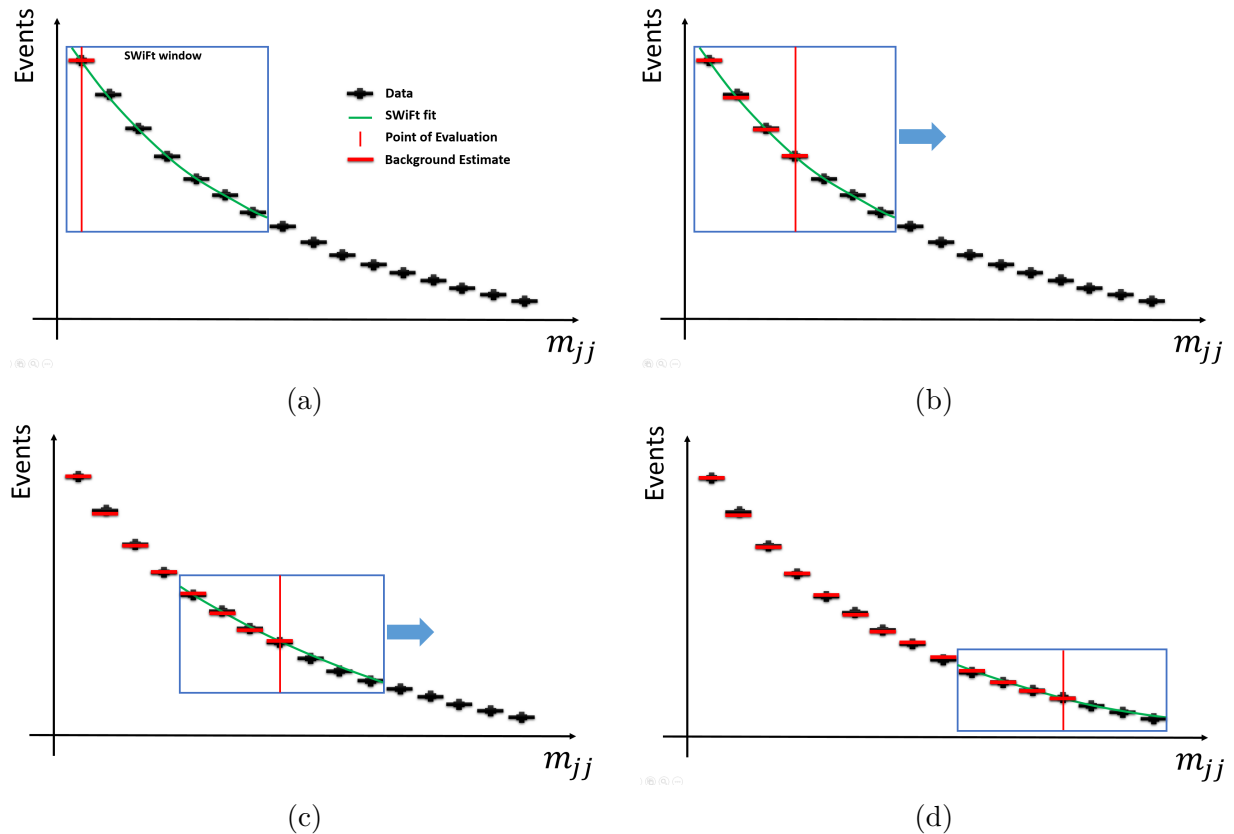


Figure 6.1: Sketch of the sliding window fit “SWiFt”.

point of evaluation is set to the lowest bin within the window and then moved bin-by-bin towards the bin center while the window position is kept fixed (sketched in Figure 6.1(a)). When the point of evaluation reaches the window center (b), it is fixed to the central bin in the window and the window slides bin-by-bin through the mass spectrum (c) until the central bin in the window reaches the upper end of the mass spectrum to be fitted (d). An illustrative animation of the SWiFt procedure can be found in [124].

Eligible empirical functions are chosen among a set of functions that have been employed in past resonance searches [56, 125–128]. The functions that were found most suitable are listed in Table 6.1. The 4PAR and UA2 functions with four degrees of freedom are the nominal choice to provide the background estimate or to derive an uncertainty in the fit function choice, depending on the fit quality. The 5PAR and UA2LOG functions with five degrees of freedom serve as a backup options. The nominal starting points for the fits in the J75 and J100 signal regions are 400 GeV and 531 GeV, respectively, to avoid the bias from the kinematic selection.

Functional form	Label
$f(x) = p_1(1-x)^{p_2}x^{p_3+p_4 \ln x}$	4PAR
$f(x) = \frac{p_1}{x^{p_2}}e^{-p_3x-p_4x^2}$	UA2
$f(x) = p_1(1-x)^{p_2}x^{p_3+p_4 \ln x+p_5 \ln x^2}$	5PAR
$f(x) = \frac{p_1}{x^{p_2}}e^{-p_3x-p_4x^2+p_5 \ln x}$	UA2LOG

Table 6.1: The candidate empirical functions employed within SWiFt in the TLA with  $p_i$  as free fit parameters and  $x = m_{jj}/\sqrt{s}$ .

## 6.3 Statistical Analysis

Once a background estimate is available, a statistical analysis is performed to quantify the agreement between the data and the background. This is done on the basis of two separate test statistics. A  $\chi^2$  test statistic is used to determine the overall fit quality. A BUMP HUNTER test statistic is used to identify and quantify localized excesses on the mass spectrum. Both quantities are compared to a set of pseudo-experiments on each bin of the mass spectrum to derive their associated  $p$ -values. To include systematic uncertainties in the search phase, pseudo-experiments can be drawn from variations of the mass spectrum according to the JES uncertainty nuisance parameters.

### 6.3.1 $\chi^2$ Test Statistic

The  $\chi^2$  test statistic is defined as the quadratic sum of the differences between observed data and background hypothesis, normalized to the background hypothesis. For binned

histograms this corresponds to

$$\chi^2 = \sum_i \frac{(d_i - b_i)^2}{b_i}, \quad (6.1)$$

where  $d_i$  and  $b_i$  are the number of events in data and the background estimate in bin  $i$ . Thus, the  $\chi^2$  test statistic characterizes the sum of the overall discrepancies between data and background hypothesis and is therefore an eligible figure of merit for the goodness of the fit.

In the case of the presence of a localized excess, the interval of the excess can be excluded from the  $\chi^2$  calculation to characterize the goodness of the fit in the remaining spectrum. The  $\chi^2$  test statistic does not distinguish between bin-by-bin correlations of discrepancies and uncorrelated discrepancies, e.g. in three consecutive bins a  $2\sigma$  upward fluctuation, followed by a same-magnitude downward fluctuation, followed by an upward fluctuation, would yield the same  $\chi^2$  value as the same  $2\sigma$  upward fluctuations in three consecutive bins. The latter case however, is of much larger physical interest in terms of a resonance search and is quantified using the BUMP HUNTER algorithm.

### 6.3.2 The BumpHunter Algorithm

The BUMP HUNTER (BH) algorithm[129, 130] is used to identify and quantify localized excesses of the data with respect to the background estimate. The algorithm scans over the mass spectrum using a window of initially two bins at every possible position in the spectrum. The BH window width is gradually increased until the window spans half the mass range of the background estimate.

For each possible window at each position, the algorithm calculates the Poissonian probability of finding a result at least as significant as the observed one if the bins in the window interval  $[m, n]$  were combined into one bin [131]. The number of events in the combined bin is

$$d = \sum_{i=m}^n d_i, \quad b = \sum_{i=m}^n b_i \quad (6.2)$$

for data  $d$  and background  $b$ . In each window the Poissonian probability of finding a more significant excess or deficit in the interval due to a background fluctuation compared to the one observed is

$$t = \begin{cases} \gamma(d, b) & \text{for } d \geq b \\ 1 - \gamma(d + 1, b) & \text{for } d < b, \end{cases} \quad (6.3)$$

where  $\gamma$  is the incomplete lower gamma function

$$\gamma(n, x) = 1 - e^{-x} \sum_{m=0}^{n-1} \frac{x^m}{m!}. \quad (6.4)$$

The BH test statistic  $t_0$  for the mass spectrum is defined as the negative logarithm of  $t_{\min}$ , the smallest  $t$  found in any possible window interval,

$$t_0 = -\ln t_{\min}. \quad (6.5)$$

In case of the presence of a localized excess the interval of the excess can also be excluded from the BH algorithm to characterize the fit quality in the remaining spectrum, i.e. in terms of remaining excesses due to a potential bad fit.

### 6.3.3 $p$ -Values and the ‘look-elsewhere-effect’

Both, the  $\chi^2$  and the BH test statistics are translated into a global  $\chi^2$  and BH  $p$ -value, which determine the probability that the observed test statistics or more extremal values arise due to statistical fluctuations of the whole background hypothesis. This procedure is particularly important for the BH test statistic, where the associated BH  $p$ -value takes the *look-elsewhere-effect* [132] into account, where an apparent statistically significant observation is related to the size of the parameter space in which the observation could principally arise.

The  $p$ -values are determined using pseudo-experiments, where in each bin  $i$  of the background hypothesis a random number is drawn from a Poisson distribution around  $b_i$  to serve as the simulated number of events  $N_{\text{PE},i}$  in each bin for the respective pseudo-experiment. The pseudo-experiments are repeated several times and for each pseudo-experimental outcome the  $\chi^2$  and BH test statistics are determined with respect to the background hypothesis. The global  $\chi^2$  and BH  $p$ -values are the number of pseudo-experiments with a larger value of the test statistic compared to the values found in data divided by the total number of pseudo-experiments.

A BH  $p$ -value below 0.01 marks the required significance of an excess to be considered a potential discovery. A  $\chi^2$   $p$ -value greater than 0.05 is the requirement on the fit quality to yield a valid background estimate. In this approach the fluctuations of the background hypothesis are purely statistical. If systematic uncertainties are to be taken into account as well, the determination of the pseudo-experiments and their associated test statistics is more complex.

### 6.3.4 Systematic Uncertainties

To account for potential non-smoothnesses in the calibration, uncorrelated components of the JES systematic uncertainty can be taken into account. For this, the search phase strategy is complemented by the following optional procedure.

The background estimate of the nominal calibrated data and the determination of the associated BH test statistic remains unaltered. The pseudo-experiments which determine the BH  $p$ -value, however, are drawn in a different manner which depends on the smoothness of the JES uncertainties in comparison to the smoothness of the data. The pseudo-experiments are drawn for each  $m_{jj}$  bin using the number of events in the nominal background estimate  $N_{\text{bkg},i}^{\text{nominal}}$  as a basis. This number is fluctuated according to a random number drawn from a Gaussian prior  $\theta$  on the difference between the nominal data  $N_{\text{data},i}^{\text{nominal}}$  and the JES-shifted template data  $N_{\text{data},i,j}^{\text{template}}$  which is shifted according to the variations in the JES nuisance parameters  $j$ . The number of events of a pseudo-experiment  $N_{\text{PE},i}$  in bin  $i$  is given by

$$N_{\text{PE},i} = N_{\text{bkg},i}^{\text{nominal}} + \theta_j \left( N_{\text{data},i}^{\text{nominal}} - N_{\text{data},i,j}^{\text{template}} \right). \quad (6.6)$$

The resulting pseudo-data distributions are fitted with the nominal procedure and their corresponding BH test statistics are determined and related to the nominal BH test statistic in data as described in the previous section. The resulting BH  $p$ -value respects the systematic JES uncertainties with respect to their impact on differences between the smoothness of the data and the templates of the JES nuisance parameter variations. If, for example, the calibration is not smooth and causes an excess in a certain  $p_T$  and  $m_{jj}$  region, the JES uncertainty should account for this due to larger nuisance parameters in that region. The distributions of the pseudo-experiments are then unsmooth themselves such that both the BH test statistic in data, as well as the average BH test statistic from the pseudo-experiments, will be shifted to larger values. This ensures that the overall BH  $p$ -value is not necessarily small. On the other hand, if a real signal was present and the calibration was smooth, the JES uncertainty should be smooth as well and the BH test statistic in data would be larger than the average BH test statistic in the pseudo-experiments leading to a small BH  $p$ -value.

## 6.4 SWiFt Window Width

An essential parameter for the performance the background estimation procedure is the SWiFt window width. This parameter needs to be optimized because it is expected to be a compromise between two opposing dependencies.

A narrow window implies a more flexible fit and a better capability to compensate shape differences between QCD and the empirical function. However, in the presence of potential resonant signals, a wider window fit is anchored more strongly by the sidebands of the signal and is less likely to adapt its shape to the signal. Therefore a wider window fit should provide a more robust background estimation in the presence of a signal leading also to a superior signal sensitivity compared to narrow windows. To quantify both effects, the effect of the window width on the fit quality in terms of the  $\chi^2$   $p$ -value and the BH  $p$ -value is studied within and without the presence of artificially injected signals on different test samples. These test samples are:

- A high-statistics pseudodata  $m_{jj}$  distribution of a NLOJET++ sample, scaled to  $29.7 \text{ fb}^{-1}$  of data. Even at the given limited statistical precision of the MC, the sample is useful because it is guaranteed signal-free and represents the equivalent statistical power of the 2016 J100 dataset.
- The  $m_{jj}$  distribution of a fraction of the 2016 J100 dataset (period F) corresponding to  $2.8 \text{ fb}^{-1}$  of data, which is less than the 2015 dataset. Although the data sample is not guaranteed signal-free, it is useful as it accounts for detector effects and a non-approximated physical background.

The study is conducted with respect to the J100 signal region, using the nominal SWiFt 4PARAM function and the fit starting point of 531 GeV. The SWiFt window width is parametrized by the number of bins which span half of the window. It is important to note, that the binning of the testing samples differ: The compared window halfwidths of (13, 17, 20, 23) in the NLOJET++ sample correspond to a window of roughly the same GeV range as window halfwidths of (7, 10, 13, 17) bins in the 2016 TLA dataset.

Three examples of SWiFt background estimates and the residuals with respect to the  $m_{jj}$  distribution of the 2016 period F dataset are given in Figure 6.2 (a-c) for increasing SWiFt window halfwidths. Figure 6.2 (d) shows the  $\chi^2$   $p$ -value of the respective SWiFt background estimates as a function of the SWiFt window halfwidth. The plots confirm the expectation that narrow windows provide a better fit quality. For SWiFt window halfwidths  $< 15$ , the  $\chi^2$   $p$ -value becomes larger than the required 0.05.

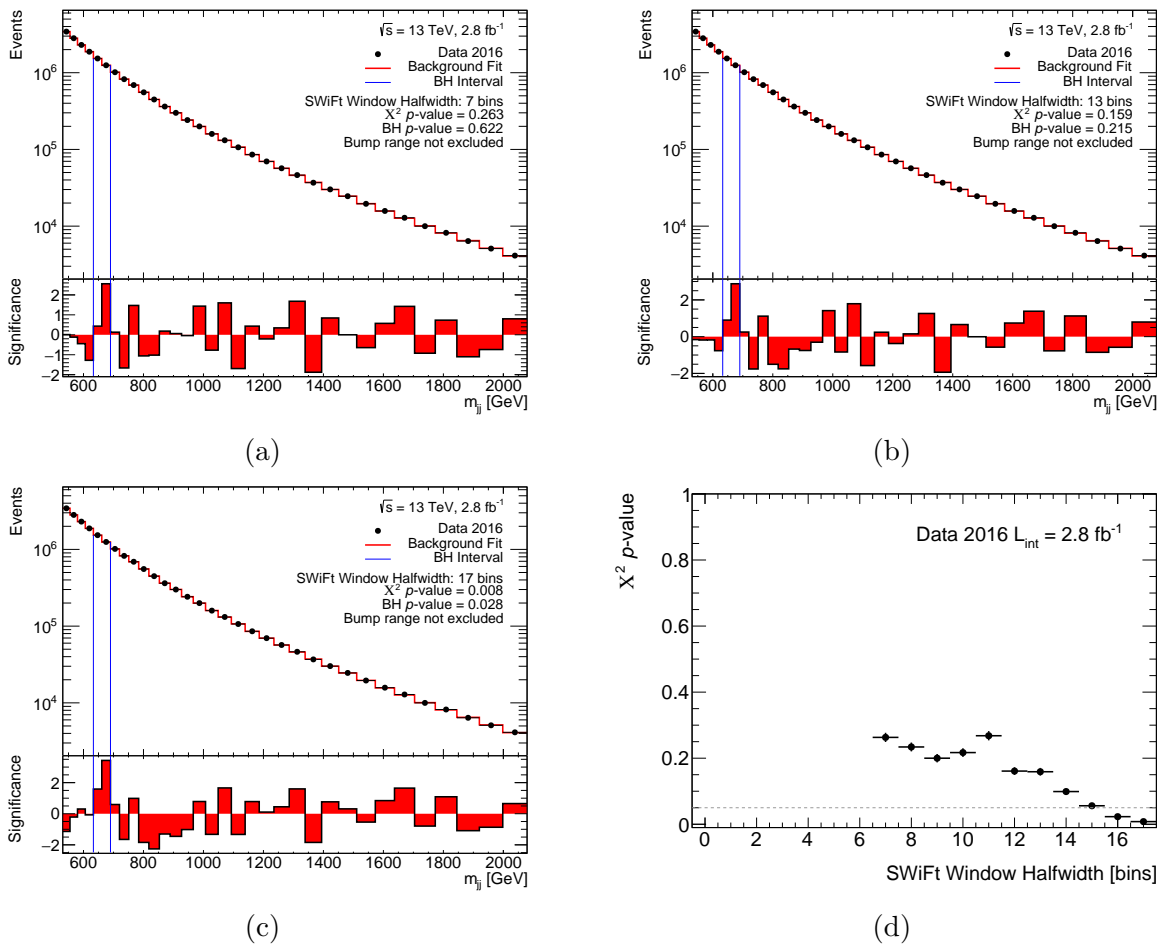


Figure 6.2: (a-c) shows three examples of SWiFt background estimates and the residuals with respect to the  $m_{jj}$  distribution of the 2016 period F dataset for increasing SWiFt window halfwidths. The  $\chi^2$   $p$ -value of the respective SWiFt background estimates as a function of the SWiFt window halfwidth is shown in (d).

To examine the fit dependence on the SWiFt window width in the presence of signal, Gaussian signals of relative widths between 3% and 15% are injected at desired mass points in the NLOJET++ pseudodata  $m_{jj}$  distribution and scaled to a significant signal cross-section. Figure 6.3 (a-c) show the SWiFt background estimates for different window widths in the presence of a Gaussian signal of 5% relative width injected at 950 GeV scaled to a cross-section of  $7.7 \text{ pb}^{-1}$ , which corresponds to the BH  $p$ -value discovery threshold for a SWiFt fit with the maximum window width (23 bins window halfwidth). The BH  $p$ -value of the background estimate for this distribution as a function of the SWiFt window halfwidth is given in Figure 6.3 (d).

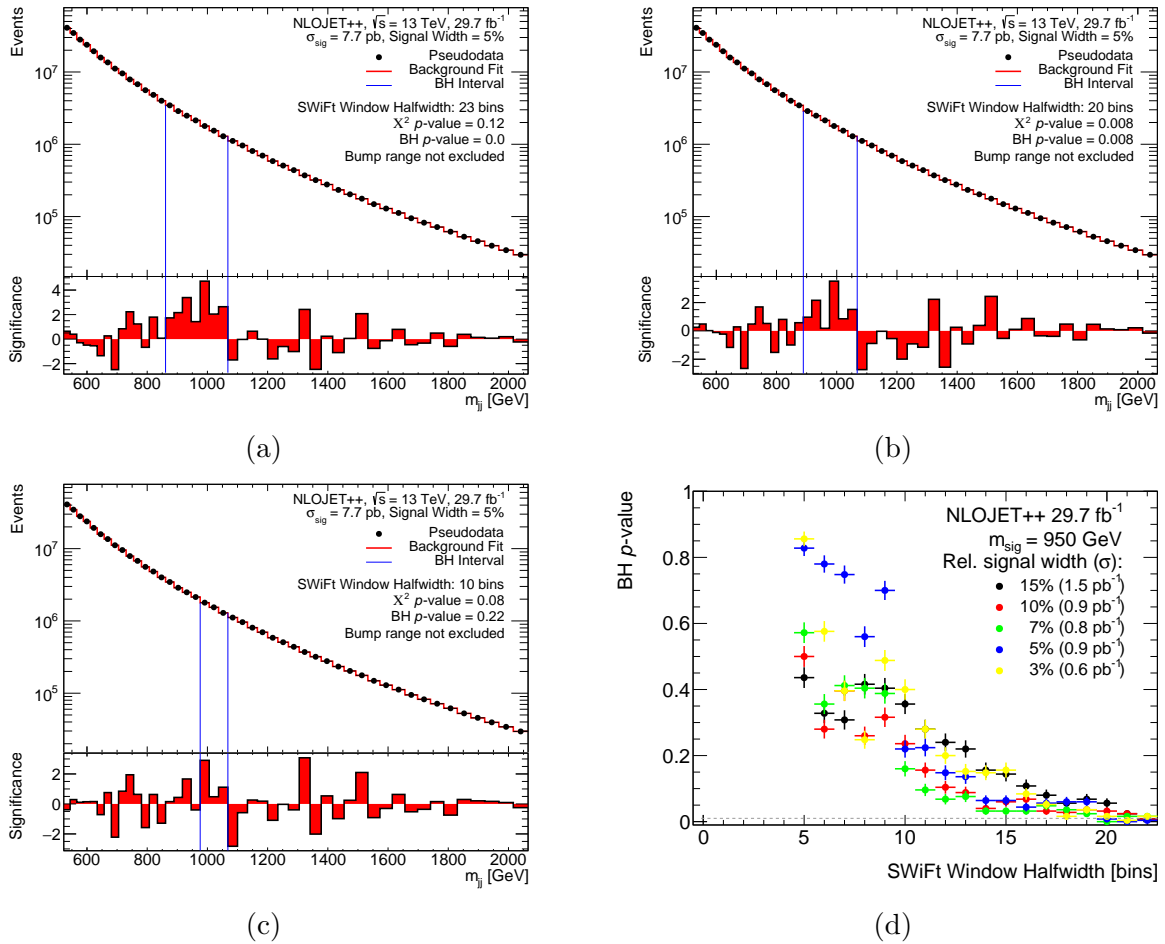


Figure 6.3: Three examples of SWiFt background estimates and the residuals with respect to the  $m_{jj}$  distribution of a signal+background distribution for increasing SWiFt window halfwidths (a-c). The injected signal is a Gaussian of 5% relative width injected at 950 GeV scaled to a cross-section of  $7.7 \text{ pb}^{-1}$ , which corresponds to the BH  $p$ -value discovery threshold for a SWiFt fit with the maximum window width (23 bins window halfwidth). The BH  $p$ -value of the respective SWiFt background estimates as a function of the SWiFt window halfwidth is shown in (d).

It can be concluded that the search phase sensitivity towards a given signal increases with larger SWiFt windows. To test how this finding is influenced by local fluctuations in a realistic dijet mass spectrum, 5% relative width Gaussian signals at mass points between 550 GeV and 1850 GeV are injected in the 2016 period F dataset. Their normalization is iteratively scaled up until the BH  $p$ -value threshold is exceeded ( $<0.01$ ). The signal cross-section needed to reach the threshold (discovery cross-section) for each mass point can be compared for different SWiFt window widths. Figure 6.4 shows for each tested window width in the upper panels the discovery cross-section as a function of the mass point where the signal was injected and in the lower panels the mass range of highest excess determined by the BH algorithm.

Generally the increased search phase sensitivity of wider windows is confirmed. However in the case of very large window halfwidths of 17 bins, the mass range of highest excess as

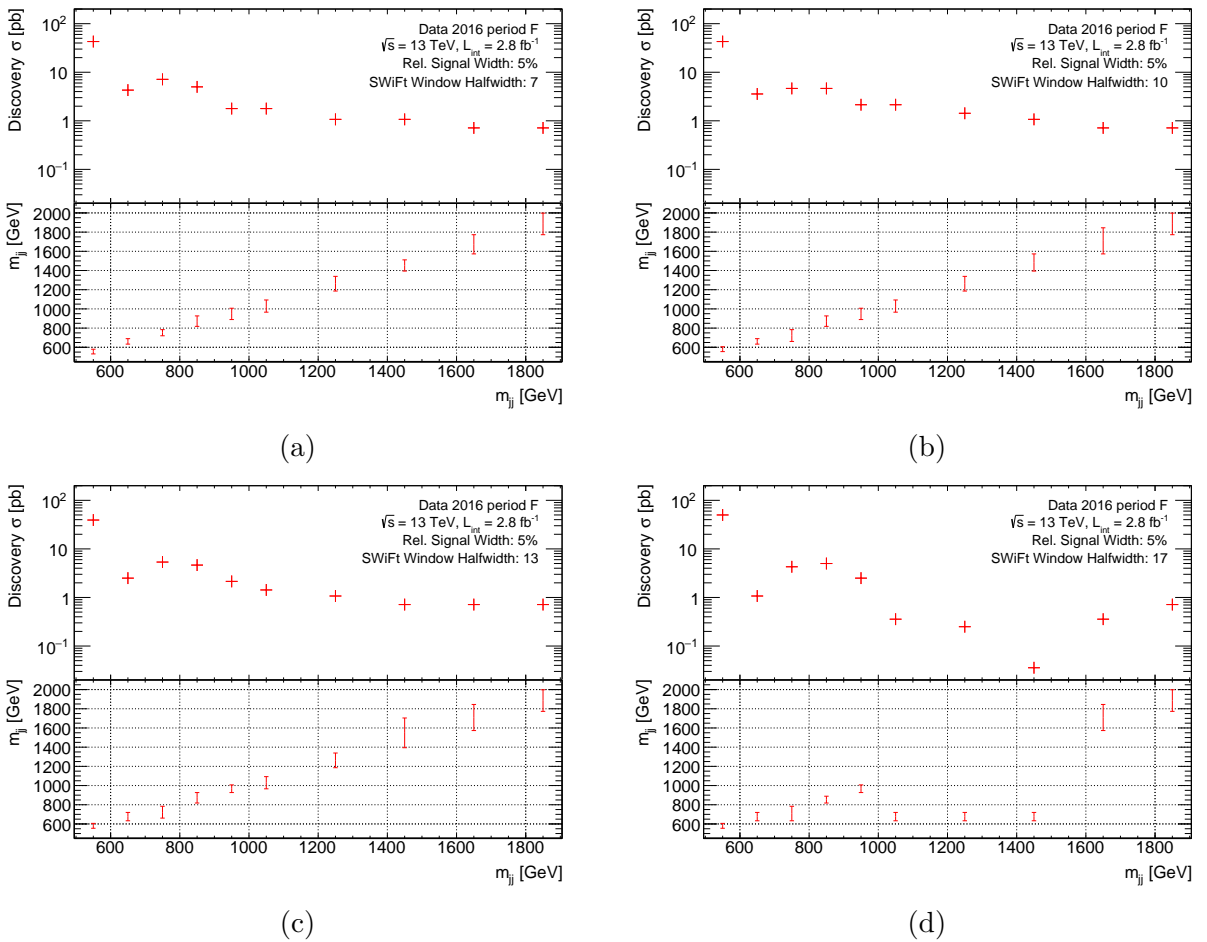


Figure 6.4: The discovery cross-section of an injected Gaussian signal of 5% width as a function of the mass point where the signal was injected (upper panel) and the mass range of highest excess determined by the BH algorithm (lower panel). Both compared for different SWiFt window halfwidths (a-d).

determined by the BH algorithm is for some mass points not consistent with the mass of the injected signal. In these cases the wide window SWiFt fit is not flexible enough and features already without injected signal a slight excess at the low end of the spectrum. The injected signal biases the SWiFt fit and causes it to tilt, which leads to the increase of the already present excess at the low end.

Moreover, the robustness of the background estimate in presence of signals depends on the SWiFt window width. This can be studied by comparing the background estimate in absence of any signals to the two separate cases of an injected signal with signal cross-section right above and right below the discovery cross-section. In the case of a signal cross-section right above the discovery cross-section, the BH  $p$ -value threshold is exceeded ( $<0.01$ ) and the search phase procedure requires to refit the spectrum while excluding the region of highest excess from the fit. Ideally the background estimate is then not influenced by the signal and is similar to the background estimate in absence of signals. In the case of a signal cross-section right below the discovery cross-section, a window exclusion is not envisaged and therefore the background estimate is influenced by the signal. The comparison between these two cases is shown in Figure 6.5 for increasing SWiFt window halfwidths. The upper panel shows the ratio of the fit in presence of signals in the two cases (green: signal above threshold, blue: signal below threshold) to the background estimate in absence of signals and compares the ratio to the relative statistical uncertainty (gray-dashed). The middle (bottom) panel shows in green (blue) the residuals of the background estimate in presence of the signal above (below) threshold and in light red the residuals of the background estimate in absence of signals. For all shown window widths the background estimate for a signal above threshold is more similar to the background estimate in absence of signal compared to the case of signals below threshold. This validates the window exclusion procedure. In addition, the residuals after window exclusion indicate a significantly larger signal excess, as expected. For window halfwidths  $\geq 16$  bins, the fit ratio for signals above threshold is within the relative statistical uncertainty of the pseudodata, whereas for window halfwidths as small as 10 bins, the statistical uncertainty is exceeded. Generally the background estimate is more robust for larger SWiFt window widths.

From these signal injection studies it can be concluded that the SWiFt window width is optimally chosen to be as wide as possible, as long as the fit quality is sufficient. Therefore a window halfwidth of 13 bins in the binning of the 2016 dataset (corresponds to 20 bins in the NLOJET++ sample) is taken as the nominal choice.

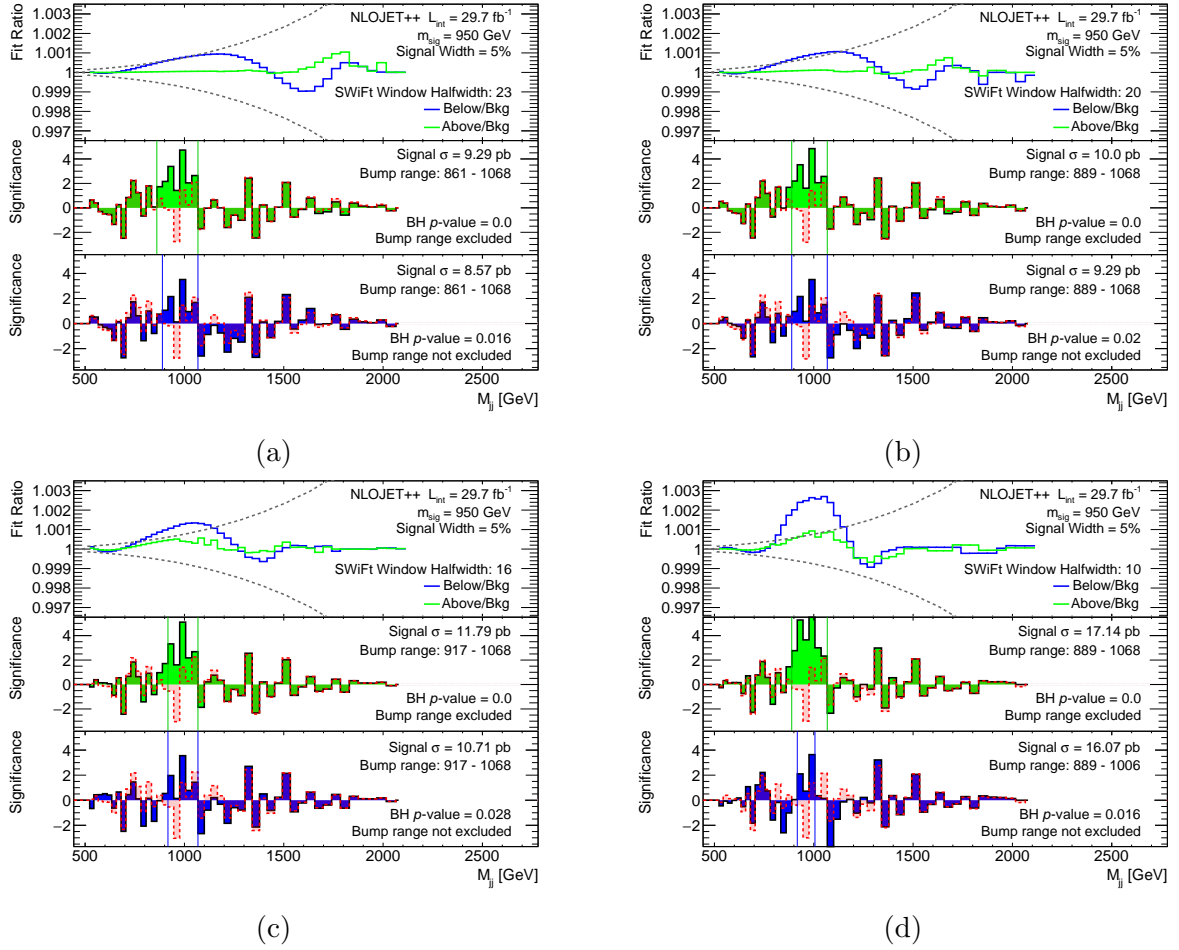


Figure 6.5: Comparison of the influence of the SWiFt window width on the robustness of the background estimation in presence a Gaussian signal of 5% relative width injected at a mass point of 950 GeV. Upper panel: Ratio of the fit in presence of signals in the cases of a signal above threshold (green) and a signal below threshold (blue) to the background estimate in absence of signals and comparison to the relative statistical uncertainty (gray-dashed). Middle panel: Residuals of the background estimate in presence of the signal right above threshold (green) compared to the residuals of the background estimate in absence of signals (light red). Bottom panel: Residuals of the background estimate in presence of the signal right below threshold (blue) compared to the residuals of the background estimate in absence of signals (light red). Figures (a-d) compare decreasing SWiFt window halfwidths.

## 6.5 Background Estimation Robustness

With the nominal choice of SWiFt parameters the robustness of the background estimate is further studied in the presence of signals of varying widths injected at different mass points in the  $m_{jj}$  spectra of the 2016 period F dataset and the NLOJET++ pseudodata. For these cases the background estimates with and without window exclusion are compared in a similar fashion as shown in Figure 6.5. The case studies shown in the following (Figures 6.6-6.8) represent signals injected at a central mass point of 950 GeV (a,b) as well as a mass point closer to the edge of the fit range at 650 GeV (c,d) where the background estimate cannot be evaluated at the center of the SWiFt window. The relative widths of the injected signals are 5%, 10% and 15% shown in Figures 6.6, 6.7 and 6.8 respectively. In (a,c) the signals were injected in the NLOJET++ pseudodata as background, while (b,d) are based on the 2016 period F dataset.

For central signals of relative widths smaller 10% and exclusion of the region of highest excess, the difference between the background estimates with and without signal is below 0.1% and within the statistical uncertainties of the underlying background sample. For signals right below the discovery threshold, with the signal window not excluded from the fit, the difference is slightly larger. It is demonstrated that the background estimation procedure is more robust for narrow signals. Especially for signals with relative widths larger 10% the influence of the signal, even after window exclusion, is considerably larger than the statistical uncertainty. For signals injected closer to the edges of the fit range (650 GeV), where the background estimate cannot be evaluated at the center of the SWiFt window, the influence of the signal is also slightly larger when compared to central signals. This acceptable discrepancy is expected because in this case the fit is not able to converge to wide sidebands to the left side of the signal.

From these studies it is concluded that the background estimate is robust in presence of Gaussian signals with relative widths of up to 10%. For Gaussian signals with relative widths larger 10% the background estimate becomes considerably biased and therefore no reliable limits can be set on these.

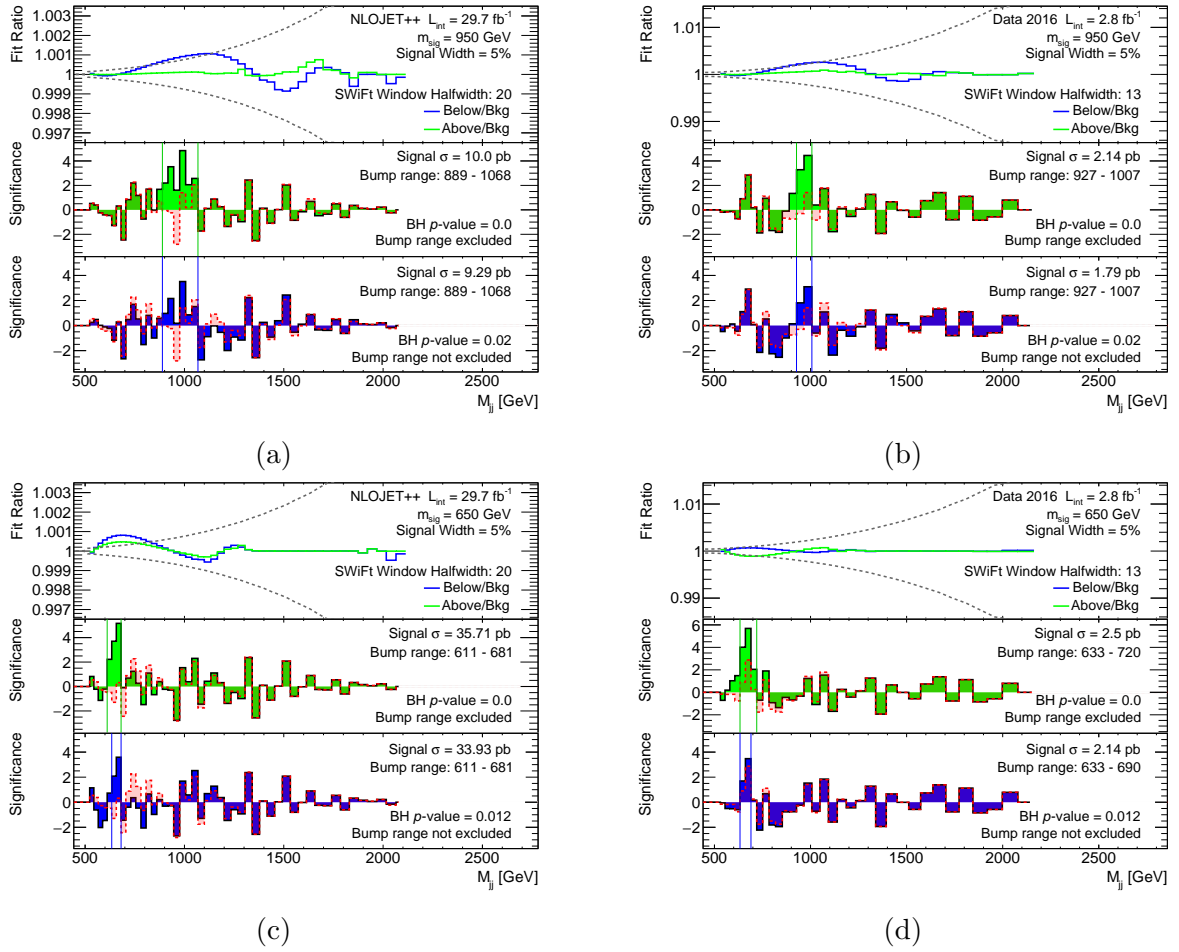


Figure 6.6: Comparison of the robustness of the background estimation in presence of Gaussian signals of 5% width injected at central masspoints at 950 GeV (a,b) and mass-points towards the edge of the spectrum at 650 GeV (c,d) on an  $m_{jj}$  background from a NLOJET++ pseudodata sample (a,c) and the 2016 period F dataset (b,d). Upper panel: Ratio of the fit in presence of signals in the cases of a signal above threshold (green) and a signal below threshold (blue) to the background estimate in absence of signals and comparison to the relative statistical uncertainty (gray-dashed). Middle panel: Residuals of the background estimate in presence of the signal right above threshold (green) compared to the residuals of the background estimate in absence of signals (light red). Bottom panel: Residuals of the background estimate in presence of the signal right below threshold (blue) compared to the residuals of the background estimate in absence of signals (light red).

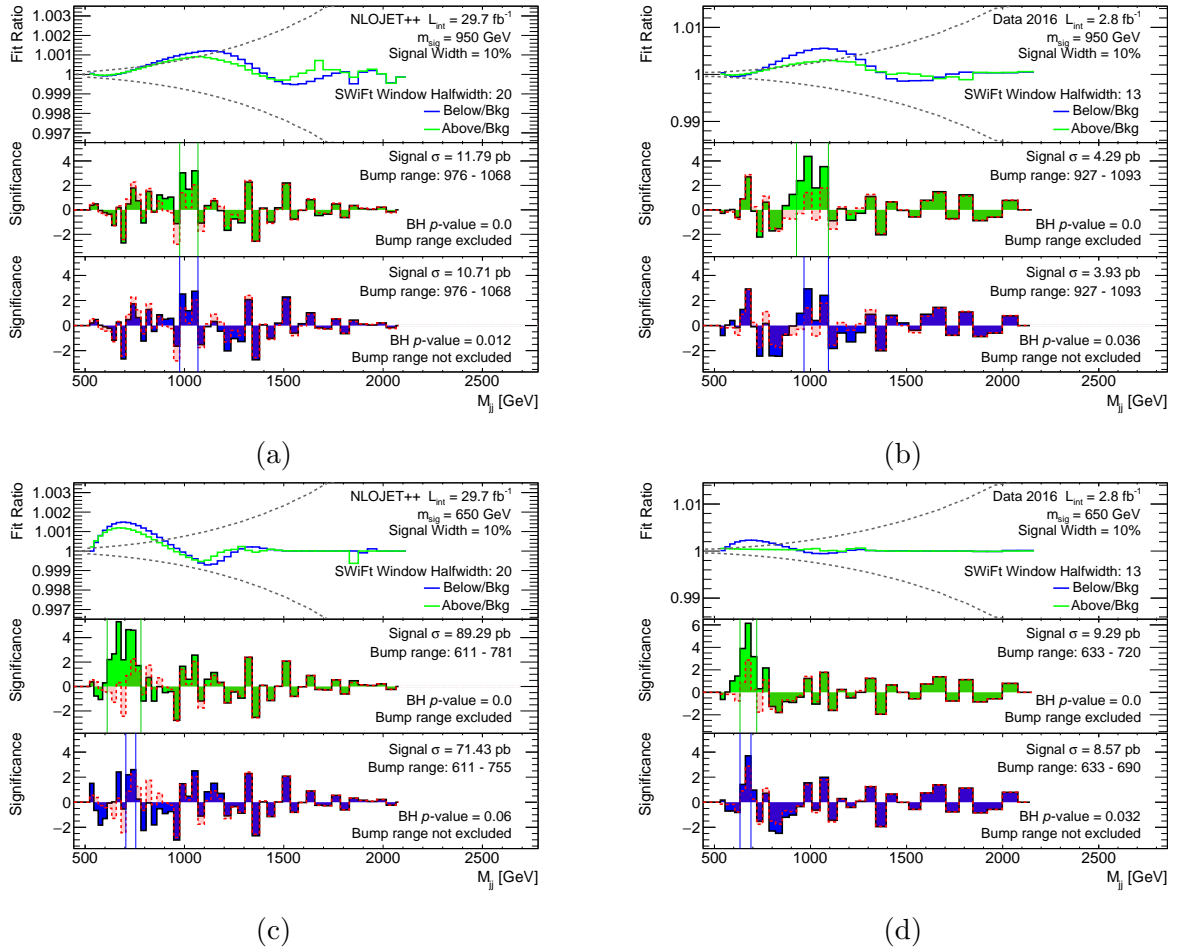


Figure 6.7: Comparison of the robustness of the background estimation in presence of Gaussian signals of 10% width injected at central masspoints at 950 GeV (a,b) and mass-points towards the edge of the spectrum at 650 GeV (c,d) on an  $m_{jj}$  background from a NLOJET++ pseudodata sample (a,c) and the 2016 period F dataset (b,d). Upper panel: Ratio of the fit in presence of signals in the cases of a signal above threshold (green) and a signal below threshold (blue) to the background estimate in absence of signals and comparison to the relative statistical uncertainty (gray-dashed). Middle panel: Residuals of the background estimate in presence of the signal right above threshold (green) compared to the residuals of the background estimate in absence of signals (light red). Bottom panel: Residuals of the background estimate in presence of the signal right below threshold (blue) compared to the residuals of the background estimate in absence of signals (light red).

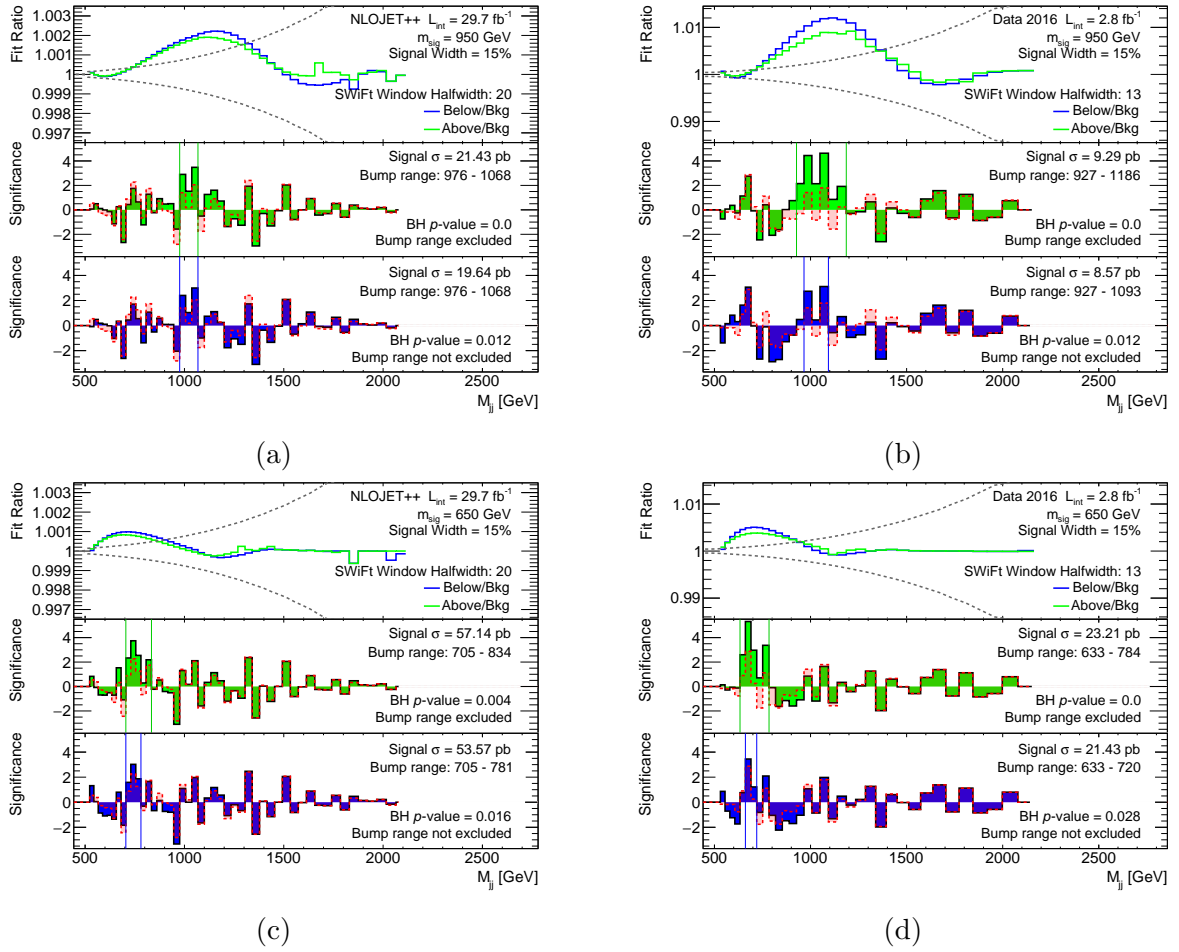


Figure 6.8: Comparison of the robustness of the background estimation in presence of Gaussian signals of 15% width injected at central masspoints at 950 GeV (a,b) and mass-points towards the edge of the spectrum at 650 GeV (c,d) on an  $m_{jj}$  background from a NLOJET++ pseudodata sample (a,c) and the 2016 period F dataset (b,d). Upper panel: Ratio of the fit in presence of signals in the cases of a signal above threshold (green) and a signal below threshold (blue) to the background estimate in absence of signals and comparison to the relative statistical uncertainty (gray-dashed). Middle panel: Residuals of the background estimate in presence of the signal right above threshold (green) compared to the residuals of the background estimate in absence of signals (light red). Bottom panel: Residuals of the background estimate in presence of the signal right below threshold (blue) compared to the residuals of the background estimate in absence of signals (light red).

## 6.6 Expected Sensitivity

With the nominal choice of SWiFt parameters the search phase sensitivity can be estimated for Gaussian signals of 3-10% width injected at mass points between 550 GeV and 1850 GeV. The discovery cross-sections as well as the range of the associated excess is given in Figure 6.9 for the different signal widths as a function of the mass points. As expected the sensitivity is highest for narrow signals because here the fit converges more strongly towards the larger sidebands of the signal and is less likely to adapt to the flanks of the signal.

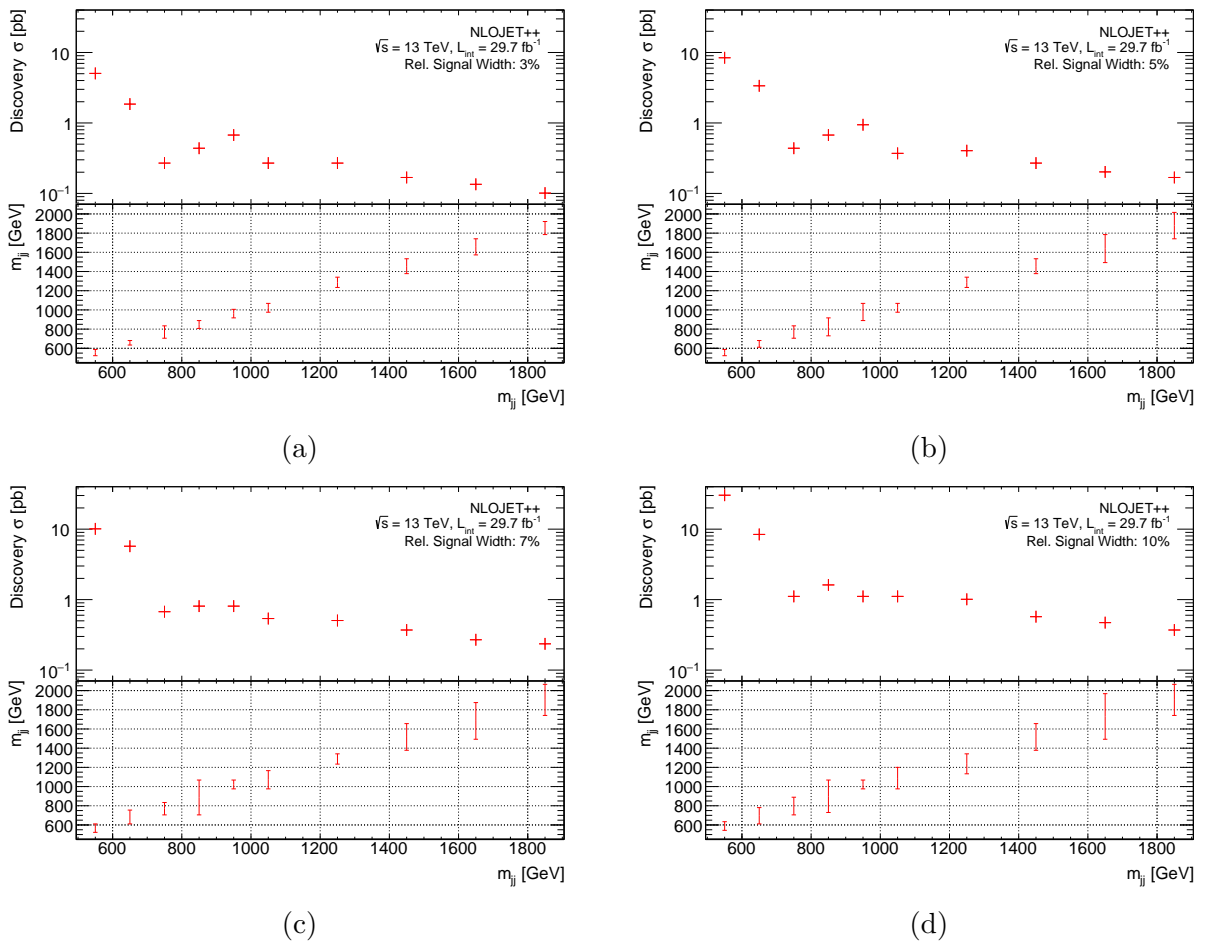


Figure 6.9: The discovery cross-section of Gaussian signals of different widths as a function of the mass point where the signal was injected (upper panel) and the mass range of highest excess determined by the BH algorithm (lower panel). (a-d) compare different relative widths of the Gaussian signals.

## 6.7 Unblinding Strategy

The running of the search phase on the 2016 dataset happens in a strictly defined *unblinding* procedure. This procedure is intended to reduce *experimenter's bias* [133] and is outlined in a simplified form in the following. The dataset is initially fitted using SWiFt with the 4PAR and UA2 functions and the nominal SWiFt window halfwidth of 13 bins and the fit result is analyzed using the BH algorithm.

- If the fit quality is sufficient with a  $\chi^2$   $p$ -value  $> 0.05$  the data is refitted allowing for the exclusion of the window of highest excess as identified by the BH algorithm.
  - If after refitting with window exclusion a BH  $p$ -value  $> 0.01$  is found, no excess is considered significant.
  - Else, if after refitting with window exclusion a BH  $p$ -value  $< 0.01$  is found, the excess is considered significant.
- If the fit quality is insufficient with a  $\chi^2$   $p$ -value  $< 0.05$  and this is *not* due to an excess with a BH  $p$ -value  $< 0.01$ , the 5PAR and UA2LOG are added to the pool of candidate functions. If the result is unchanged after refitting using the functions with additional degrees of freedom the SWiFt window halfwidth will be decreased by one bin per iteration.
- If a  $\chi^2$   $p$ -value  $< 0.05$  and a BH  $p$ -value  $< 0.01$  is found, the data is refitted allowing for a window exclusion of the region of highest excess identified by the BH algorithm.
  - If after refitting with window exclusion a  $\chi^2$   $p$ -value  $> 0.05$  and a BH  $p$ -value  $> 0.01$  for the regions outside of the window and a BH  $p$ -value  $< 0.01$  of the overall spectrum is found, the excess is considered significant.
  - Else the data will be refitted with the functions of additional degrees of freedom or the SWiFt window width will be decreased by two bins per iteration.
- If a significant excess is found, the search phase procedure is repeated including systematic uncertainties. If the excess is still significant including systematic uncertainties, it is considered a potential discovery.
- Else, limits are set on new physics models using the obtained background estimate.

## 6.8 Dependence on Calibration Smoothness

The high demands which the TLA imposes on the smoothness of the jet calibration procedure can be heuristically justified by an invalid search phase result on the J75 data. This is demonstrated in the following on the basis of an example where the J75 data was calibrated according to the unsuitable absolute in-situ calibration curve based on a Gaussian smoothing kernel which was shown in Figure 5.15. This is in contrast to the dedicated in-situ calibration curve based on a polynomial fit (shown in Figure 5.16) which is used to derive the nominal TLA result. The Gaussian smoothing in-situ calibration curve is used within the TLA to derive an invalid result containing a calibration-induced excess. This dependence of the search phase on the smoothness of the calibration is *ex post* accounted for by the derivation of the alternative in-situ calibration curve and the addition of systematic uncertainties to the unblinding procedure.

### 6.8.1 Example of a Calibration-induced Excess

The search phase result on the  $m_{jj}$  spectrum of the J75 data which was calibrated using the inadequate Gaussian smoothing in-situ calibration curve is shown in Figure 6.10(a). With a  $\chi^2$   $p$ -value = 0.044 < 0.05 and a BH  $p$ -value = 0.001 < 0.01, the distribution is to be refitted with the window of highest excess (555 to 690 GeV) excluded from the fit. The search phase result after window exclusion is shown in Figure 6.10(b) with a  $\chi^2$   $p$ -value = 0.18 > 0.05 and a BH  $p$ -value = 0.00 < 0.01. Without the addition of systematic uncertainties this corresponds to a significant excess. A set of tests that link the excess to an unsmoothness in the JES calibration are presented in the following.

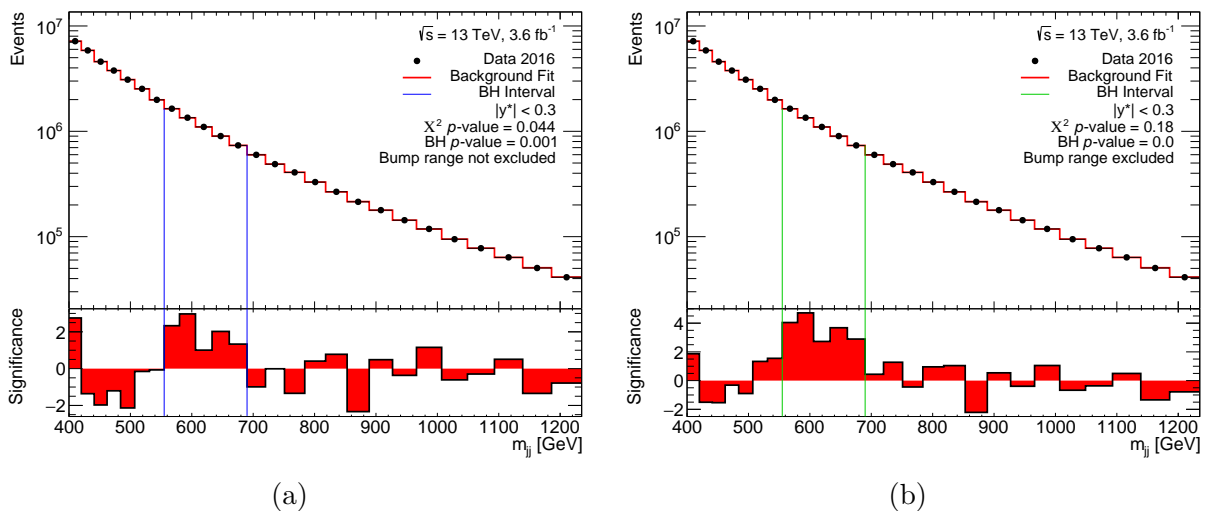


Figure 6.10: The search phase result on the  $m_{jj}$  spectrum of the J75 data which was calibrated using the inadequate Gaussian smoothing in-situ calibration curve. The result is shown (a) without and (b) with window exclusion of the most discrepant region.

### Calibration Stages

The J75 data is re-calibrated to the GSC scale and to the individual calibration stages of the in-situ calibration ( $\eta$ -intercalibration, scale factors and the absolute in-situ correction) to further narrow down the source of the excess. Figure 6.11 shows the residuals of SWiFt fits to the resulting  $m_{jj}$  distributions at each respective calibration stage.

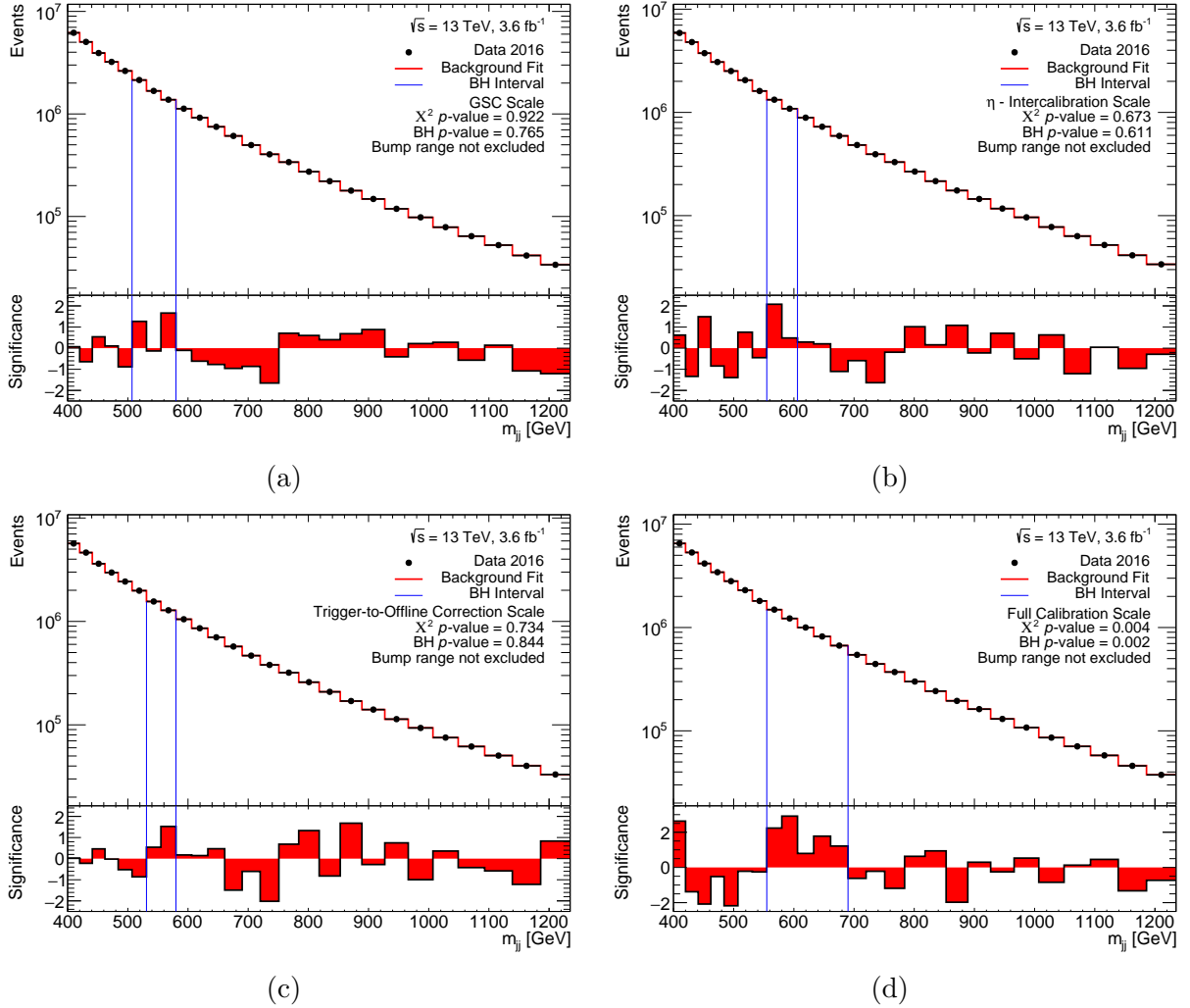


Figure 6.11: Search phase results on the  $m_{jj}$  distributions at individual stages of the calibration, (a) GSC scale, (b)  $\eta$  - intercalibration scale, (c) Trigger-to-Offline correction scale, (d) full calibration scale including the absolute in-situ correction based on Gaussian smoothing.

Except for the very last stage which includes also the absolute in-situ correction, the BH  $p$ -values are moderate and the residuals are largely within the statistical uncertainty of the data. This suggests that an unsmoothness in the absolute in-situ calibration curve induces the excess.

### Absolute in-situ calibration smoothness

The derivation of the absolute in-situ calibration curve contains a Gaussian smoothing procedure. The effect of the smoothing on the excess can be studied by modifying the smoothing kernel to create further variations of the calibration curve corresponding to a higher or lower degree of smoothing. The resulting calibration curves of three different different smoothing variations compared to the nominal calibration curve are shown in Figure 6.12.

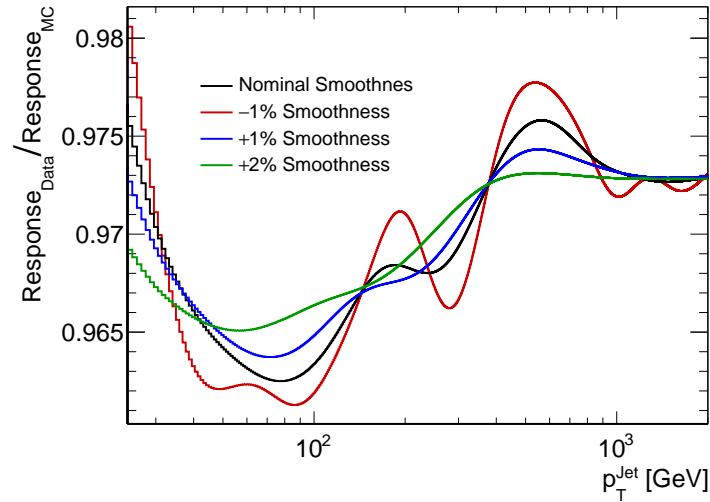


Figure 6.12: Smoothing variations of the absolute in-situ calibration curve compared to the nominal choice. Here “smoothness” refers to the mean curvature of the histograms.

The J75 is again re-calibrated according to these smoothing variations and the rederived search phase results on the  $m_{jj}$  spectra are shown in Figure 6.13. It can be seen that every smoothing variation has a highly significant impact on the magnitude of the excess. Compared to the nominal smoothness, a variation with -1% smoothness<sup>1</sup> strongly enhances the excess, while a +1% smoothness variation significantly decreases it. The +1% smoothness variation corresponds to a BH  $p$ -value of 0.31 which is far from the discovery threshold of 0.01. The excess becomes even less significant in the +2% smoothness variation with a BH  $p$ -value of 0.44. The findings confirm that a non-smoothness in the absolute in-situ calibration curve is responsible for the excess, and further show that the TLA background estimation and search phase procedure is sensitive towards variations in the smoothing procedure.

<sup>1</sup>Here, “smoothness” refers to the mean curvature of the in-situ calibration curve.

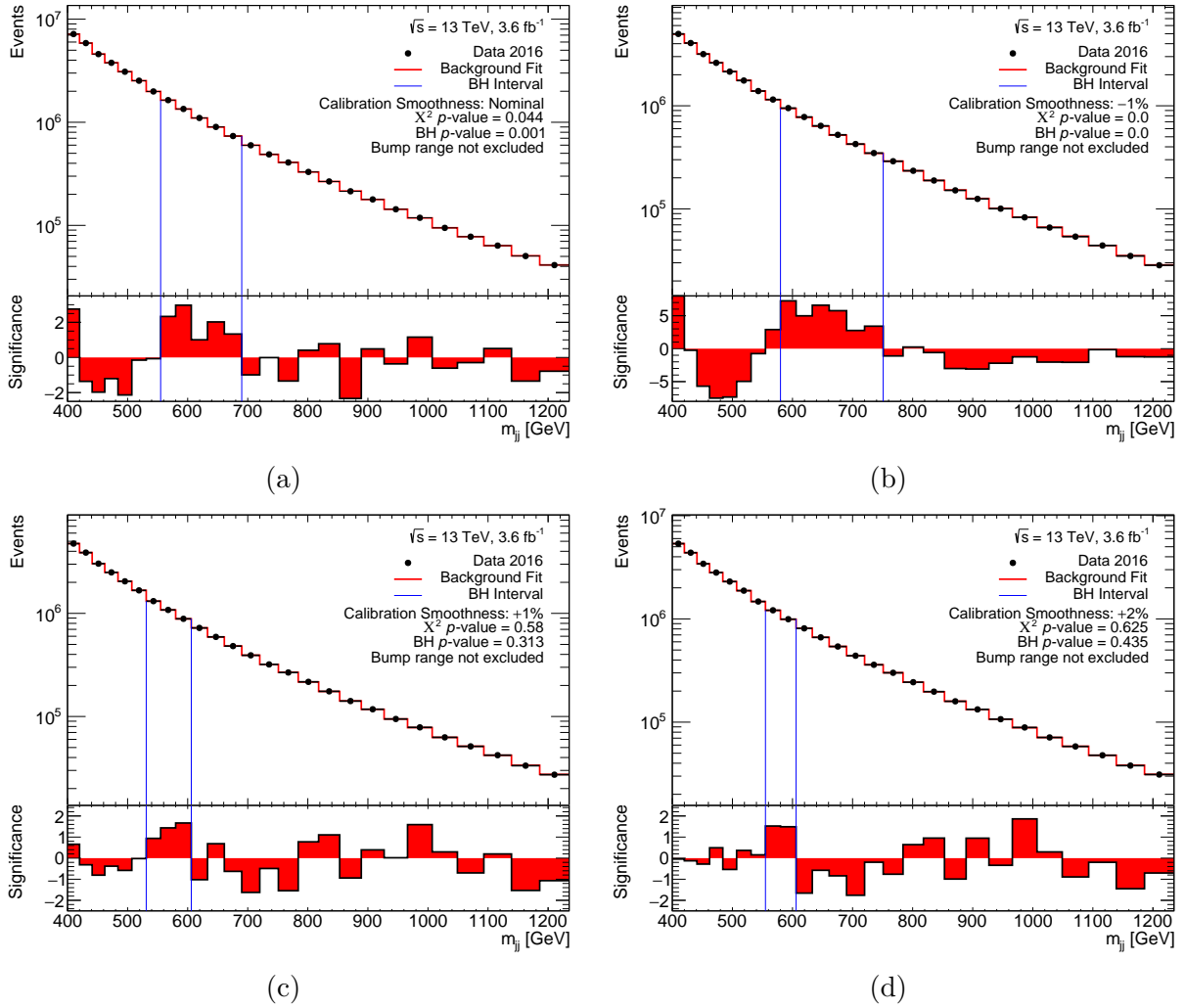


Figure 6.13: Search phase result on the smoothing variations of the absolute in-situ calibration curve and the nominal choice. Compared to the nominal smoothing in (a), (b) shows a 1% less smooth variation, (c) a 1% smoother variation and (d) a 2% smoother variation.

### 6.8.2 Validation of Calibration Smoothness on MC

Given the sensitivity of the background estimation on the smoothness of the calibration, the alternative absolute in-situ calibration based on a polynomial fit needs to be validated on a smooth spectrum to ensure that it does not introduce any excesses in a similar fashion as it is the case for the nominal absolute in-situ calibration. To do this, NLOJET++ samples are produced where each jet is subjected to a  $p_T$  dependent calibration factor corresponding to the nominal or alternative absolute in-situ calibration. Data-like  $m_{jj}$  spectra are created from these samples with the selection requirements of the  $|y^*| < 0.3$  and  $|y^*| < 0.6$  signal regions and the resulting spectra are fitted using SWiFt within the

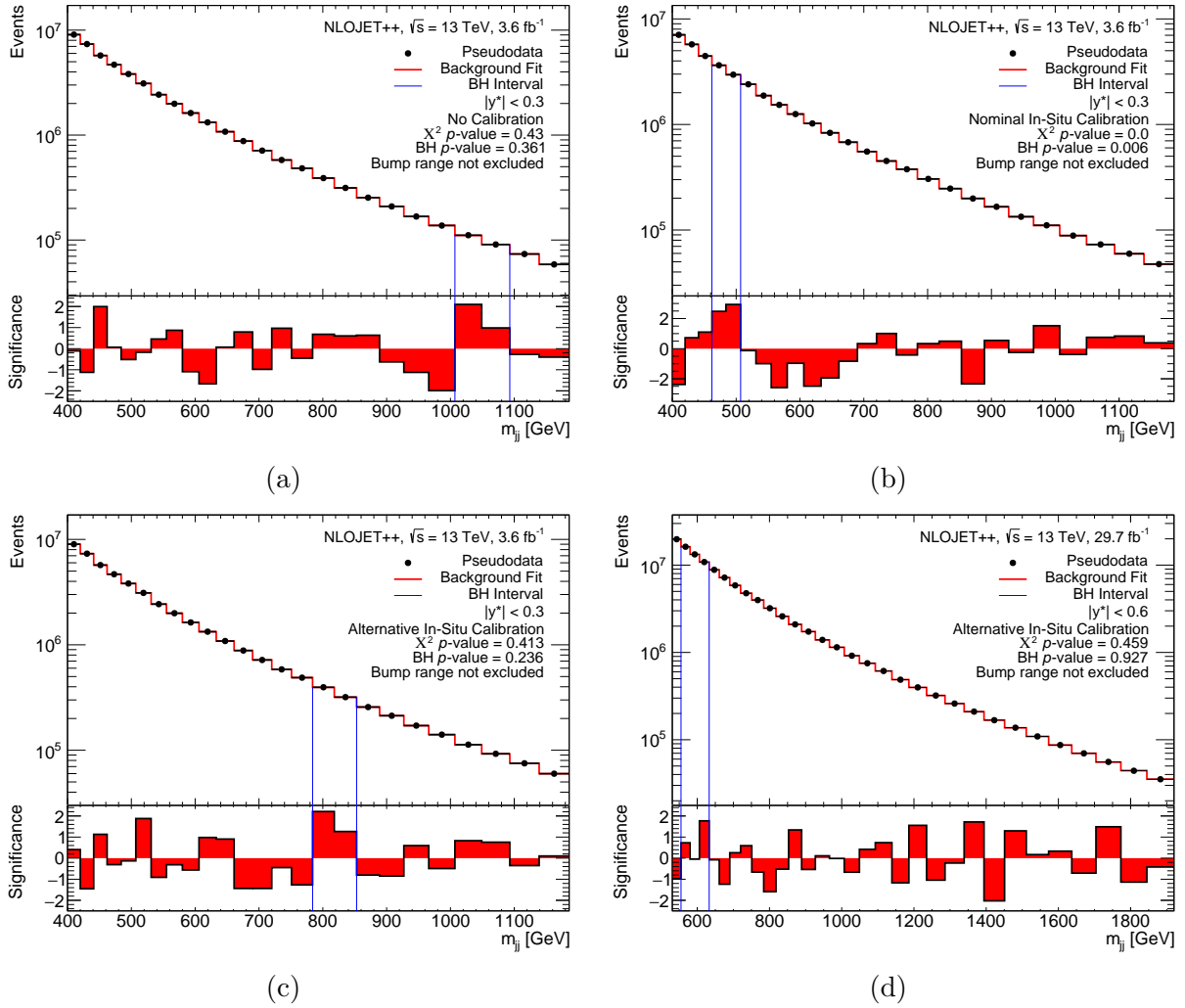


Figure 6.14: Search phase results for the NLOJET++  $m_{jj}$  spectrum with  $|y^*| < 0.3$  scaled to  $3.6\text{fb}^{-1}$  (a) without any calibration factors applied, (b) with the nominal absolute in-situ calibration factors applied and (c) with the alternative absolute in-situ calibration factors applied. In addition, the search phase results for the  $|y^*| < 0.6$  signal region, with the  $m_{jj}$  spectrum scaled to  $29.7\text{fb}^{-1}$  is shown in (d) with the alternative absolute in-situ calibration factors were applied as well.

search phase procedure. Figure 6.14 shows the search phase results for the NLOJET++  $m_{jj}$  spectrum with  $|y^*| < 0.3$  scaled to  $3.6\text{fb}^{-1}$  (a) without any calibration factors applied, (b) with the nominal absolute in-situ calibration factors applied and (c) with the alternative absolute in-situ calibration factors applied. In addition, the search phase results for the  $|y^*| < 0.6$  signal region, with the  $m_{jj}$  spectrum scaled to  $29.7\text{fb}^{-1}$  is shown in (d), where the alternative absolute in-situ calibration factors were applied as well. A comparison of (a) and (b) shows the introduction of a significant excess due to application of the

nominal absolute in-situ calibration factors, thus demonstrating the validity of this check in general. In (c) and (d) no significant excesses are visible which demonstrates that the alternative absolute in-situ calibration factors do not introduce fluctuations of sizes larger than the statistical data-like fluctuations of the sample. This conclusion can be made for the statistical power and event selection criteria of the J75  $|y^*| < 0.3$  (c) and J100  $|y^*| < 0.6$  (d) signal regions.

### 6.8.3 Validation of Search Phase Procedure with Systematic Uncertainties

Another procedure to take the dependence of the background estimate on the smoothness of the calibration into account is to incorporate systematic uncertainties on the JES within the search phase in order to prevent false discoveries due to potential calibration-induced structures. This procedure (outlined in Chapter 6.3.4) can be validated by signal injections on a background sample and the JES uncertainty templates and studying the effects on the search phase test statistics. As background sample the appropriately calibrated dataset from the J75  $|y^*| < 0.3$  signal region is used, which does not contain significant excesses as it is shown in Chapters 6.8.1 and 7.1. A Gaussian signal of 5% relative width is injected at the 620 GeV masspoint and scaled to lie above the discovery threshold for the case that no systematic uncertainties are applied. For illustration, the search phase result in this scenario is shown in Figure 6.15 together with the distribution of the BH and  $\chi^2$  test statistics of the pseudo-experiments compared to the data.

The search phase procedure is repeated with different cases of applied systematic uncertainties and their results are compared in terms of the distribution of the BH and  $\chi^2$  test statistics of the pseudo-experiments in Figure 6.16.

In the first case (Figure 6.16(a,b)) the same signal is injected in the spectra of the templates associated to all grouped JES uncertainty variations. This mimics the case of a real signal which is therefore also present in each JES uncertainty variation template with the same magnitude. The second case (Figure 6.16(c,d)) mimics the scenario where the injected signal corresponds to a calibration-induced excess and is accounted for by a single group of JES uncertainty variations. In this case the JES uncertainty variation should already contain an excess of similar size as the calibration-induced excess. The mass spectrum template corresponding to this JES uncertainty variation then contains contributions from the calibration-induced excess and the intrinsic uncertainty connected to it. The  $1\sigma$  uncertainty corresponding to the calibration-induced excess is assumed to be of the size of the injected signal. Therefore, to mimic this scenario, the signal injected in the mass spectrum of one group of JES uncertainty variations is scaled by  $(1 + \sigma_{\text{var}})$ , where  $\sigma_{\text{var}}$  is the magnitude of the variation.

Comparing the effect on the BH test statistic it can be seen that applying systematic uncertainties sizably reduces the significance of a present excess. This is also the case where a real signal excess is mimicked, and therefore the sensitivity of the search phase procedure with systematics is slightly reduced compared to the procedure with statistical

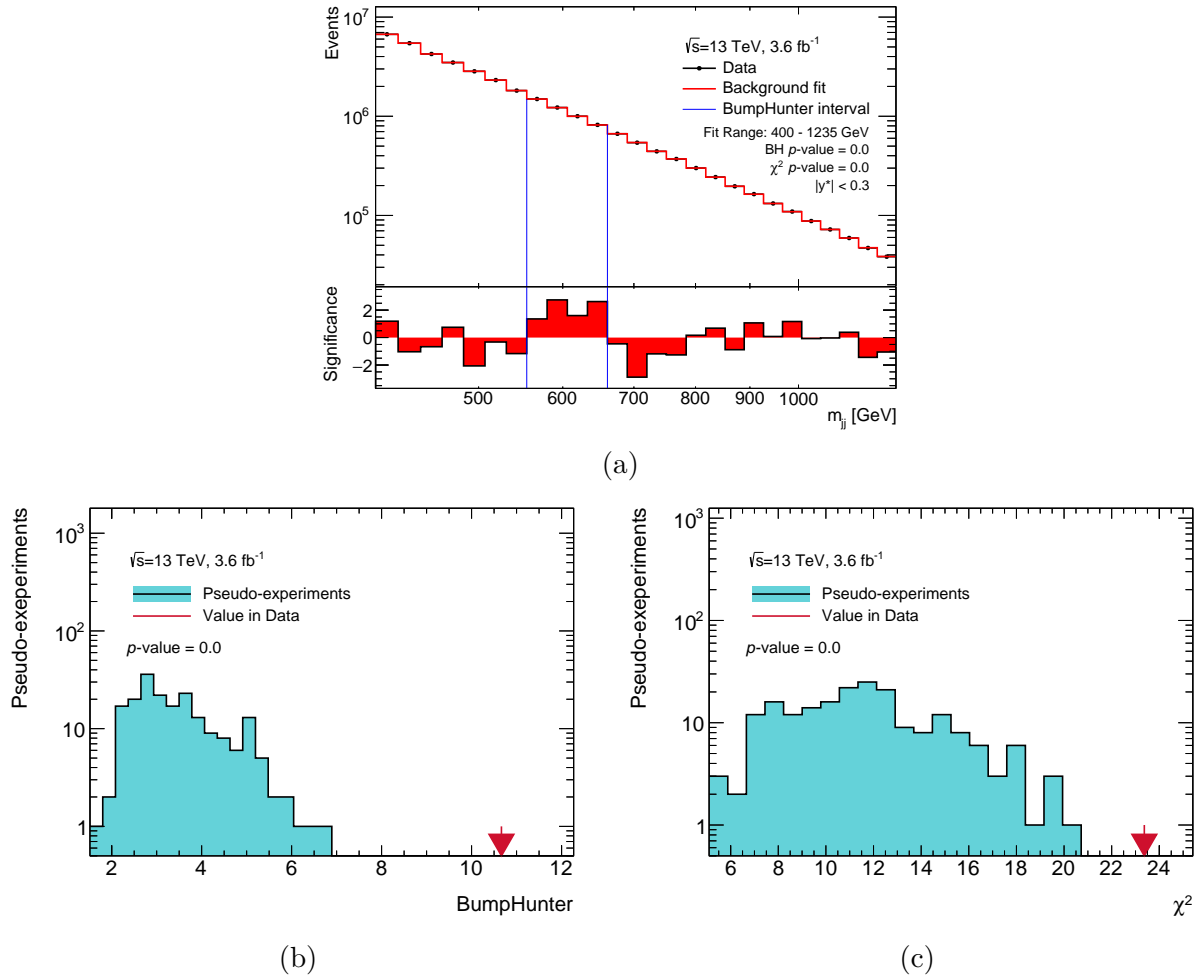


Figure 6.15: Search phase results for a 5% Gaussian width signal injected at the 620 GeV mass point on the dataset of the J75  $|y^*| < 0.3$  signal region (a). The signal was scaled to lie above the discovery threshold of the search phase without systematic uncertainties. The distribution of the BH and  $\chi^2$  test statistics of the pseudo-experiments compared to the data is shown in (b) and (c).

uncertainties only. For example, the discovery cross-section for a 5% Gaussian signal injected at 620 GeV amounts to 1.94 pb if no systematic uncertainties are applied. It increases to 3.6 pb under the inclusion of systematic uncertainties. The reduced sensitivity is considered acceptable. In the case of a calibration-induced excess, the significance of the excess is reduced by a large fraction. This validates the search phase uncertainty procedure as a reliable method to prevent false discoveries due to calibration-induced structures.

The same comparisons can also be made for the  $\chi^2$  test statistic, where the effect of systematic uncertainties is more significant than for the BH test statistic because the overall shape is affected by the JES variations.

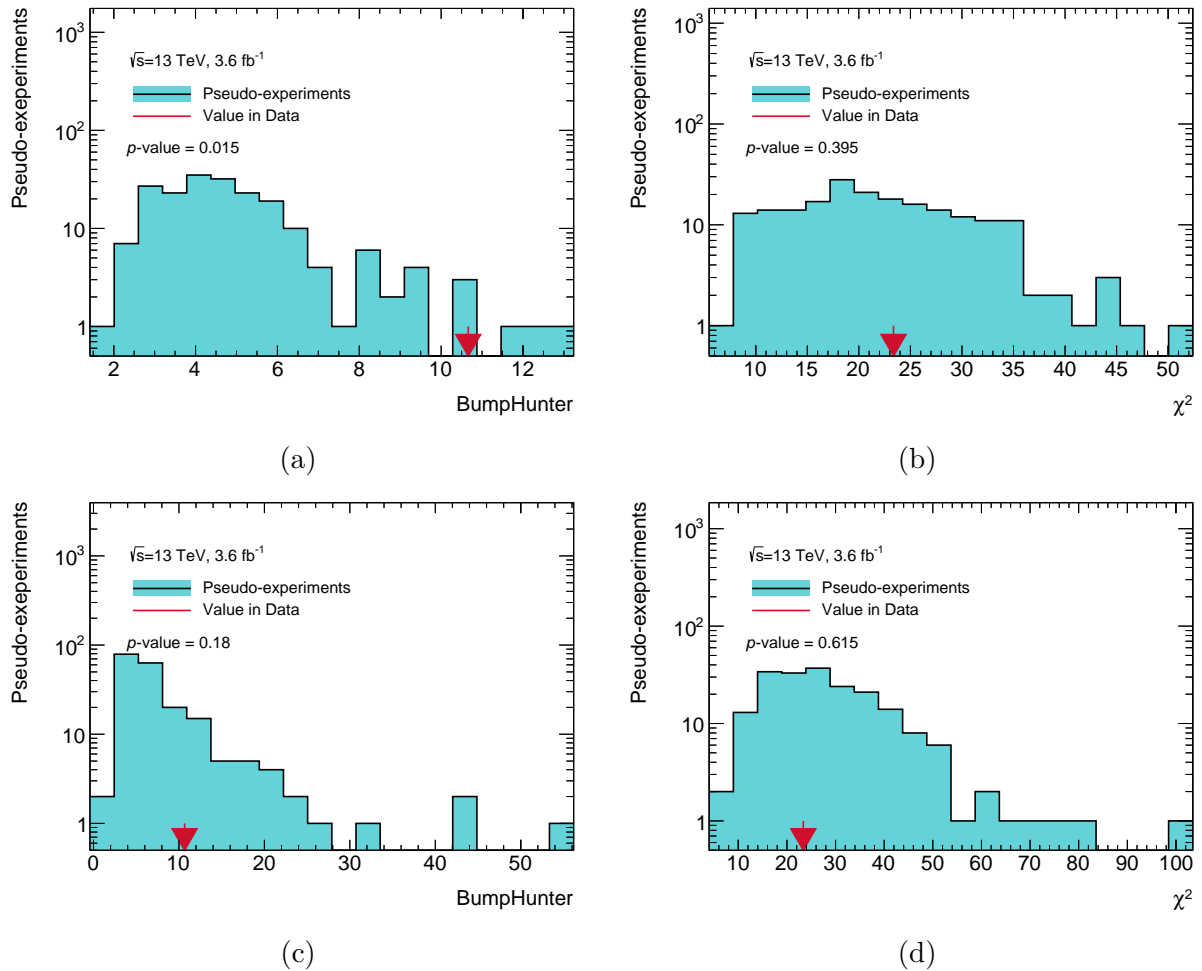


Figure 6.16: Distribution of the BH and  $\chi^2$  test statistics of the pseudo-experiments within the search phase procedure on the dataset of the J75  $|y^*| < 0.3$  signal region with a 5% Gaussian width signal injected at the 620 GeV mass point for the cases (a,b) with the same signal injected on the JES uncertainty variation templates, (c,d) with the same signal injected on the JES uncertainty variation templates except for one variation where the signal magnitude depends on the variation.



# Chapter 7

## TLA Search Results in 13 TeV Data

### 7.1 The J75 data

The search phase result on the mass distribution of the J75  $|y^*| < 0.3$  signal region is shown in Figure 7.1(a).

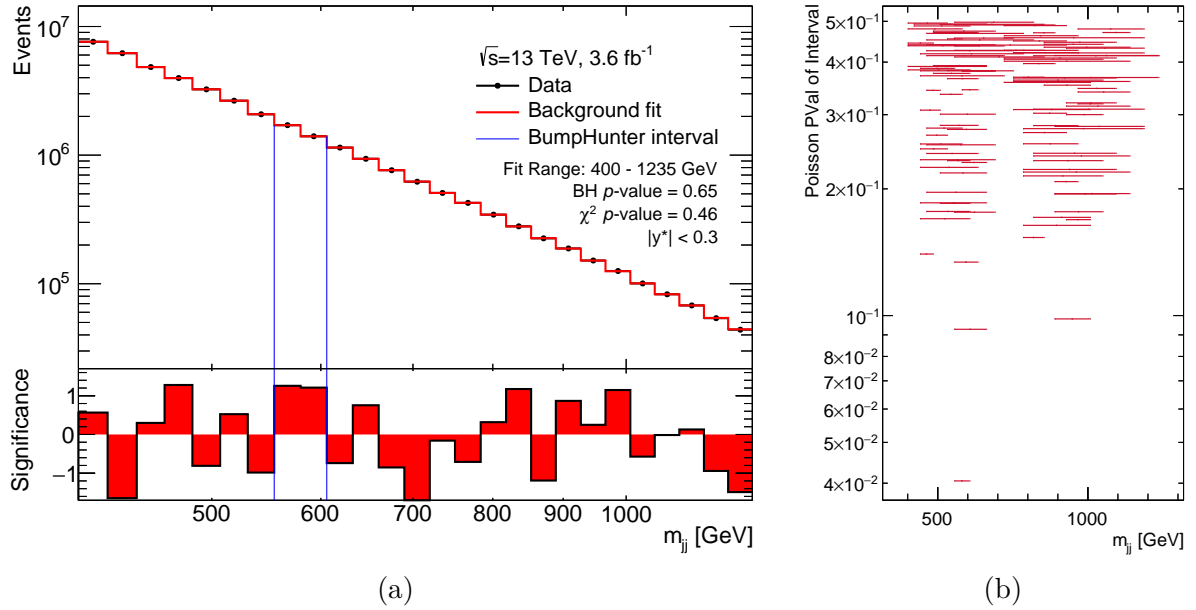


Figure 7.1: Search phase result in the J75  $|y^*| < 0.3$  signal region corresponding to an integrated luminosity of  $3.6 \text{ fb}^{-1}$ (a) and distribution of Poisson probabilities associated to each possible BH interval on the data with respect to the background estimate (b).

The background estimation is obtained from the 4PARAM fit function using the nominal SWiFt window halfwidth of 13 bins in the fit range of 400 – 1235 GeV. The agreement between the fit and the data is quantified to  $\chi^2 = 13.07$ . Figure 7.1(b) shows furthermore the distribution of Poisson probabilities associated to each possible BH interval on the

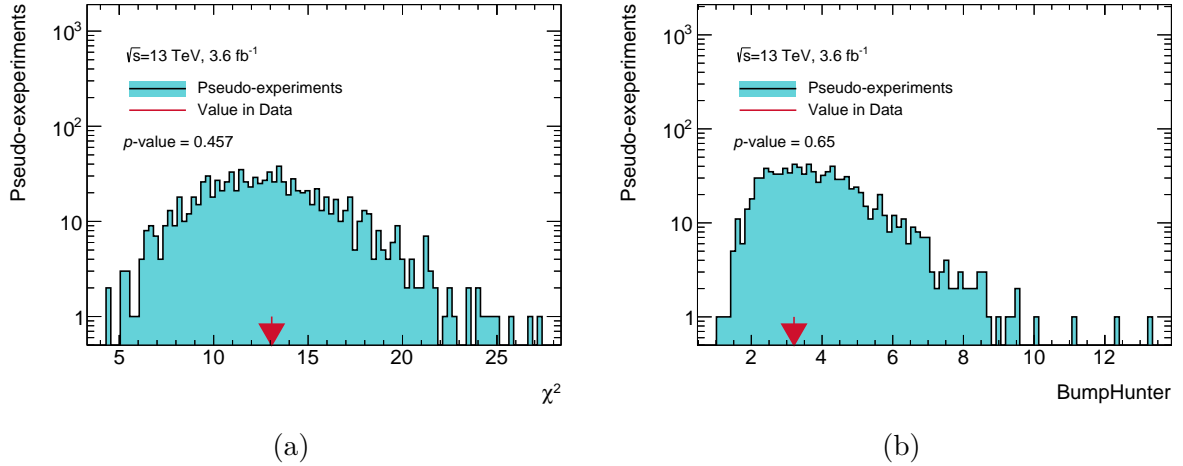


Figure 7.2: Distribution of the (a)  $\chi^2$  and (b) BH test statistics of the pseudo-experiments in comparison to the test statistic of the J75 data (red arrow), both with respect to the background estimate. The respective  $p$ -value is the fraction of pseudo-experiments with a larger test statistic than the value given by the data.

data. The smallest Poisson probability  $t_{\min} = 0.04$  is given within the interval 555 – 606 GeV. Its negative logarithm indicates the BH test statistic of the data  $t_0 = 3.2$ . The distribution of the test statistics of the pseudo-experiments by which the  $\chi^2$  and BH  $p$ -values are determined is shown in Figure 7.2. Each  $p$ -value is given by the fraction of pseudo-experiments with a larger  $\chi^2$  and BH test statistic than the test statistic given by the data (indicated by the red arrow). The  $\chi^2$   $p$ -value of 0.46 demonstrates a good agreement between background estimate and data. The probability of encountering an excess due to a background fluctuation at least as significant as the largest excess observed in data is 0.65 as quantified by the BH  $p$ -value.

## 7.2 The J100 data

The search phase result on the mass distribution of the J100  $|y^*| < 0.6$  signal region is shown in Figure 7.3(a).

After following the unblinding procedure outlined in Chapter 6.7, the background estimate is obtained from the 5PARAM fit function using a reduced SWiFt window halfwidth of 9 bins in the fit range of 541 – 2079 GeV. The agreement between the fit and the data is quantified to  $\chi^2 = 20.98$ . Figure 7.3(b) shows furthermore the distribution of Poisson probabilities associated to each possible BH interval on the data. The smallest Poisson probability  $t_{\min} = 0.013$  is given within the interval 889 – 1007 GeV. Its negative logarithm indicates the BH test statistic of the data  $t_0 = 4.35$ . The distribution of the test statistics of the pseudo-experiments by which the  $\chi^2$  and BH  $p$ -values are determined is shown in Figure 7.4. Each  $p$ -value is given by the fraction of pseudo-experiments with a larger  $\chi^2$

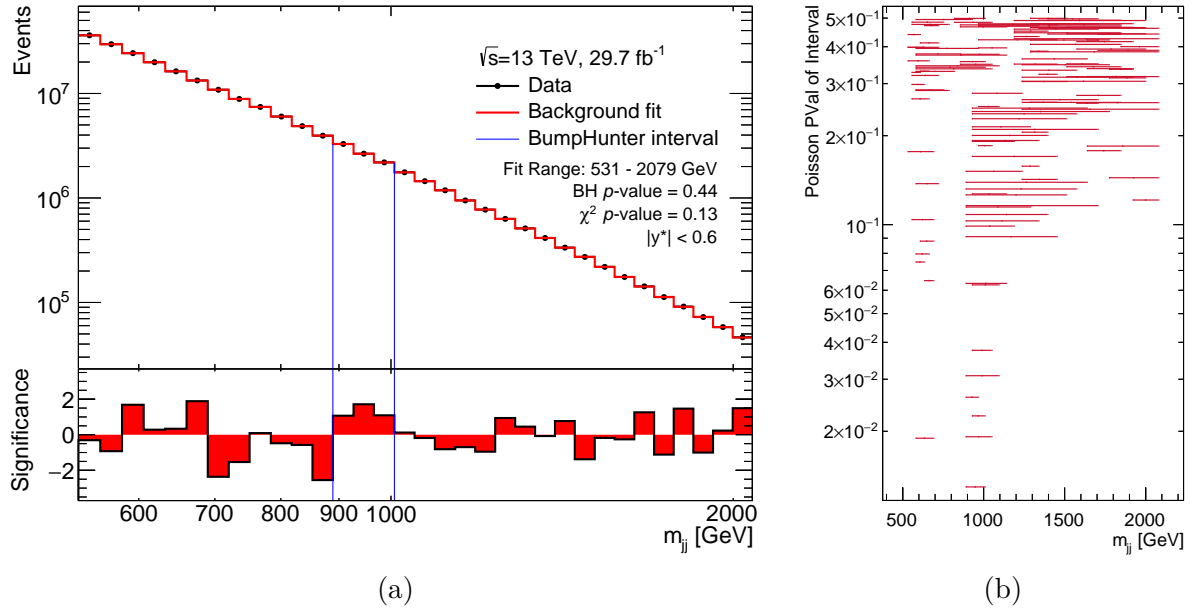


Figure 7.3: Search phase result in the J100  $|y^*| < 0.6$  signal region corresponding to an integrated luminosity of  $29.7 \text{ fb}^{-1}$  (a) and the distribution of Poisson probabilities associated to each possible BH interval on the data with respect to the background estimate (b).

and BH test statistic than the test statistic given by the data (indicated by the red arrow). The  $\chi^2$   $p$ -value of 0.13 demonstrates an acceptable agreement between background estimate and data. The probability of encountering an excess due to a background fluctuation at least as significant as the largest excess observed in data is 0.44 as quantified by the BH  $p$ -value. This corresponds to a significance of  $0.16 \sigma$ .

### 7.3 Discussion

For both the J75 and the J100 signal regions a background estimate was successfully obtained. Since the J75 search phase result was obtained after a previous result was recalibrated using an improved calibration, it cannot be viewed as the result of a fully blinded analysis. For J100, the search phase result stems from a blinded analysis.

No significant excesses were found in the targeted mass range from 400 – 2000 GeV in either signal region. This allows to set exclusion limits on the parameterspace of a leptophobic  $Z'$  as well as on generic Gaussian resonances. With respect to the 2015 TLA iteration the limits are expected to improve - not only due to the larger dataset, but also due to the improved resolution and smaller JES uncertainties. Also a 500 GeV-wide gap of unexplored parameter space between the limits obtained in the previous TLA iteration and the high-mass dijet analysis [134] is expected to be successfully covered.

The background estimate in the J75 region was obtained using the nominal SWiFt window halfwidth. Within the higher statistical precision of the J100 region the window halfwidth

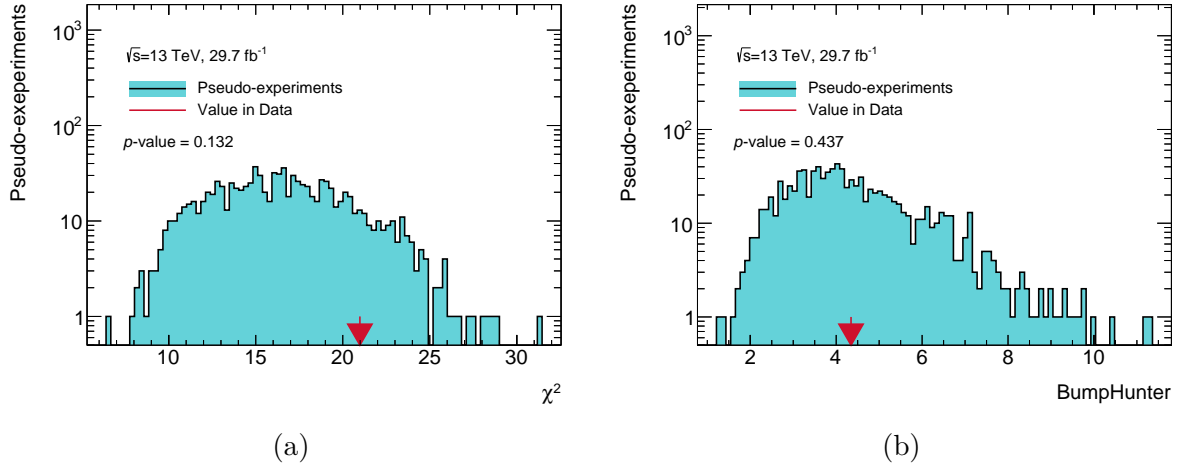


Figure 7.4: Distribution of the (a)  $\chi^2$  and (b) BH test statistics of the pseudo-experiments in comparison to the test statistic of the J100 data (red arrow), both with respect to the background estimate. The respective  $p$ -value is the fraction of pseudo-experiments with a larger test statistic than the value given by the data.

had to be decreased in order to yield an acceptable  $\chi^2$   $p$ -value. The resulting loss in sensitivity and robustness with respect to signals, especially towards the lower edge of the mass range, is accepted. This further suggests that the smoothness of the calibration as well as the background estimation strategy are still to be improved, especially as the statistical precision continues to increase for the next iterations of the TLA.

The TLA jet calibration could be improved by deriving the calibration factors solely from HLT jets. This would render the trigger-to-offline scale factors unnecessary and thereby exclude one potential source of calibration unsmoothness.

The TLA background estimation strategy could be improved by using a background estimation method which does not rely on an analytic function to describe the QCD background. This could be realized for example by functionless fitting methods that are constrained by monotony requirements on the fit and its derivatives.

# Chapter 8

## Summary

Searches for resonances in the dijet invariant mass spectrum provide a mode-independent approach to search for physics beyond the Standard Model at the Large Hadron Collider. This work presents the dijet Trigger-Object Level Analysis (TLA), which is a dijet resonance search in the low mass spectrum. This analysis uses  $29.7 \text{ fb}^{-1}$  of 13 TeV data, taken in 2016 by the ATLAS detector and targets the invariant mass range between 400 and 2000 GeV. For conventional “offline” searches this mass range is statistically limited due to the bandwidth capacity of the data acquisition system. The TLA approach circumvents this limitation by recording only calorimeter jets which are reconstructed “online” within the High Level Trigger (HLT). This allows for a larger statistical precision but at the same time poses challenges on the jet energy calibration procedure. Based on calorimeter information only, the TLA jet energy calibration should be smooth and reach a similar performance in terms of resolution and uncertainties as the offline calibration which uses the full detector information. In addition, the statistical precision of the data in conjunction with the calorimeter-based calibration adds challenges to the background estimation. Monte Carlo simulations can not be used due to large systematic uncertainties and simple functional forms can not describe the full invariant mass spectrum.

The TLA jet energy calibration procedure is based on the same procedure for offline jets but is modified when the offline jet calibration procedure is not applicable, i.e. when full detector information is required. This is for example the case for the Global Sequential Correction (GSC), which corrects the jet energy as function of jet property variables from the full detector. The TLA employs a dedicated GSC using calorimeter-based jet property variables, thereby reducing the jet energy resolution (JER) by  $\sim 20\%$ . This is comparable to the  $\sim 25\%$  improvement achieved by the offline GSC. The GSC further reduces flavor-related calibration uncertainties, which would become the dominant components of the jet energy scale (JES) uncertainty without the GSC applied. Together with a dedicated determination of the flavor composition of the analysis sample, the total JES uncertainty is thereby reduced by around 50%. The dominant source of the JES uncertainty arises from residual differences to offline jets which are accounted for by dedicated trigger-to-offline scale factors. Compared to offline, the overall JES uncertainty for the TLA remains only 30% larger.

The large statistical precision of the data sample, make the TLA background estimate susceptible to non-smoothness in the calibration functions. In this analysis, the in-situ calibration, which corrects for differences in JES between data and Monte Carlo, is not smooth enough. Therefore, an alternative absolute in-situ calibration, reflecting the smoothness of the detector response, is validated and employed. The full TLA calibration procedure is validated using in-situ techniques demonstrating a good agreement with respect to the offline JES within 1% throughout the TLA signal regions.

To provide a reliable background estimation, a sliding window fit (SWiFt) is employed. The SWiFt parameters such as the window width are optimized in terms of sensitivity and robustness towards potential signals. To account for the dependence of the background estimation on the calibration smoothness, a method to apply uncorrelated JES uncertainties in the search for resonances is introduced and validated. The SWiFt method is successfully employed to obtain a background estimate in the targeted search range. No significant excesses are found within the TLA signal regions.

For the future, as the statistical precision continues to increase, the calibration and background estimation procedures need further improvement. The TLA in particular is sensitive towards calibration non-smoothness, but also other resonance searches with large data samples, including offline searches, could eventually be affected. Here, a comprehensive discussion across other resonance searches and calibration groups is needed to find a consistent calibration strategy and treatment of uncertainties.

The TLA jet calibration procedure can be improved by deriving the calibration factors solely from HLT jets. This renders the trigger-to-offline scale factors unnecessary and thereby excludes one potential source of calibration unsmoothness and uncertainty. A second improvement is to add tracking information to the recorded HLT jets. This can be done in two ways. One way is to include the tracking information which is used by the  $b$ -tagging algorithms at the HLT. Another way is to employ tracking information from the ATLAS Fast Tracker [135], which is planned to be operational in 2018. Track based information would provide for the inclusion of reference objects and track-based jet property variables for the GSC as well as methods for pile-up rejection.

The TLA background estimation can be improved by using a method which does not rely on analytic functions to describe the QCD background. This can be realized for example by functionless fitting methods that are constrained by monotony requirements on the fit and its derivatives.

Apart from these improvements, the TLA approach can be extended towards other trigger-limited signatures like 4-jet or  $\gamma$ -jet topologies.

# Appendix A

## TLA Jet Reconstruction and Calibration

### A.1 Jet Quality Selection

A jet quality check is employed to veto events containing jets stemming from non-collision backgrounds such as cosmic rays, calorimeter noise or beam induced backgrounds (i.e. due to upstream proton losses). It is based on the procedure for offline jets with the *BadLoose* criteria defined in [136], where a jet is rejected if at least one of the following conditions is met:

- $f_{\text{HEC}} > 0.5$  and  $|f_{\text{Q}}^{\text{HEC}}| > 0.5$  and  $\langle Q \rangle > 0.8$ ,

where  $f_{\text{HEC}}$  is the jet energy fraction deposited in the HEC calorimeter,  $f_{\text{Q}}^{\text{HEC}}$  is the jet energy fraction deposited in the HEC calorimeter with poor signal shape quality and  $\langle Q \rangle$  is the pulse quality in the liquid argon based calorimeters.

- $|E_{\text{neg}}| > 60$  GeV,

where  $|E_{\text{neg}}|$  is the energy sum of all cells with negative energy.

- $f_{\text{EM}} > 0.95$  and  $|f_{\text{Q}}^{\text{LAr}}| > 0.8$  and  $\langle Q \rangle > 0.8$  and  $|\eta| < 2.8$ ,

where  $f_{\text{EM}}$  is the jet energy fraction deposited in the EM calorimeter and  $|f_{\text{Q}}^{\text{LAr}}|$  is the jet energy fraction deposited in the liquid argon based calorimeters with poor signal shape quality.

- $f_{\text{max}} > 0.99$  and  $|\eta| < 2$ ,

where  $f_{\text{max}}$  is the maximum jet energy fraction deposited in any of the calorimeter layers.

- $f_{\text{EM}} < 0.05$  and  $f_{\text{ch}} < 0.05$  and  $|\eta| < 2$ ,

where  $f_{\text{ch}}$  is the charged fraction, defined as the ratio of the  $p_T$  sum of the tracks associated to the jet to the total  $p_T$  of the jet.

- $f_{\text{EM}} < 0.05$  and  $|\eta| \geq 2$

Except for the charged fraction  $f_{\text{ch}}$  which is a track based variable, all cleaning variables are available in the datascouting stream and are used likewise in the TLA. If at least one of the first three leading jets is not passing the cleaning criteria, the event is rejected.

## A.2 Modelling of GSC Jet Property Variables

The MC based modelling of the calorimeter based GSC jet property variables employed by the TLA is presented in Figure A.1 in different  $\mu$  environments and in Figure A.2 in different  $N_{PV}$  environments in comparison to data. The considered jets have a  $p_T$  close to the subleading jet  $p_T$  cut of the TLA. An additional comparison for  $N_{PV}$  close to the leading jet  $p_T$  cut is given in Figure A.3.

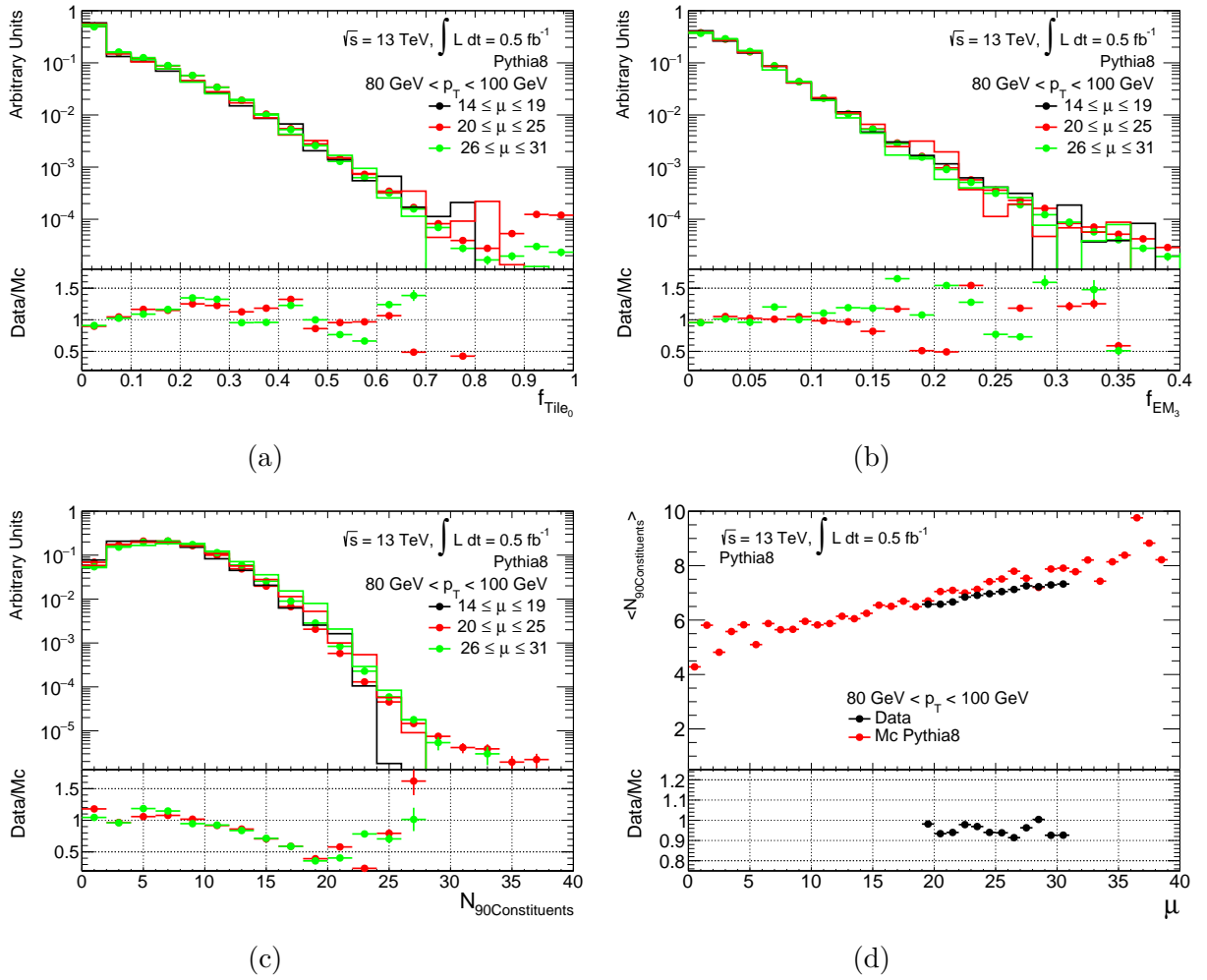


Figure A.1: Shape comparison of the (a)  $f_{\text{Tile}_0}$ , (b)  $f_{EM_3}$  and (c)  $N_{90\text{Constituents}}$  variables between data and MC for jets with  $80\text{GeV} < p_T < 100\text{GeV}$  and different  $\mu$  environments. The dotted datapoints represent data and the lines represent MC. A comparison of the arithmetic mean of the  $N_{\text{Constituents}}$  variable as a function of  $\mu$  between data and MC is shown in (d).

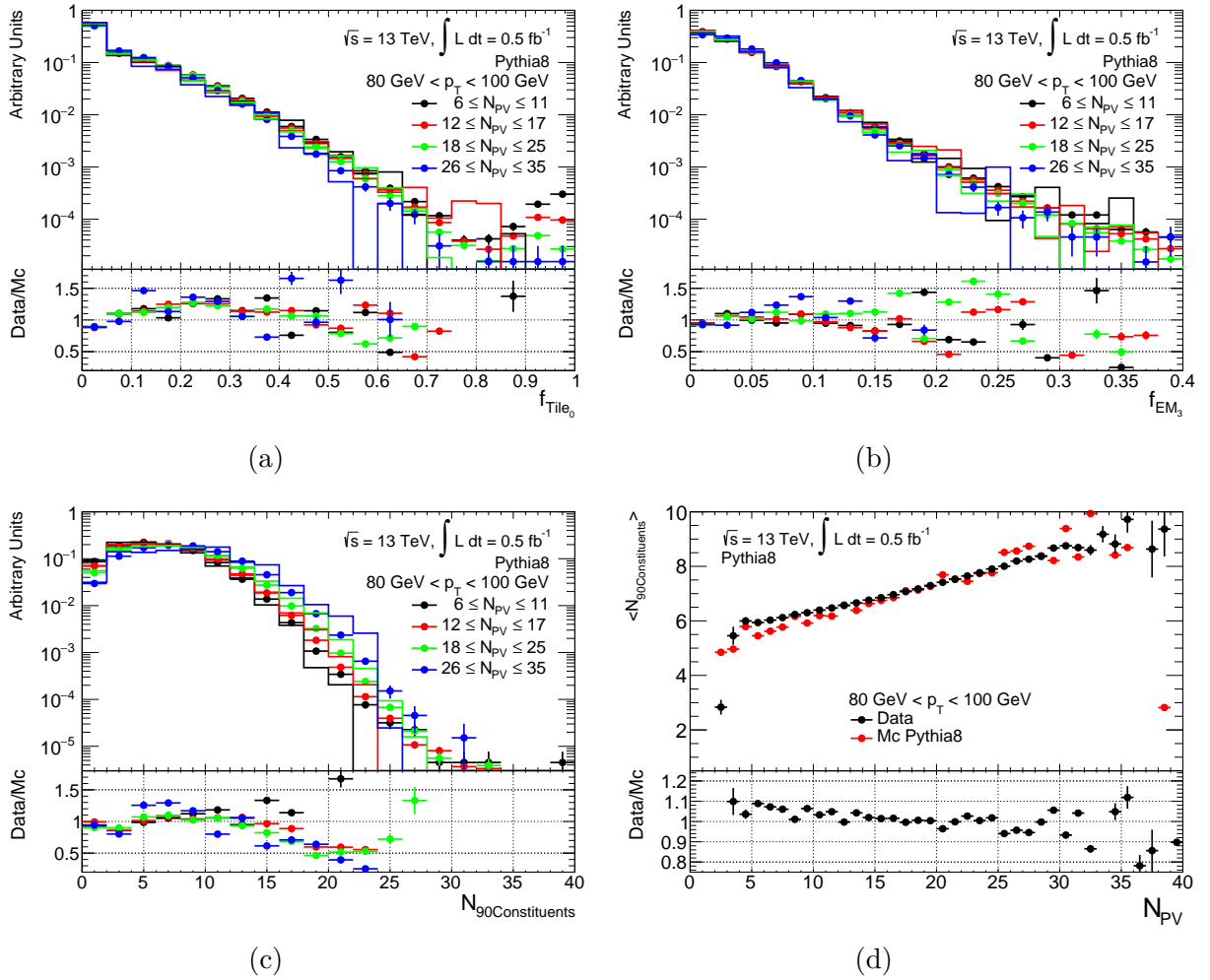


Figure A.2: Shape comparison of the (a)  $f_{\text{Tile}_0}$ , (b)  $f_{\text{EM}_3}$  and (c)  $N_{90\text{Constituents}}$  variables between data and MC for jets with  $80 \text{ GeV} < p_T < 100 \text{ GeV}$  and different  $N_{\text{PV}}$  environments. The dotted datapoints represent data and the lines represent MC. A comparison of the arithmetic mean of the  $N_{\text{Constituents}}$  variable as a function of  $N_{\text{PV}}$  between data and MC is shown in (d).

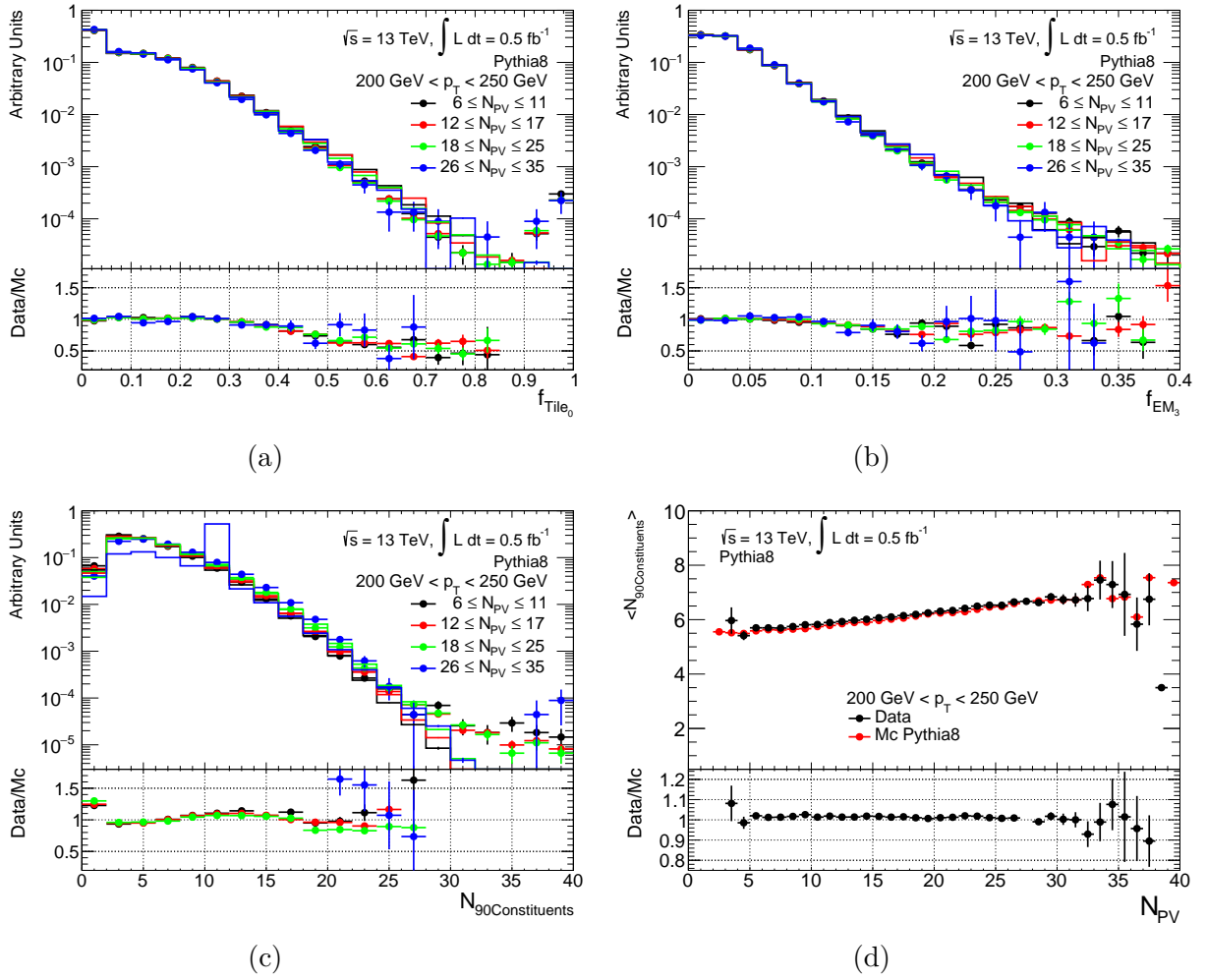


Figure A.3: Shape comparison of the (a)  $f_{\text{Tile}_0}$ , (b)  $f_{EM_3}$  and (c)  $N_{90\text{Constituents}}$  variables between data and MC for jets with  $200\text{GeV} < p_T < 250\text{GeV}$  and different  $N_{PV}$  environments. The dotted datapoints represent data and the lines represent MC. A comparison of the arithmetic mean of the  $N_{\text{Constituents}}$  variable as a function of  $N_{PV}$  between data and MC is shown in (d).



# Bibliography

- [1] M. Thomson, *Modern Particle Physics*. Cambridge University Press, 2013.
- [2] M. E. Peskin and D. V. Schroeder, *An introduction to quantum field theory*. Westview, 1995.
- [3] C. P. Burgess and G. D. Moore, *The standard model: A primer*. Cambridge University Press, 2007.
- [4] R. M. Harris and K. Kousouris, *Searches for Dijet Resonances at Hadron Colliders*, Int. J. Mod. Phys. **A26** (2011) 5005–5055.
- [5] R. K. Ellis, W. J. Stirling, and B. R. Webber, *QCD and Collider Physics*. Cambridge Univ. Press, 2003.
- [6] R. Devenish and A. Cooper-Sarkar, *Deep Inelastic Scattering*. Oxford University Press, 2004.
- [7] P. Ramond, *Journeys Beyond the Standard Model*. Perseus Books, 1999.
- [8] G. Dissertori, I. G. Knowles, and M. Schmelling, *Quantum chromodynamics: high energy experiments and theory*. Oxford Univ. Press, 2002.
- [9] CERN Summer Student Webfest, *Go on a particle quest at the first CERN hackfest*, 2012. <https://sciencenode.org/spotlight/go-particle-quest-first-cern-hackfest.php>.
- [10] LHCb Collaboration, *Observation of  $J/\psi p$  Resonances Consistent with Pentaquark States in  $\Lambda_b^0 \rightarrow J/\psi K^- p$  Decays*, Phys. Rev. Lett. **115** (2015) 072001.
- [11] LHCb Collaboration, *Observation of the resonant character of the  $Z(4430)^-$  state*, Phys. Rev. Lett. **112** (2014) 222002.
- [12] C. T. Sachrajda, *Perturbative QCD and Hard Scattering Processes*, Phys. Scripta **19** (1979) 85.
- [13] T. Kinoshita, *Mass Singularities of Feynman Amplitudes*, Journal of Mathematical Physics **3** (1962) 650–677.

- [14] T. D. Lee and M. Nauenberg, *Degenerate Systems and Mass Singularities*, Phys. Rev. **133** (1964) B1549–B1562.
- [15] R. Akhoury, M. G. Sotiropoulos, and V. I. Zakharov, *Kinoshita-Lee-Nauenberg theorem and soft radiation in gauge theories: Abelian case*, Phys. Rev. D **56** (1997) 377–387.
- [16] ATLAS Collaboration, *Standard Model Public Results*, 2017. <https://twiki.cern.ch/twiki/bin/view/AtlasPublic/StandardModelPublicResults>.
- [17] A. Shomer, *A pedagogical explanation for the non-renormalizability of gravity*, ArXiv e-prints (2007), arXiv:0709.3555 [hep-th].
- [18] L. Canetti, M. Drewes, and M. Shaposhnikov, *Matter and antimatter in the universe*, New J. Phys. **14** no. 9, (2012) 095012.
- [19] S. M. Bilenky, *Neutrino oscillations: brief history and present status*, ArXiv e-prints (2014), arXiv:1408.2864 [hep-ph].
- [20] R. D. Peccei, *The Strong CP problem and axions*, Lect. Notes Phys. **741** (2008) 3–17.
- [21] R. J. Hill, *Review of experimental and theoretical status of the proton radius puzzle*, EPJ Web Conf. **137** (2017) 01023.
- [22] J. P. Miller, E. de Rafael, and B. L. Roberts, *Muon ( $g - 2$ ): experiment and theory*, Rep. Prog. Phys. **70** (2007) 795–881.
- [23] E. Corbelli and P. Salucci, *The extended rotation curve and the dark matter halo of M33*, MNRAS **311** (2000) 441–447.
- [24] D. Clowe, A. Gonzalez, and M. Markevitch, *Weak lensing mass reconstruction of the interacting cluster 1E0657-558: Direct evidence for the existence of dark matter*, Astrophys. J. **604** (2004) 596–603.
- [25] M. Markevitch, A. H. Gonzalez, D. Clowe, A. Vikhlinin, L. David, W. Forman, C. Jones, S. Murray, and W. Tucker, *Direct constraints on the dark matter self-interaction cross-section from the merging galaxy cluster 1E0657-56*, Astrophys. J. **606** (2004) 819–824.
- [26] Planck Collaboration, *Planck 2015 results. XIII. Cosmological parameters*, Astron. Astrophys. **594** (2016) A13.
- [27] F. Zwicky, *On the Masses of Nebulae and of Clusters of Nebulae*, Astrophys. J. **86** (1937) 217.

- [28] A. N. Taylor, S. Dye, T. J. Broadhurst, N. Benitez, and E. van Kampen, *Gravitational lens magnification and the mass of abell 1689*, *Astrophys. J.* **501** (1998) 539.
- [29] W. J. Percival, S. Cole, D. J. Eisenstein, R. C. Nichol, J. A. Peacock, A. C. Pope, and A. S. Szalay, *Measuring the Baryon Acoustic Oscillation scale using the Sloan Digital Sky Survey and 2dF Galaxy Redshift Survey*, *MNRAS* **381** no. 3, (2007) 1053–1066.
- [30] J. A. Peacock et al., *A Measurement of the cosmological mass density from clustering in the 2dF Galaxy Redshift Survey*, *Nature* **410** (2001) 169–173.
- [31] C. S. Frenk and S. D. M. White, *Dark matter and cosmic structure*, *Ann. Phys.* **524** (2012) 507–534.
- [32] L. Roszkowski, E. M. Sessolo, and S. Trojanowski, *WIMP dark matter candidates and searches - current issues and future prospects*, [arXiv:1707.06277](https://arxiv.org/abs/1707.06277) [hep-ph].
- [33] G. C. Branco, P. M. Ferreira, L. Lavoura, M. N. Rebelo, M. Sher, and J. P. Silva, *Theory and phenomenology of two-Higgs-doublet models*, *Phys. Rept.* **516** (2012) 1–102.
- [34] M. Schmaltz and D. Tucker-Smith, *Little Higgs Theories*, *Annu. Rev. Nucl. Part. Sci.* **55** (2005) 229–270.
- [35] I. Garcia Garcia, R. Lasenby, and J. March-Russell, *Twin Higgs WIMP Dark Matter*, *Phys. Rev.* **D92** (2015) 055034.
- [36] J. S. Hagelin, G. Kane, and S. Raby, *Perhaps scalar neutrinos are the lightest supersymmetric partners*, *Nucl. Phys. B* **241** (1984) 638 – 652.
- [37] S. P. Martin, *A Supersymmetry primer*, *Adv. Ser. Direct. High Energy Phys.* **18** (1997).
- [38] S. Raby, *Grand Unified Theories*, in *2nd World Summit: Physics Beyond the Standard Model*. 2006. [arXiv:hep-ph/0608183](https://arxiv.org/abs/hep-ph/0608183) [hep-ph].
- [39] M. Schmaltz and D. Tucker-Smith, *Little Higgs review*, *Ann. Rev. Nucl. Part. Sci.* **55** (2005) 229–270.
- [40] H. Nilles, *Supersymmetry, supergravity and particle physics*, *Physics Reports* **110** no. 1, (1984) 1 – 162.
- [41] J. A. Evans and Y. Kats, *LHC coverage of RPV MSSM with light stops*, *Journal of High Energy Physics* **4** (2013) 28.
- [42] W. de Boer, *Grand unified theories and supersymmetry in particle physics and cosmology*, *Prog. Part. Nucl. Phys.* **33** (1994) 201–302.

- [43] D. Peripelitsa, *Sakharov Conditions for Baryogenesis*, November, 2008.
- [44] M. Dittmar, A.-S. Nicollerat, and A. Djouadi, *Z-prime studies at the LHC: An Update*, Phys. Lett. **B583** (2004) 111–120.
- [45] A. De Simone and T. Jacques, *Simplified models vs. effective field theory approaches in dark matter searches*, Eur. Phys. J. C **76** (2016) 367.
- [46] M. Chala, F. Kahlhoefer, M. McCullough, G. Nardini, and K. Schmidt-Hoberg, *Constraining dark sectors with monojets and dijets*, Journal of High Energy Physics **2015** (2015) 89.
- [47] B. Holdom, *Two U(1)'s and  $\epsilon$  charge shifts*, Physics Letters B **166** (1986) 196 – 198.
- [48] E. Dudas, Y. Mambrini, S. Pokorski, and A. Romagnoni, *(In)visible Z-prime and dark matter*, JHEP **08** (2009) 014.
- [49] H. An, X. Ji, and L.-T. Wang, *Light dark matter and Z' dark force at colliders*, Journal of High Energy Physics **2012** no. 7, (2012) 182.
- [50] H. An, R. Huo, and L.-T. Wang, *Searching for low mass dark portal at the LHC*, Physics of the Dark Universe **2** (2013) 50 – 57,  
<http://www.sciencedirect.com/science/article/pii/S221268641300006X>.
- [51] LUX Collaboration, *First Results from the LUX Dark Matter Experiment at the Sanford Underground Research Facility*, Phys. Rev. Lett. **112** (2014) 091303.
- [52] CMS Collaboration, *Search for dark matter, extra dimensions, and unparticles in monojet events in proton-proton collisions at  $\sqrt{s} = 13$  TeV*, Eur. Phys. J. C **75** (2015) 235.
- [53] UA2 Collaboration, *A search for new intermediate vector bosons and excited quarks decaying to two-jets at the CERN  $\bar{p}p$  collider*, Nucl. Phys. B **400** (1993) 3 – 22.
- [54] CDF Collaboration, *Search for new particles decaying into dijets in proton-antiproton collisions at  $\sqrt{s} = 1.96$  TeV*, Phys. Rev. D **79** (2009) 112002.
- [55] CMS Collaboration, *Search for resonances and quantum black holes using dijet mass spectra in proton-proton collisions at  $\sqrt{s} = 8$  TeV*, Phys. Rev. D **91** (2015) 052009.
- [56] ATLAS Collaboration, *Search for new phenomena in the dijet mass distribution using pp collision data at  $\sqrt{s} = 8$  TeV with the ATLAS detector*, Phys. Rev. D **91** (2015) 052007.
- [57] ATLAS Collaboration, *Search for a dijet resonance produced in association with a leptonically decaying W or Z boson with the ATLAS detector at  $\sqrt{s} = 8$  TeV*, ATLAS-CONF-2013-074, 2013.

- [58] L. Evans and P. Bryant, *LHC Machine*, JINST **3** (2008) S08001.
- [59] ATLAS collaboration, *The ATLAS Experiment at the CERN Large Hadron Collider*, JINST **3** (2008) S08003.
- [60] K. Kleinknecht, *Detectors for particle radiation*. Cambridge University Press, 2<sup>nd</sup> ed., 1998.
- [61] C. Leroy and P. Rancoita, *Principles of Radiation Interaction In Matter and Detection*. World Scientific Publishing, 4<sup>th</sup> ed., 2016.
- [62] ATLAS Collaboration, *Luminosity Public Results*, 2017.  
[https://twiki.cern.ch/twiki/bin/view/AtlasPublic/LuminosityPublicResultsRun2#Luminosity\\_summary\\_plots\\_for\\_201](https://twiki.cern.ch/twiki/bin/view/AtlasPublic/LuminosityPublicResultsRun2#Luminosity_summary_plots_for_201).
- [63] Bruschi, M., *Diffraction and Forward Physics in ATLAS: results and perspectives*, EPJ Web of Conferences **90** (2015) 06003.
- [64] CERN PhotoLab, J. Pequenaio, *Computer generated image of the whole ATLAS detector*, 2008. <https://cds.cern.ch/record/1095924>.
- [65] CERN PhotoLab, J. Pequenaio, P. Schaffner, *Computer generated image representing how ATLAS detects particles*, 2013.  
<https://cds.cern.ch/record/1505342>.
- [66] T. Han, *Collider Phenomenology: Basic Knowledge and Techniques*, Physics in D  $\geq 4$  TASI (2006) 407–454.
- [67] CERN PhotoLab, J. Pequenaio, *Computer generated image of the ATLAS inner detector*, 2008. <https://cds.cern.ch/record/1095926>.
- [68] ATLAS Collaboration, G. Aad et al., *The ATLAS Inner Detector commissioning and calibration*, Eur. Phys. J. **C70** (2010) 787–821.
- [69] ATLAS Collaboration, *Study of the material of the ATLAS inner detector for Run 2 of the LHC*, 2017.
- [70] J. P. CERN PhotoLab, *Computer Generated image of the ATLAS calorimeter*, 2008. <https://cds.cern.ch/record/1095927>.
- [71] D. E. Groom and S. R. Klein, *Passage of particles through matter*, Eur. Phys. J. **15** (2000) 163–173.
- [72] ATLAS Collaboration, *ATLAS liquid-argon calorimeter: Technical Design Report*. Technical Design Report ATLAS. CERN, 1996.  
<http://cds.cern.ch/record/331061>.

- [73] ATLAS Collaboration, *Energy linearity and resolution of the ATLAS electromagnetic barrel calorimeter in an electron test-beam*, Nucl. Instr. Meth. Phys. A **568** (2006) 601 – 623.
- [74] ATLAS Collaboration, *The ATLAS liquid argon hadronic end-cap calorimeter: construction and selected beam test results*, Nucl. Phys. B Proceedings Supplements **150** (2006) 102–105.
- [75] P. Berkvens, *Radiation and Safety Lecture*, 2013.
- [76] A. Para, M. Derric, D. Anderson, E. Fisk, and C. Sazama, *Calorimetry In High Energy Physics - Proceedings Of The International Conference*. World Scientific Publishing Company, 1991.
- [77] I. J.-L. Plante and M. Tylmad, *Pulse shapes for signal reconstruction in the ATLAS Tile Calorimeter*, Nucl. Instr. Meth. Phys. A **617** (2010) 96 – 98, 11th Pisa Meeting on Advanced Detectors.
- [78] ATLAS Collaboration, *Signal Reconstruction of the ATLAS Hadronic Tile Calorimeter: implementation and performance*, J. Phys.: Conference Series **293** (2011) 012056.
- [79] ATLAS Collaboration, *ATLAS Tile Calorimeter performance for single particles in beam tests*, J. Phys.: Conference Series **160** (2009) 012057.
- [80] ATLAS Collaboration, *Performance of the ATLAS hadronic end-cap calorimeter in beam tests*, Nucl. Instr. Meth. Phys. A **482** (2002) 94 – 124.
- [81] ATLAS Collaboration, *Energy calibration of the ATLAS Liquid Argon Forward Calorimeter*, J. Instrum. **3** (2008) P02002.
- [82] ATLAS Collaboration, *Performance of the ATLAS trigger system in 2015*, Eur. Phys. J. C **77** (2017) 317.
- [83] ATLAS Collaboration, *Trigger Menu in 2016*, Tech. Rep. ATL-DAQ-PUB-2017-001, CERN, Geneva, 2017. <https://cds.cern.ch/record/2242069>.
- [84] ATLAS Collaboration, *ATLAS Photos*, 2010. <http://atlasexperiment.org/photos/events-collision-proton.html>.
- [85] J. J. Goodson and R. McCarthy, *Search for Supersymmetry in States with Large Missing Transverse Momentum and Three Leptons including a Z-Boson*. PhD thesis, 2012. <https://cds.cern.ch/record/1449722>.

- [86] W. Lampl, S. Laplace, D. Lelas, P. Loch, H. Ma, S. Menke, S. Rajagopalan, D. Rousseau, S. Snyder, and G. Unal, *Calorimeter Clustering Algorithms: Description and Performance*, Tech. Rep. ATL-LARG-PUB-2008-002. ATL-COM-LARG-2008-003, 2008.
- [87] B. Isildak, *Measurement of the differential dijet production cross section in proton-proton collisions at  $\sqrt{s} = 7$  tev*. PhD thesis, Bogazici U., 2011. <http://inspirehep.net/record/1251416/files/arXiv:1308.6064.pdf>.
- [88] S. D. Ellis and D. E. Soper, *Successive combination jet algorithm for hadron collisions*, Phys. Rev. **D48** (1993) 3160–3166.
- [89] Y. L. Dokshitzer, G. D. Leder, S. Moretti, and B. R. Webber, *Better jet clustering algorithms*, JHEP **08** (1997) 001.
- [90] M. Cacciari, G. P. Salam, and G. Soyez, *The Anti- $k(t)$  jet clustering algorithm*, JHEP **04** (2008) 063, arXiv:0802.1189 [hep-ph].
- [91] ATLAS Collaboration, *The ATLAS Simulation Infrastructure*, Eur. Phys. J. **C70** (2010) 823–874.
- [92] GEANT4 Collaboration, *GEANT4: A Simulation toolkit*, Nucl. Instrum. Meth. **A506** (2003) 250–303.
- [93] T. Sjostrand, S. Mrenna, and P. Z. Skands, *A Brief Introduction to PYTHIA 8.1*, Comput. Phys. Commun. **178** (2008) 852–867.
- [94] B. Andersson, S. Mohanty, and F. Soderberg, *Recent developments in the Lund model*, 2002. arXiv:hep-ph/0212122 [hep-ph].
- [95] ATLAS Collaboration, *ATLAS Run 1 Pythia8 tunes*, Tech. Rep. ATL-PHYS-PUB-2014-021, CERN, 2014.
- [96] S. Carrazza, S. Forte, and J. Rojo, *Parton Distributions and Event Generators*, 2013. arXiv:1311.5887 [hep-ph].
- [97] T. Gleisberg, S. Hoeche, F. Krauss, M. Schonherr, S. Schumann, F. Siegert, and J. Winter, *Event generation with SHERPA 1.1*, JHEP **02** (2009) 007.
- [98] S. Catani, F. Krauss, R. Kuhn, and B. R. Webber, *QCD matrix elements + parton showers*, JHEP **11** (2001) 063.
- [99] J.-C. Winter, F. Krauss, and G. Soff, *A Modified cluster hadronization model*, Eur. Phys. J. **C36** (2004) 381–395.
- [100] H.-L. Lai, M. Guzzi, J. Huston, Z. Li, P. M. Nadolsky, J. Pumplin, and C.-P. Yuan, *New parton distributions for collider physics*, Phys. Rev. D **82** (2010) 074024.

- [101] S. Frixione, P. Nason, and C. Oleari, *Matching NLO QCD computations with Parton Shower simulations: the POWHEG method*, JHEP **11** (2007) 070.
- [102] Z. Nagy, *Next-to-leading order calculation of three jet observables in hadron hadron collision*, Phys. Rev. **D68** (2003) 094002.
- [103] M. H. Seymour, *Jet shapes in hadron collisions: Higher orders, resummation and hadronization*, Nucl. Phys. **B513** (1998) 269–300.
- [104] P. M. Nadolsky, H.-L. Lai, Q.-H. Cao, J. Huston, J. Pumplin, D. Stump, W.-K. Tung, and C. P. Yuan, *Implications of CTEQ global analysis for collider observables*, Phys. Rev. **D78** (2008) 013004.
- [105] ATLAS Collaboration, *Search for light dijet resonances with the ATLAS detector using a Trigger-Object Level Analysis in LHC pp collisions at  $\sqrt{s} = 13$  TeV*, ATLAS-CONF-2016-030, 2016, <http://cds.cern.ch/record/2161135>.
- [106] ATLAS Collaboration, *Search for new phenomena in dijet mass and angular distributions from pp collisions at  $\sqrt{s} = 13$  TeV with the ATLAS detector*, Phys. Lett. **B754** (2016) 302–322.
- [107] B. A. Dobrescu and F. Yu, *Coupling-mass mapping of dijet peak searches*, Phys. Rev. **D88** (2013) 035021.
- [108] ATLAS Collaboration, *Trigger Operation Public Results*, 2016. <https://twiki.cern.ch/twiki/bin/view/AtlasPublic/TriggerOperationPublicResults>.
- [109] ATLAS Collaboration, *Jet Trigger Public Results*, 2016. <https://twiki.cern.ch/twiki/bin/view/AtlasPublic/JetTriggerPublicResults>.
- [110] ATLAS collaboration, *Search for low-mass dijet resonances in 2016 data with Trigger-object-Level Analysis*, ATL-COM-PHYS-2016-1498, 2016, ATLAS internal document.
- [111] ATLAS Collaboration, *Performance of pile-up mitigation techniques for jets in pp collisions at  $\sqrt{s} = 8$  TeV using the ATLAS detector*, Eur. Phys. J. **C76** (2016) 581.
- [112] ATLAS Collaboration, *Jet energy scale measurements and their systematic uncertainties in proton-proton collisions at  $\sqrt{s} = 13$  TeV with the ATLAS detector*, CERN-EP-2017-038, 2017, [arXiv:1703.09665](https://arxiv.org/abs/1703.09665) [hep-ex].
- [113] ATLAS Collaboration, *Jet energy measurement with the ATLAS detector in proton-proton collisions at  $\sqrt{s} = 7$  TeV*, Eur. Phys. J. **C73** (2013) 2304.
- [114] N. Bludau, *Calibration of Jets at Trigger-Level for a Low Mass Dijet Search at ATLAS*, master’s thesis, Universität Heidelberg, 2017.

- [115] ATLAS Collaboration, *Jet global sequential corrections with the ATLAS detector in proton-proton collisions at  $\sqrt{s} = 8$  TeV*, ATLAS-CONF-2015-002, 2015, <https://cds.cern.ch/record/2001682>.
- [116] ATLAS Collaboration, *Jet energy measurement and its systematic uncertainty in proton-proton collisions at  $\sqrt{s} = 7$  TeV with the ATLAS detector*, Eur. Phys. J. **C75** (2015) 17.
- [117] ATLAS Collaboration, *JES Public Plots for Moriond 2017*, 2017. <https://atlas.web.cern.ch/Atlas/GROUPS/PHYSICS/PLOTS/JETM-2017-003/>.
- [118] ATLAS Collaboration, *Determination of the jet energy scale and resolution at ATLAS using  $Z/\gamma$ -jet events in data at  $\sqrt{s} = 8$  TeV*, ATLAS-CONF-2015-057, 2015.
- [119] ATLAS Collaboration, *Photon and electron identification with the ATLAS detector*, ATL-PHYS-PROC-2016-230, 2016, <https://cds.cern.ch/record/2233097>.
- [120] J. Mitrevski, *Electron and Photon Reconstruction with the ATLAS Detector*, 37th International Conference on High Energy Physics (ICHEP): Nuclear and Particle Physics Proceedings **273-275** (2016) 2539 – 2541.
- [121] ATLAS Collaboration, *Muon reconstruction performance in early  $\sqrt{s} = 13$  TeV data*, ATL-PHYS-PUB-2015-037, 2015, <https://cds.cern.ch/record/2047831>.
- [122] Particle Data Group Collaboration, C. Patrignani et al., *Review of Particle Physics*, Chin. Phys. **C40** no. 10, (2016) 100001.
- [123] ATLAS Collaboration, *A method for the construction of strongly reduced representations of ATLAS experimental uncertainties and the application thereof to the jet energy scale*, ATL-PHYS-PUB-2015-014, 2015, <https://cds.cern.ch/record/2037436>.
- [124] Meyer zu Theenhausen, H., *Animated illustration of the sliding window fit "SWiFt" and how it is employed within the ATLAS Dijet TLA*, 2017. [https://wiki.kip.uni-heidelberg.de/KIPwiki/images/b/be/Swiftanimation\\_HMeyerZuTheenhausen.gif](https://wiki.kip.uni-heidelberg.de/KIPwiki/images/b/be/Swiftanimation_HMeyerZuTheenhausen.gif).
- [125] ATLAS Collaboration, ATLAS Collaboration, *Search for new phenomena in the dijet mass distribution using  $p - p$  collision data at  $\sqrt{s} = 8$  TeV with the ATLAS detector*, Phys. Rev. **D91** (2015) 052007.
- [126] UA2 Collaboration, *A measurement of two-jet decays of the  $W$  and  $Z$  bosons at the CERN  $\bar{p}p$  collider*, Zeitschrift für Physik C Particles and Fields **49** (1991) 17–28.

- [127] ATLAS Collaboration, ATLAS Collaboration, *Search for strong gravity in multijet final states produced in pp collisions at  $\sqrt{s} = 13$  TeV using the ATLAS detector at the LHC*, JHEP **03** (2016) 026.
- [128] ATLAS Collaboration, *Search for resonances decaying to photon pairs in  $3.2 \text{ fb}^{-1}$  of pp collisions at  $\sqrt{s} = 13$  TeV with the ATLAS detector*, ATLAS-CONF-2015-081, 2015.
- [129] CDF Collaboration, *Global search for new physics with  $2.0 \text{ fb}^{-1}$  at CDF*, Phys. Rev. D **79** (2009) 011101.
- [130] G. Choudalakis, *On hypothesis testing, trials factor, hypertests and the BumpHunter*, ArXiv e-prints (2011), arXiv:1101.0390 [physics.data-an].
- [131] G. Choudalakis and D. Casadei, *Plotting the differences between data and expectation*, Eur. Phys. J. Plus **127** (2012) 25.
- [132] L. Lyons, *Open statistical issues in Particle Physics*, Ann. Appl. Stat. **2** (2008) 887–915.
- [133] A. Roodman, *Blind analysis in particle physics*, Statistical problems in particle physics, astrophysics and cosmology. Proceedings, Conference, PHYSTAT (2003), arXiv:physics/0312102.
- [134] ATLAS Collaboration, *Exotics Public Results*, 2017.  
<https://twiki.cern.ch/twiki/bin/view/AtlasPublic/ExoticsPublicResults>.
- [135] ATLAS Collaboration, *FTK: a Fast Track Trigger for ATLAS*, J. Instrum. **7** (2012) C10002, <http://stacks.iop.org/1748-0221/7/i=10/a=C10002>.
- [136] ATLAS Collaboration, *Selection of jets produced in 13TeV proton-proton collisions with the ATLAS detector*, ATLAS-CONF-2015-029, 2015.

# Acknowledgements

This thesis would not have been possible without the help and support of many people. First, I'd like to thank Prof. Hans-Christian Schultz-Coulon for giving me the opportunity to work on a research topic about a fundamental question of nature and I am happy that he encouraged me to work on this for a year at a place like CERN. I appreciate his council and that I never missed anything in his KIP working group, be it travel opportunities, expert assistance or social events. I know it takes a lot of work to keep everything running and I do not take it for granted.

I also want to thank Prof. Klaus Reygers, who kindly agreed to co-review this thesis. I could not have received a better supervision in my local ATLAS group and I am very grateful for that. Here my special thanks goes to Monica Dunford and Pavel Starovoitov. Monica always gave me excellent advice, especially for the big picture of my work and development of my skills in general. Without her motivational words all of this would have been much harder. Pavel shared his inexhaustible knowledge about jets with me and his relaxed mood gave me some easiness in stressful times.

I also could not have ended up in a better analysis group than the TLA group and I want to thank every member for contributing to such a friendly and motivating working atmosphere. Here I'd like to express particular thanks to Caterina Doglioni. Despite not being in my local group, Caterina was always there to discuss results and next steps, even from airports or boats at any time of the day/night. Her enthusiasm about the TLA and getting her own hands dirty was quite intoxicating. She definitely changed my view of how working in a team can be.

From my time in L1Calo I'd like to cordially thank Martin Wessels and Ivana Hristova. Both helped me a lot during my starting time in ATLAS and never made me feel stupid when I was asking my beginner's questions.

Of course I want to thank my diligent proof-readers Julia, Monica, Claire, Nadia, Pavel, Sebastian, Stanislav, Martin, Rainer, Thomas and Jan.

I am very happy to have my colleagues, or better to say friends, Manü, Merve, Julia, Alessandra, Claire, Nadia, Sebastian, Thomas, Stanislav, Jan and Adam. Thank you all for a great time inside and outside the university or CERN. And of course I thank Vany. Writing our both theses, side-by-side made everything half the struggle. Thank you for the good chemistry.

Last I want to express a huge thank you to my family, to Sigrid, Joachim and Moritz, for their strength in not so easy times.